박 사 학 위 논 문

Understanding of sea-level rise and decadal changes on regional and global scales since 1993

차 현 수

제주대학교 대학원

지구해양융합학부 지구해양전공

2024년 02월

Understanding of sea-level rise and decadal changes on regional and global scales since 1993

이 논문을 이학박사 학위논문으로 제출함

차현수

제주대학교 대학원

지구해양융합학부 지구해양전공

지도교수 문 재 홍

차현수의 이학박사 학위논문을 인준함

2024년 02월

심사위원장 송 상 근 (NU)

위 원 문 재 홍 (FU)

위 원 남 성 현 (FU)

위 원 조 영 헌 (FU)

위 원 김 병 훈 (FU)

Understanding of sea-level rise and decadal changes on regional and global scales since 1993

Hyeonsoo Cha

(Supervised by Professor Jae-Hong Moon)

A thesis submitted in partial fulfillment of the requirements
for the degree of Doctor of Science

2024. 02.

This thesis has been examined and approved.

Thesis director, Sang-Keun Song, Prof. of Earth and Marine Sciences in JNU
Jae-Hong Moon, Prof. of Earth and Marine Sciences in JNU
Sung-Hyun Nam, Prof. of School of Earth and Environmental Sciences in SNU
Young-Heon Jo, Prof. of Department of Oceanography in PNU
Byeong-Hoon Kim, Ph. D. of Korea Polar Research Institute

Faculty of Earth and Marine Convergence
Earth and Marine Science Major

GRADUATE SCHOOL
JEJU NATIONAL UNIVERSITY

Contents

List of Figures

List of Tables

Abstract

Present-day sea-level rise is the key indicator of climate change. Since late 1992, the satellite altimeters have clearly shown the global mean sea-level (GMSL) has been rising due to anthropogenic changes in Earth's climate system, including increased ice-melting and ocean heat uptake. However, despite continuous global warming, the GMSL rise slowed over the 2000s, and the sea level decreased in the eastern tropical Pacific and increased in the western tropical Pacific. After the 2010, the GMSL increased again, and the pattern reversed compared with the earlier decades. Natural climate variability, which is responsible for redistributing ocean heat and land water storage, can obscure the underlying global and regional sea-level rise. Therefore, identifying the climate-driven sea-level change on global and regional scales is essential to enhance our understanding of sea-level changes and mitigate the impact of ongoing sea-level rise.

Sea-level changes are caused by several physical processes. Recent advancements in in-situ observation and satellite measurements have enabled comparing the sum of each process with the observed sea-level change within uncertainty. Previous studies have demonstrated the closure of the GMSL budget and the contribution of each process to sea-level rise (Chen et al., 2017; Dieng et al., 2017; WCRP, 2018; Royston et al., 2020; Cha et al., 2021). However, due to each physical process varying in space and time, estimating their contribution to sea-level rise on a regional scale remains a challenging issue. East Asian marginal seas, including the Yellow and East China Seas, South China Sea, and East/Japan Sea, have experienced higher sea-level rise than the GMSL. Thus, sea-level rise is getting more attention because a lot of people live near the East Asian Marginal Seas.

In this dissertation, three studies are carried out to improve our understanding of climate-driven sea-level variability and underlying process of sea-level rise on global and regional

scales. The first study examines the decade-long fluctuation in the GMSL rise, which can be attributed to climate-related decadal fluctuation in ocean heat storage and hydrology. The GMSL rise rate was slowed down over the 2000s and has increased rapidly after 2011. Over the 2010s, the climate-driven decadal changes led to additional ocean mass gain from land water storage and increased ocean heat uptake, resulting in the GMSL rise rate increasing. This study demonstrates that this decadal fluctuation is linked to Pacific decadal variability and notes that the importance of natural variability in understanding the impact of the ongoing sea-level rise.

The second study focuses on a dramatic shift in the tropical Pacific Ocean toward an El Niño-like state, which coincides with a period of a recent resumption of global warming after a hiatus in the 2000s. The observation and model data analysis using ensemble empirical mode decomposition shows that the distinct decadal mode in the tropical Pacific is associated with the suppression and resumption of global warming over this period. This decadal mode is associated with Pacific Decadal Oscillation-related wind variability on a decadal time scale, which can control the sea-level trend, subsurface temperature changes, and the strength of the Equatorial Under Current in the tropical Pacific. Hindcast and model experiments illustrate that decadal climate-related wind forcing can control regional oceanic response in the tropical Pacific has a possible link to global ocean warming.

The third study is a process-based assessment of the sea-level rise in the northwestern Pacific marginal seas, including the Yellow and East China Sea, South China Sea, and East/Japan Sea. This study conducts the budget analysis comparing the combination of observation and reanalysis with satellite sea-level change and estimates the contribution of each physical process to sea-level rise. The result shows that the sterodynamic effect and ice-melting are significant processes to sea-level rise and sterodynamic process dominates the

spatial pattern and variability. Further estimation using in situ profiles and satellite gravity measurement presents that ocean mass redistribution plays a crucial role in sterodynamic sea-level change along the continental shelves.

Chapter 1. Introduction

After satellite altimetry was launched, it has been making the near global coverage for observing sea-level change with high accuracy since late September 1992, allowing us to observe sea-level changes in oceans and seas around the world. Advancements in satellite and ocean in-situ measurements greatly improved our understanding of sea-level changes. This continuous ocean monitoring has revealed that global and regional sea levels have been rising due to anthropogenic changes in ocean heat uptake and ice-melting. However, despite ongoing global warming, sea-level rise on global and regional scales is not uniform and varies in time and space. Sea-level changes can be complicated by the combination of internal variability and continuous sea-level rise. Thus, identifying the cause of ongoing sea-level trends and variability from global and regional sea-level change is crucial to our understanding the sea-level rise and supporting local adaptation planning.

Natural climate variability on interannual to decadal timescales can obscure the underlying global and regional sea-level rise, changing the trend over short timescales. El Nino-Southern Oscillation (ENSO) is one of the most significant climate variabilities on the Earth, which can alter atmospheric circulation, affecting temperature and precipitation patterns. Many previous studies have shown that GMSL is significantly correlated with ENSO, with GMSL rising during the El Niño phase and declining during La Niña (Boening et al. 2012; Fasullo et al. 2013; Cazenave et al., 2014; Nerem et al., 2018; Hamlington et al., 2020). It has been reported that the sea-level change related to ENSO is closely linked to the dominant changes in ocean heat storage and global hydrological cycle. However, the relative contribution of heat storage and hydrological cycle to GMSL has remained unclear.

There is also ENSO-like climate variability on the decadal time scale in the Pacific, called Pacific Decadal Oscillation (PDO), which has a similar pattern to ENSO but more widespread

variations across the Pacific basin (Mantua et al., 1997). It is closely connected with global sea-level changes (Hamlington et al., 2019; Moreira et al., 2021). While GMSL has been rising about 3.1±0.3 mm/yr over the altimetry period from 1993 to 2017, there was a noticeable slowdown in the rate of GMSL rise of ~2.4mm/yr over the 2000s. This slowdown is consistent with a pause in the rise of the global mean surface temperature (GMST), known as the global warming hiatus (England et al., 2014; Maher et al., 2018). Climate-driven land water storage change contributed to this GMSL slowdown (Cazenave et al., 2014; Reager et al., 2016). Despite the global ocean has absorbed over 90% of the extra energy in the climate system due to anthropogenic warming, observational studies have shown that ocean heat uptake also slowed over the 2000s (Xie et al., 2016; Von Schuckmann et al., 2020; Loeb et al., 2021). Following the hiatus, the rate of GMSL rise increased again and the Pacific climate variability can play a role in GMSL acceleration occurring on decadal time scale (Hamlington et al., 2019). These findings indicate that ocean mass and heat uptake can modulate GMSL rise both during and after the hiatus. However, their contribution to sea-level budget and interplay with natural climate variability are lacking.

During the hiatus period, La Niña-like patterns appeared in the Pacific, closely linked to the negative phase of PDO and Interdecadal Pacific Oscillation (IPO; Power et al. 1999). These patterns are associated with strengthening trade winds and increasing (decreasing) the sea-level on the western (eastern) tropical Pacific (England et al., 2014). In contrast to the hiatus period, the global mean temperature increased again over the 2010s, accompanied by a notable shift in the tropical Pacific, where the sea surface temperature of the eastern (western) tropical Pacific has consistently risen (decreased). At the same time, the Pacific sea-level has also experienced sharply increasing (decreasing) in the eastern (western) tropical Pacific. Hu and Fedorov (2017) suggested that strong La Niña in 2011/2012 followed by a strong El Niño in 2015/2016 were a main factor contributing to the dramatic shift in the tropical Pacific.

Nonetheless, this ongoing shift is attributed to not only interannual ENSO but also low frequency variability in the Pacific basin (Hamlington et al., 2016).

Due to regional sea-level rise affected by various physical processes varying in space and time, sea-level changes are usually not spatially uniform. Understanding and quantifying the contribution of each process to regional sea-level changes is essential to prevent low-lying inundation in preparation for future ocean conditions. East Asian marginal seas (EAMS), including the Yellow and East China Sea (YECS), South China Sea (SCS), and East/Japan Sea (EJS), are vulnerable regions to the impact of sea-level rise due to high coastal populations. Previous studies have shown that these marginal seas have undergone higher rates of sea-level rise than GMSL over the past decades (Feng et al., 2012; Moon and Song, 2013; Guo et al., 2015; Cheng et al., 2016; Yu et al., 2019). These studies predominantly have focused on sea-level fluctuations in response to climate variability, such as ENSO, North Pacific Gyre Oscillation (NPGO), and PDO, on interannual to decadal timescales. However, relatively less attention has been paid to assessing the underlying processes contributing to sea-level rise on marginal seas, including extensive continental shelves.

Considering these complexities, assessing the underlying processes contributing to sea-level rise and estimating climate-driven sea-level variation is crucial to enhancing our understanding sea-level change and the ocean's role in the global climate system. Therefore, this dissertation examined the climate-driven decadal sea-level variability both in the tropical Pacific and globally and assessed the contributions of underlying processes to sea-level rise in marginal seas in the northwestern Pacific. Data and methods are briefly described in Chapter 2. Chapter 3.1 demonstrates decade-long fluctuation in GMSL rise and identifies the effect of climate-driven Earth energy change and hydrological cycle on GMSL rise. In Chapter 3.2, this study investigates the recent shift toward an El Nino-like state in the Pacific and its connection

with Pacific decadal climate-related wind patterns. The ocean circulation model is used to identify the dynamical response of ocean circulation to climate-driven wind changes. Chapter 3.3 assesses the regional sea-level rise budget on marginal seas in northwestern Pacific (YECS, SCS, and EJS) and examine whether the sum of individual processes can account for the observed sea-level rise on these marginal seas. The concluding remarks are presented in Chapter 4. A discussion of this dissertation is given in Chapter 5.

Chapter 2. Data and Methods

2.1. Processes of global mean sea-level rise

The global mean sea-level (GMSL) has been rising due to thermal expansion and mass input to the ocean. Steric sea-level change refers to the contributions of thermal expansion associated with ocean heat change, but the ocean mass change is affected by various processes in the earth's climate system (Antarctica and Greenland Ice Sheets, Glaciers, and Land Water Storage (LWS)). Thus, GMSL can be written using the following budget equation:

$$GMSL = GMSL_{Steric} + GMSL_{Antarctica} + GMSL_{Greenland} + GMSL_{Glaciers} + GMSL_{LWS}$$

To examine global mean sea-level change and sea-level budget over an altimetry period, we considered six altimetry GMSL products and estimated the contributions of each component, as follows.

Satellite altimetry. We use six different altimetry products processed by five groups: Archiving, Validation and Interpretation of Satellite Oceanographic data (AVISO; https://www.aviso.altimetry.fr/data/products/ocean-indicators-products/mean-sea-level.html); Commonwealth Scientific and Industrial Research Organization (CSIRO; https://research.csiro.au/slrwavescoast/sea-level/measurements-and-data/sea-level-data/); Colorado University (CU 2018 Release 1; http://sealevel.colorado.edu/content/2018rel1-global-mean-sea-level-time-series-seasonal-signals-removed); National Oceanographic and Atmospheric Administration (NOAA; https://www.star.nesdis.noaa.gov/socd/lsa/SeaLevelRise/LSA_SLR_timeseries.php); NASA, Goddard Space Flight Centre (NASA-GSFC version 4; https://podaac.jpl.nasa.gov/dataset/MERGED_TP_J1_OSTM_OST_GMSL_ASCII_V4); The Climate Change Initiative (CCI version 2; http://www.esa-sealevel-cci.org/products). The effect of Glacier Isostatic Adjustment (GIA) is accounted for in each GMSL time-series, except

for the NOAA data. The NOAA sea level data was corrected for the GIA effect by using -0.3 mm/yr based on Peltier (2004). In addition, a correction of TOPEX-A instrumental drift for the altimeter data sets was considered (1.5 mm/yr) over the period of 1993–1999, except for the NASA-GSFC data, which was already corrected for the drift correction (Beckley et al., 2017; Dieng et al., 2017; Watson et al., 2015). Similar to previous studies (Dieng et al., 2017; Yi et al., 2015), we use the ensemble average from all products instead of relying on a single altimetry-derived GMSL time series. Uncertainties are based on the dispersion among different time series around the mean. Figure 2.1a shows the time-series of GMSL in each product and their ensemble average from 1993 to 2018. Detailed information of each data set is available in the corresponding website.

Steric Sea Levels. To quantify the steric component of GMSL, we use the following different data sets: Ishii and Kimoto (2009) (hereafter IK) data set (https://rda.ucar.edu/datasets/ds285.3); EN4 data set (Good et al., 2013) (https://www.metoffice.gov.uk/hadobs/en4/download-en4-2-0.html); NOAA data set (Levitus et al., 2012) (https://www.nodc.noaa.gov/OC5/3M_HEAT_CONTENT/tsl_global.html). These products integrate the temperature and salinity data from the surface to 700 m depth at monthly intervals. Two of the time series cover the period of 1993–2017, but the IK data ends in 2012. Total steric sea-level is reconstructed from the ensemble average of the upper ocean time series, the estimate (0.24 mm/yr) from 700 to 2000 m based on Chambers et al. (2017) and the deep ocean trend (0.11 mm/yr) based on Purkey and Johnson (2010). After 2005, we utilize three different Argo data sets, providing temperature and salinity down to 2000 m depth at monthly intervals: The International Pacific Research Center (IPRC, http://apdrc.soest.hawaii.edu/projects/Argo/data/gridded/On_standard_levels/index-1.html); The Japan Agency for Marine-Earth Science and Technology (JAMSTEC, https://pubargo.jamstec.go.jp/public/MOAA_GPV/Glb_PRS/OI/); The SCRIPPS Institution

of Oceanography (SCRIPPS; http://sio-argo.ucsd.edu/RG_Climatology.html). For the three data sets, we computed steric sea level time series from the surface down to 2000 m on a 1°x1° grid for the period of January 2005 to December 2017. The estimate for the deep ocean contribution (0.11 mm/yr) based on Purkey and Johnson (2010) was also added over the whole data length. During the Argo period, we use the ensemble average of all steric sea level products. The standard deviation of the residuals of the individual time series with the ensemble mean represents the systematic uncertainty. The monthly time series of steric sea level in each product and their ensemble mean are shown in Figure 2.1b.

Antarctica and Greenland Ice Sheets. Greenland and Antarctica Ice Sheet data from the Ice sheet Mass Balance Inter-comparison Exercise (IMBIE; http://imbie.org/data-downloads/) are used in this study. The IMBIE data provides a reconciled estimate of ice sheet mass balance by using satellite altimetry, space gravimetry and the input-output method (Shepherd et al., 2012). The IMBIE supports the Antarctica ice sheet (AIS) data from January 1992 to June 2017 and newly released Greenland ice sheet (GIS) data from January 1992 to December 2018 (IMBIE Team, 2020). Uncertainty of cumulative ice sheet mass change is estimated as the root sum square of annual errors (IMBIE Team, 2020). Figure 2.1c provides the contributions of Greenland and Antarctica ice sheets to GMSL rise and their uncertainties.

Glaciers. For the global glacier mass balance, we considered four time series that have different time periods: (1) Zemp et al. (2019) for the period 1961–2016; (2) Marzeion et al. (2015) for the period 1902–2013; (3) Leclercq et al. (2011) for the period 1800–2010, (4) Cogley (2009) for the period 1950–2015. Because these datasets are given at annual or pentadal intervals, time series are interpolated onto regular monthly intervals over 1993–2016; consequently, we use the ensemble average across the interpolated records. We computed the uncertainty associated with each time series (σ_i) and the spread around the ensemble mean

(σ_{spread}) through the quadratic sum:

$$\sum \sqrt{\sigma_i^2 + {\sigma_{spread}}^2}$$

The monthly time series of the glacier in each data set and their ensemble mean are shown in Figure 2.1d.

Land Water Storage (LWS). For LWS contributions, the GRACE mascon solution (JPL RL06Mv2) from April 2002 to Jun 2016 is used in this study. Several post-processing corrections, such as geocenter motion, GIA signal, and solid earth response to tectonic events, are applied to this RL06Mv2 solution (Peltier et al., 2018; Reager et al., 2016; Wiese et al., 2016). To isolate LWS in GRACE mascon, we removed the glacier signals from the data over land based on Wouters et al. (2019). The standard error is based on noise assessment by Groh et al. (2019). Prior to the GRACE period, information on the LWS component is sourced from the reanalysis products over the 1993–2002 period, namely: Modern Era Retrospective-analysis for Research and Applications (MERRA)-Land (Reichle et al., 2011) and an updated MERRA version 2 with hydrology data (Reichle et al., 2017); this data is freely available at GES DISC (https://disc.gsfc.nasa.gov/). MERRA-Land is a land-only reanalysis data that supplements the original MERRA product (Reichle et al., 2011). MERRA-2 uses observation-based precipitation data to derive the land surface water budget, allowing the near-surface air temperature and humidity to respond to the improved precipitation forcing (Reichle et al., 2017). Figure 2.1e shows the time-series of LWS in each product and the corresponding ensemble average.

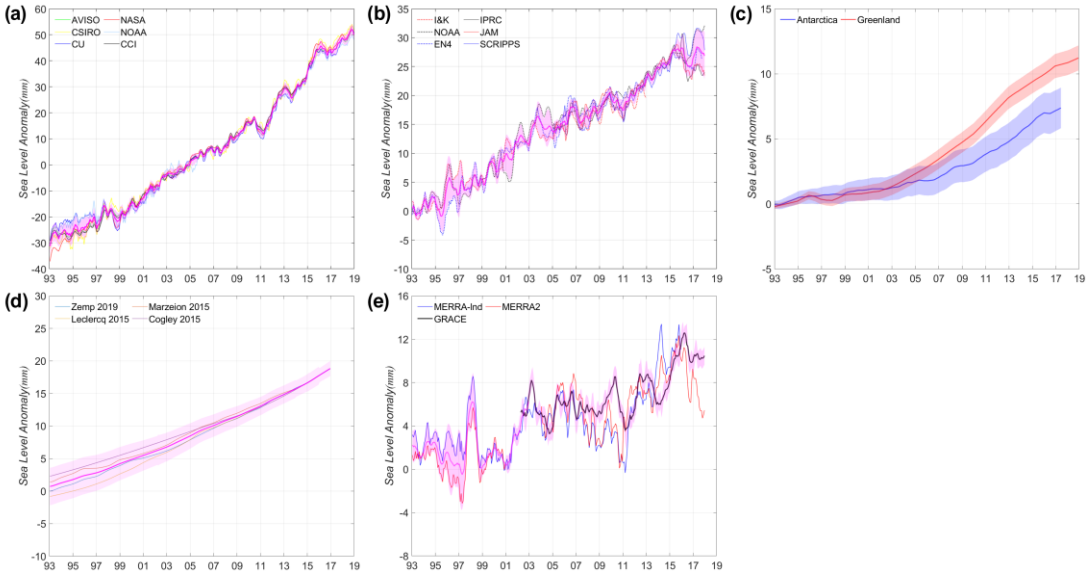

Figure 2.1. Each component of GMSL budget for (a) satellite altimetry, (b) steric, (c) Antarctica and Greenland Ice Sheets, (d) Glacier, and (e) land water storage. The uncertainties of each component are shown in coloured shades.

2.2. Processes of regional sea-level change

Unlike the global mean sea-level change, each physical process varies both space and time. The altimeter-derived regional geocentric sea-level (SL_{ALT}) can be expressed by three main processes: (1) changes in local ocean density and ocean dynamics, which is called sterodynamic sea-level (SL_{SD}, Gregory et al., 2019), (2) changes in Earth's Gravity, Rotation, and Deformation (GRD) caused by contemporary mass redistribution from land ice and land water storage changes (SL_{GRD}), and (3) ongoing surface movement of glacial isostatic adjustment (SL_{GIA}, Peltier, 2004; Tamisiea and Mitrovica, 2011; Caron et al., 2018). The relation between these processes can be written using the following budget equation: $SL_{ALT} = SL_{SD} + SL_{GRD} + SL_{GIA} + SL_{RES}$. SL_{RES} is a residual given by the difference between the geocentric sea-level and the sum of all components, which includes uncertainties of data used. For the assessment of sea-level budget in the northwestern Pacific marginal seas, here we compare the regional SLR (SL_{ALT}) trends to the sum of estimates of individual contributor, i.e., SL_{SD}, SL_{GRD}, and SL_{GIA}. The sea-level change from altimetry and each process are estimated as follows.

Sea level observation from satellite altimetry. To identify the spatial and temporal changes of sea-level rise (SLR) in the Northwestern Pacific marginal seas, we use the geocentric sea-level data derived from AVISO monthly 0.25 degree gridded sea surface height anomaly data from 1993 to 2017 (https://data.marine.copernicus.eu/product/SEALEVEL_GLO_PHY_L4_MY_008_047/description).

Sterodynamic effect. Following the method described previously (e.g., Gregory et al., 2019; Harvey et al., 2021; Wang et al., 2021), the regional sterodynamic sea-level (SL_{SD}) is estimated by combining global mean thermosteric sea-level (GMTS) with dynamic sea-level

(DSL) from ocean reanalysis: $SL_{SD} = GMTS + DSL$.

We use GMTS estimates from three sources of in situ-based ocean subsurface temperature: Institute of Atmospheric Physics (IAP, Cheng et al., 2017), Met Office Hadley Centre observations datasets EN.4.2.2 (EN4, Good et al., 2013), and Japan Meteorological Agency (JMA, Ishii and Kimoto, 2009; Ishii et al., 2017). An ensemble mean of these products is taken to estimate the observation-based GMTS and uncertainty is derived from spread of the ensemble mean (i.e., standard deviation). For the estimate of regional SLR associated with ocean dynamics, we use two monthly products of ocean reanalysis over the 1993-2017 period, including the German contribution of the Estimating the Circulation and Climate of the Ocean project (GECCO3, Köhl, 2020) at 1° spatial resolution and Estimating the Circulation and Climate of the Ocean version4 release 4 (ECCO v4r4, Forget et al., 2015; Fukumori et al., 2017; ECCO Consortium, 2021) at 1/2° resolution. Because the ocean models used in these products do not conserve the ocean mass or heat, a time-varying global mean of each product is removed from their sea-surface height to calculate the regional DSL, thereby setting the global mean of DSL to zero (Carton et al., 2019; Hamlington et al., 2019; Harvey et al., 2021; Wang et al., 2021). The mean of these DSL products is finally added to the observation-based GMTS to estimate the sterodynamic effect. Figure 2.2 shows the spatial patterns of SL_{SD} trends calculated using GECCO and ECCO products, respectively.

Contemporary mass redistribution. Contemporary mass redistribution, resulting from changes in melting ice (ICE, ice sheets and glaciers) and land water storage (LWS), cause gravitational, rotational, and deformation (GRD) effects, which is called contemporary-GRD fingerprints: $SL_{GRD} = ICE + LWS$. ICE is the GRD effect resulting from the ice sheets of Greenland and Antarctica, and land glaciers. LWS is the water exchange between ocean and land, which contains groundwater depletion, dam retention, and natural variability. To assess

the GRD effects from global mass redistribution, we use the yearly estimates at 1/2° spatial resolution from Frederikse et al. (2020), which provides reconstructed datasets, including effects of land glaciers, Greenland ice sheets, Antarctica ice sheets, and land water storage from anthropogenic and natural changes. These estimates are based on in-situ observation and models during the period of 1993–2003, while they are based on GRACE measurements after 2003 (for more details of dataset and its uncertainties, see Frederikse et al., 2020). To directly compare with the geocentric sea-level, relative sea-level components associated with the contemporary mass redistribution were transformed into the geocentric sea-levels by subtracting vertical land motion of each component (Frederikse et al., 2019). The yearly estimates from Frederikse et al. (2020) were also converted to monthly interval estimates by using 3rd order interpolation method. Because high-frequencies shorter than annual are not involved in the interpolated datasets, we have also eliminated semi-annual and annual signals from all individual monthly datasets for a direct comparison.

Glacial isostatic adjustment. Glacial isostatic adjustment (GIA) is the change due to ongoing movement in the solid earth caused by past glacier changes. To identify the GIA contribution to the regional SLR trends in the marginal seas, the geocentric GRD change associated with the GIA is examined using the estimate of Caron et al. (2018), which includes an estimate of the associated uncertainties. This estimate used the ensemble of 128,000 GIA model predictions informed by the Global Positioning System (GPS) and relative sea-level dataset. See Caron et al. (2018) for more details of the estimate.

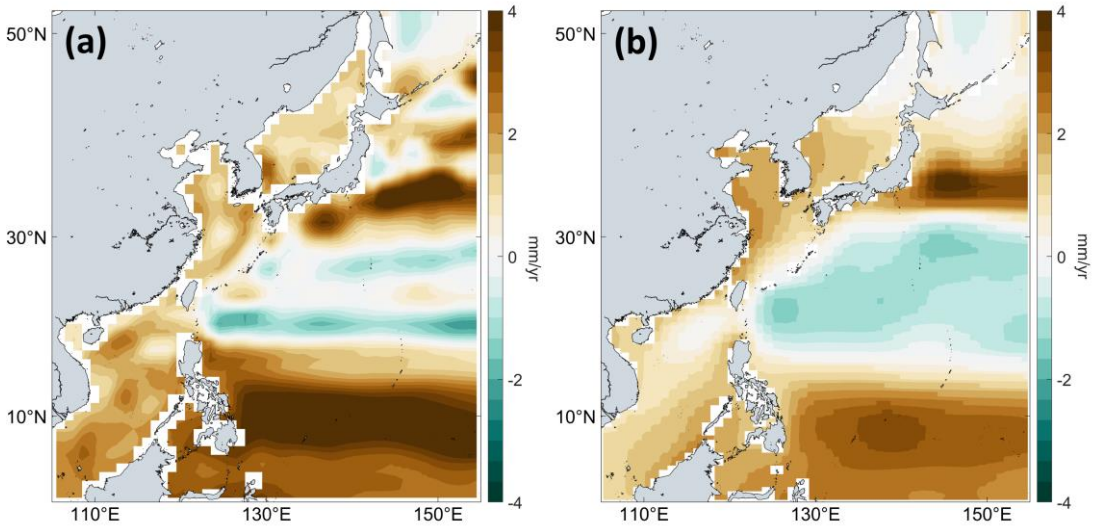

Figure 2.2. Sea-level rise trend from sterodynamic process. Trends of sterodynamic sea-level in the northwestern Pacific based on two products of ocean reanalysis over 1993-2017: (a) GECCO and (b) ECCO. The sterodynamic contribution is estimated by the sum of observation-based GMTS and regional dynamic sea-level from each ocean reanalysis product.

2.3. Ensemble Empirical Mode Decomposition (EEMD) Method.

To extract the climate-driven decadal variability in all data sets, we use an ensemble empirical mode decomposition (EEMD) method, which has been widely used in many geophysical climatology applications. The EEMD method is based on empirical mode decomposition (EMD), which is designed to separate the time series into a finite number of intrinsic mode functions (IMFs) and a residual trend that represents the long-term adaptive trend (Huang et al., 1998, Wu and Huang, 2009). The IMFs of EEMD have been obtained as an ensemble average of IMFs that were decomposed from the original time-series, with the addition of Gaussian white noise by EMD. This advanced method resolves the mode mixing problem caused by intermittence signal in the original EMD. Here, we set the white noise with variance σ=0.2 relative to the variance of the original time-series and the number of ensemble members N=500. Figure 2.3-4 shows the EEMD results for GMSL and the tropical Pacific sea-level, which yielded seven IMFs and residuals in ascending order from highest-frequency to lowest-frequency. Based on spectral analysis, the EEMD-derived IMFs can be grouped into four major time-scale components: IMFs 1–2 as the high-frequency components of less than a year, IMFs 3–5 as the ENSO-scales frequencies ranging from 1.5 to 7 years, and IMF 6–7 as the decadal-scales component with a peak period of ~ 12 years; a residual was taken as the intrinsic trend. Note that the EEMD-determined ENSO signals are clearly separated from the decadal mode and the secular trend.

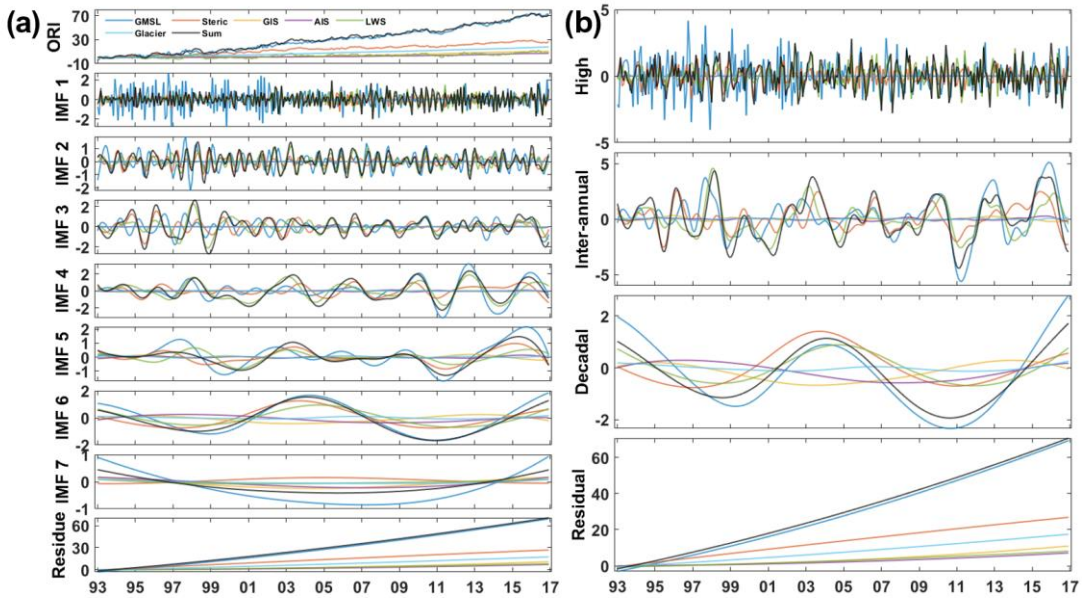

Figure 2.3. EEMD results for all components of global mean sea-level budget. (a) All of the original monthly data (top) are decomposed into seven intrinsic mode functions (IMFs) and the resulting trends (bottom) in ascending order. (b) Four major time-scale components representing high-frequency (IMFs 1–2), ENSO-scale frequency (IMFs 3–5), decadal-scale frequency (IMFs 6–7), and residual.

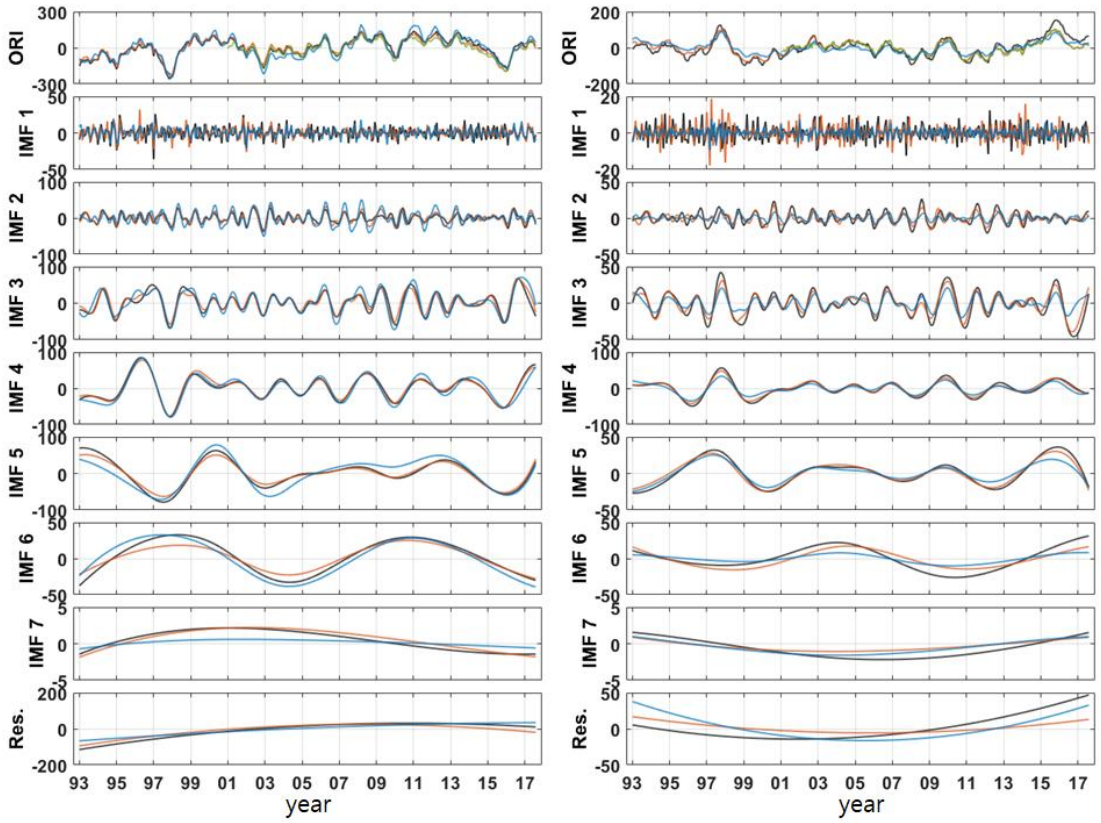

Figure 2.4. EEMD decompositions of time series in the western tropical Pacific (left) and central-to-eastern tropical Pacific (right panels) for the altimetry-based sea levels (black), EN4 steric sea-level (orange), and model steric sea-level (blue). All of the original monthly data (top) are decomposed into seven IMFs and the resulting trends (bottom panels) by EEMD method. Same as Figure 2.3 the EEMD-derived IMFs can be grouped into four major time-scale components: high-frequency (IMFs 1–2), ENSO-scale frequency (IMFs 3–5), decadal-scale frequency (IMFs 6–7), and residual.

Chapter 3. Results

3.1. Underlying drivers of decade-long fluctuation in the global mean sea-level rise

3.1.1. Introduction

Globally, the mean sea level has increased ~ 20 cm over the past century, and has been rising by nearly 3 mm/yr during the period of 1993−2017 (IPCC, 2013; Ablain et al., 2017; WCRP Global Sea Level Budget Group, 2018 (hereafter WCRP)). The change in the global mean sea level (GMSL) rate has been primarily attributed to the effect of thermal expansion in ocean, mass loss from glaciers and ice sheets, and changing land water storage (LWS) (Gardner et al., 2013; Shepherd et al., 2012; Wada et al., 2012; Marzeion et al., 2014). The GMSL budget was estimated by WCRP (2018), comparing the sum of all sea-level components with the observed GMSL. The altimetry-based sea-level products showed an average rate of 3.1 mm/yr in the GMSL trend over the altimeter era. The rate of sea-level rise has increased over the recent decades and has been faster since 2010s. The increases in the rate of sea-level rise are also not globally uniform (e.g., IPCC, 2013). These results indicate that the rate of GMSL rise is perturbed by internal climate modes in the complex Earth's climate system. Although the secular trend of GMSL rise is a crucial indicator of ongoing global warming, the fluctuations on interannual to decadal timescales superimposed on this trend can also provide important clues for the role of oceans in Earth's energy imbalance (EEI) and global hydrological cycle.

Natural climate variability on interannual to decadal timescales masks the background trend of the detected sea level, thereby changing the acceleration values over short timescales. Previous studies have shown that the GMSL responds to the interannual El Niño-Southern

Oscillation (ENSO) variability (Boening et al., 2012; Fasullo et al., 2013; Cazenave et al., 2014; Nerem et al., 2018; Hamlington et al., 2020). It has been reported that the sea level variations related to the ENSO are closely linked to the dominant changes in ocean heat storage and global hydrological cycle; however, the relative importance of these two contributions to GMSL variability has remained unclear. Piecuch and Quinn (2016) also raised the question of why the GMSL response to El Niño in 2015/2016 was much stronger than 1997/1998, although these two events were comparable in ENSO amplitude. They speculated in their discussion that other climate modes, like Pacific Decadal Oscillation (PDO), exert an impact on GMSL (Newman et al., 2016).

One factor that makes it difficult to understand the ENSO-related GMSL changes is the presence of decadal modes associated with the climate variability (Zhang and Church, 2012; Hamlington et al., 2019; Moreira et al., 2021). The GMSL showed a sluggish rate of ~ 2.4 mm/yr during the 2000s (WCRP, 2018), despite the ocean gaining mass from ice sheets and glaciers. Climate-driven water exchanges between ocean and land contributed to this slowdown (Cazenave et al., 2014; Reager et al., 2016). This decade-long decrease in GMSL rate is also consistent with a pause in the global mean surface temperature (GMST) increase, which is commonly called as the recent warming “hiatus” (England et al., 2014; Maher et al., 2018). The global ocean has been suggested to absorb extra heat because of anthropogenic radiative forcing during the hiatus period (Chen and Tung, 2014). However, more recent analyses and observations revealed that the ocean heat uptake has slowed down over the 2000s hiatus as compared to the recent decade after 2011 (Xie et al., 2016; von Schuckmann et al., 2020; Loeb et al., 2021). The rate of GMSL is increasing again since about 2011 (Figure 3.1.1) (Yi et al., 2015; Moreira et al., 2021), along with a shift in the Pacific climate variability that has been shown to play a role in GMSL acceleration occurring on decadal time scales (Hamlington et al., 2019). Based on analyses of ocean temperature data, von Schuckmann et

al. (2020) revealed that the rates of ocean heat gain have been steadily increased over the past decades, but a rapid increase after the recent hiatus. More recently, a comparison between satellite observations of top-of-atmosphere (TOA) net radiation and in situ observations showed a decadal increase in EEI from mid-2005 to mid-2019 (Loeb et al., 2021). These results indicated that heat gain in the oceans is increasing over the recent decade, but a direct comparison with the sea-level budget components and their relationship with natural climate variability is lacking.

Because the ocean stores over 90% of EEI in the form of ocean heat content (OHC) and reflects the changes in mass between the ocean and land, natural changes in OHC and exchange of water mass significantly affect the decadal trends of GMSL rise. Therefore, estimating climate-driven sea-level variations is essential to improve our understanding of ocean responses to the global climate system and associated rising sea levels in the future. Despite the significance of determining GMSL and its changes, the following aspects still remain unclear: (i) what are the internal modes that represent the changes in the GMSL rate on decadal timescales (Hamlington et al., 2019); (ii) how and to what extent does the ENSO interacts with decadal-scale fluctuations in the GMSL rate (Piecuch and Quinn, 2016); and (iii) what is the ocean's role in the Earth's energy budget (Llovel et al., 2011; Johnson et al., 2016). Herein, these issues are discussed by considering the influence of the Earth's energy storage and global hydrology during the closure of sea-level budget.

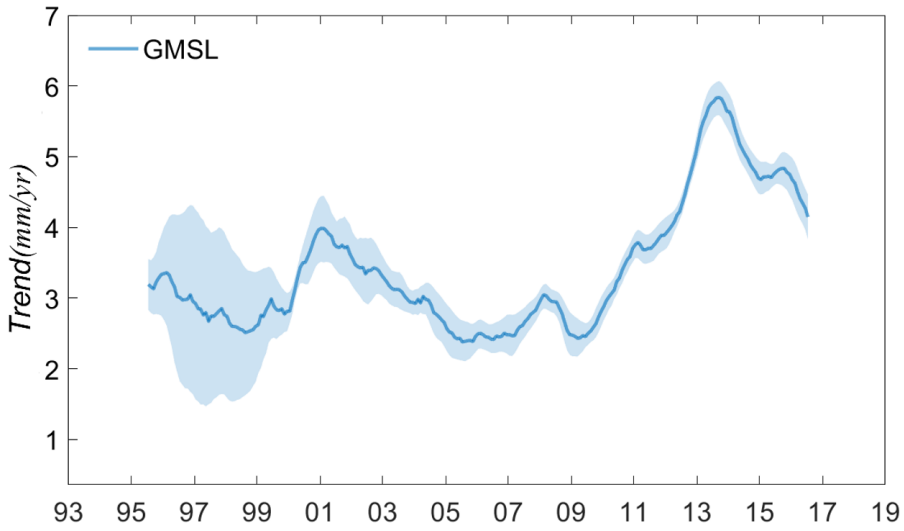

Figure 3.1.1. Temporal evolution of the GMSL rise rate with a moving average of 5 years. The GMSL rise rate was slowed from the early 2000s and increasing again after about 2011.

3.1.2. Data and Methods

3.1.2.1. Datasets

We considered six different altimetry GMSL products from 1993 to 2018 to estimate GMSL budget during the altimetry era. These products were corrected for the effect of glacial isostatic adjustment and TOPEX-A instrumental drift (see details on the altimetry-based sea-level products in section 2.1). For a steric component of GMSL, we used three following reanalysis products: Ishii and Kimoto (2009) (hereafter IK), EN4 product from Good et al. (2013), and NOAA product from Levitus et al. (2012) for 1993 to 2017, except for IK available until 2012. After 2005, three Argo products from the Japan Agency for Marine-Earth Science and Technology (JAMSTEC), International Pacific Research Center (IPRC), and the SCRIPPS Institution of Oceanography (SCRIPPS) were also considered. Because of the Reanalysis (Argo) products are only available from the surface to 700m (2000m), the estimate for the deep ocean contribution of 700–2000m (Chambers et al., 2017) and deep ocean contribution (Purkey and Johnson, 2010) was added over the whole datasets. For Greenland and Antarctica ice sheets, the Ice sheet Mass Balance Intercomparison Exercise (IMBIE) datasets are used in this study. The IMBIE provides an estimate of Ice Sheet data by using satellite altimeters, gravity and input-output method (Shepherd et al., 2012). Four global glaciers products were considered to estimate the contribution to GMSL (Cogley et al., 2009; Leclercq et al., 2011; Marzeion et al., 2015; Zemp et al., 2019). For LWS, the GRACE mascon (JPL RL06Mv2) solution from 2002 to 2017 is used in this study. Prior to the GRACE launch, the reanalysis datasets from MERRA (Reichle et al., 2011) and MERRA-2 (Reichle et al., 2017) were considered (see more details on steric and mass datasets in section 2.1). Altimetry based GMSL and each component are shown in Figure 3.1.2.

To find relationship between the GMSL and climate variability, we used the following

climate data: PDO, MEI, and Sunspot Number. PDO is defined as the leading principal component of monthly sea surface temperature variability over the North Pacific, representing climate variability not only over the North Pacific but also at a global scale (Moreira et al., 2021). Monthly PDO timeseries is obtained from JISAO (available at http://research.jisao.washington.edu/pdo/). MEI is composed from six different variables (sea level pressure, sea surface temperature, zonal and meridional wind, and long wave radiation) over the tropical Pacific. The MEI data is available at NOAA web (https://psl.noaa.gov/enso/mei.old/table.html). To identify the relationship between GMSL and Sunspot activity, which modulates the amount of total solar irradiance and fluctuated energy flux in the earth climate system (Trenberth et al., 2014), we also used monthly sunspot number data obtained from SILSO (http://www.sidc.be/silso/datafiles).

To examine satellite-observed Earth's energy storage, the Top of Atmosphere (TOA) net energy storage anomalies are obtained by time-integrating the TOA net energy flux data from the Clouds and the Earth's Radiant Energy System (CERES) Energy Balanced and Filled (EBAF) Ed4.0 product (https://ceres.larc.nasa.gov/data/#energy-balanced-and-filled-ebaf).

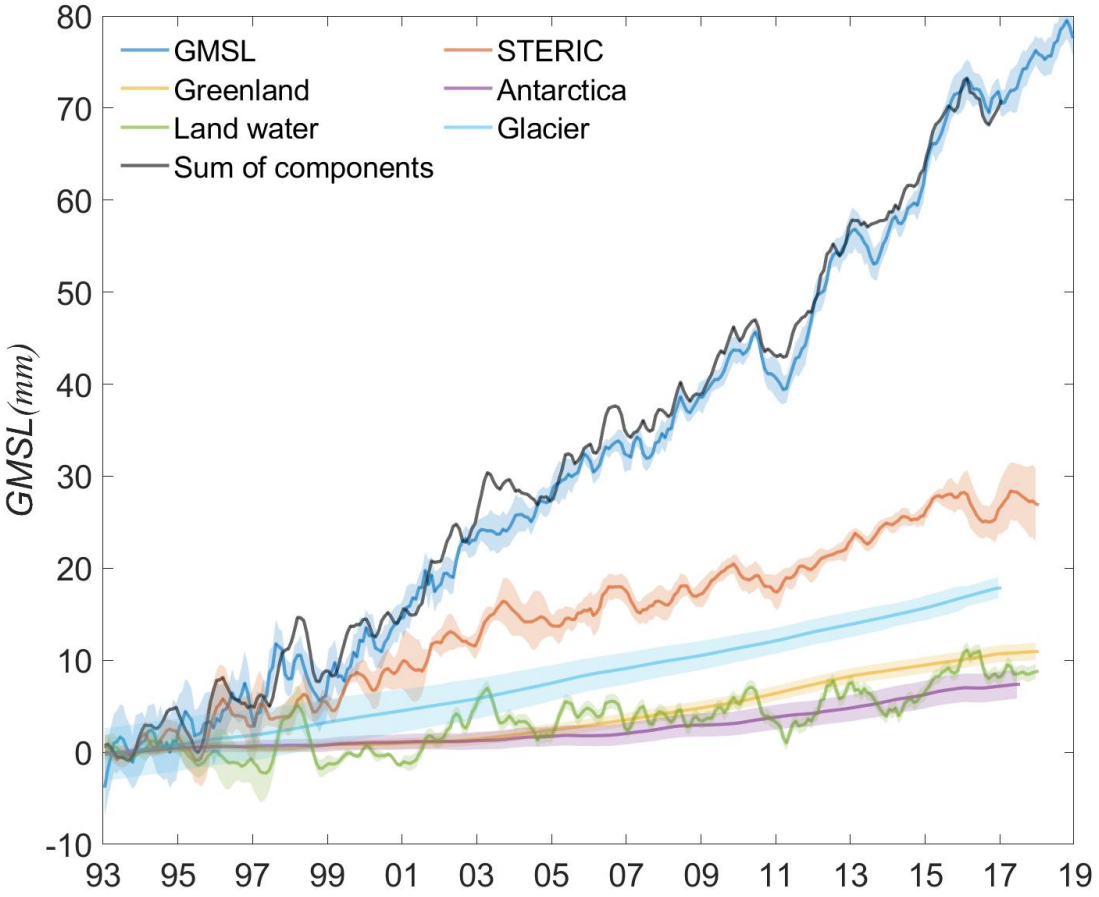

Figure 3.1.2. Time series of all sea-level components, including the ensemble mean GMSL for six groups and individual components. More details in section 2.1.

3.1.2.2. Methods

To extract time-varying trends in all components of sea-level budget, we used an ensemble empirical mode decomposition (EEMD) method, which has been widely used in many geophysical climatology applications (Huang and Wu, 2008; Ezer, 2013; Ji et al., 2014; Chen et al., 2017). The EEMD is an advanced method that improved the mode mixing problem in empirical mode decomposition (EMD). This method is designed to separate the original signals into several intrinsic mode functions (IMFs) and a secular trend, i.e., a residual (Huang et al., 1998). The IMFs of EEMD have been acquired as an ensemble average of IMFs separated from the original data sets added by Gaussian white noise. Figure 3.1.3 shows the EEMD results for all components, which demonstrate seven IMFs and residual trend in ascending order from high to low frequency. Based on spectral analysis, the EEMD-derived IMFs can be grouped into four major time-scale components: High-frequency, ENSO-scale Interannual variability, decadal-scale variability and a residual as the intrinsic trend. Details about EEMD method is given in section 2.3.

The significance of the intrinsic trend and variability is tested using a standard bootstrap method (Mudelsee, 2010). This method is based on random resampling to estimate confidence intervals. The main steps in this method are as follows: 1) create artificial resampled data (ε_{rand}) by randomly sampling the anomaly for the original data; 2) add the artificial data to the residual ($x^* = \varepsilon_{rand} + R$); 3) perform the EEMD again on the reconstructed data (x^*) to obtain the artificial trend; 4) repeat the steps 1–3 for M times (in this study, M=1,000 iterations) and the mean artificial trend ($\overline{R^*}$) can be estimated from individual bootstrap simulations:

$$\overline{R^*} = \frac{1}{m}\sum_{i=1}^{M} R(x_i{}^*) \qquad (3)$$

Figure 3.1.4 show the rates of intrinsic trends and decadal variability in each component, with a 95% confidence interval (within two standard deviations) for 1,000 randomly sampled trends

and decadal modes. The time-varying trends and decadal modes in all components do not change significantly within their confidence intervals, indicating robustness of the EEMD-derived trend and decadal mode.

The intrinsic trend is the same unit as the raw time series, and the rate of time-varying trend is obtained by taking the first-order time derivative of the trend in mm/yr for GMSL. Time-varying rate associated with the intrinsic trend of each time series, which was determined by calculating the temporal derivative of the trend (i.e., residual mode), has been presented in Figure 3.1.4a. A bootstrap method, which is based on random resampling to estimate confidence intervals, is used to test the significance of the intrinsic trends obtained from EEMD. It is shown that the time-varying trends in all components do not change significantly within their confidence intervals, indicating robustness of the EEMD-derived trends. The trend rate from the sum of all components of GMSL budget increased from 2.3±0.3 mm/yr in 1993 to 3.8±0.3 mm/yr in 2017. The volumetric expansion due to ocean warming occupied 53% of the sum of the contributions in 1993; however, it reduced significantly to 29% of the total contributions in 2016. In contrast, the mass inflow to the ocean due to exchange of water mass between land and ocean exhibited an increasing contribution to GMSL from 47% in 1993 to 71% of the total contributions in 2016, with the largest increase coming from the contribution of the Greenland ice sheet (GIS). These trends are consistent with a previous estimate of the time-varying trends (Chen et al., 2017) that showed changes in relative contributions of steric and mass components.

In addition, to test whether the decadal-scale component was affected by the ending point effect including a significant event like El Niño, we compared the decadal-scale components of full record length with gradually shortened records of the same datasets by removing 0–3 years of data from the end of the time series (Figure 3.1.5); this has also been done in previous

studies (Cha et al., 2018, Chen et al., 2014). The amplitudes of decadal-scale components from satellite altimetry, steric, and LWS show insignificant changes; however, their decadal signal persisted regardless of the impact of the El Niño event in 2015/16, indicating that the decadal-scale variability is robust in the GMSL.

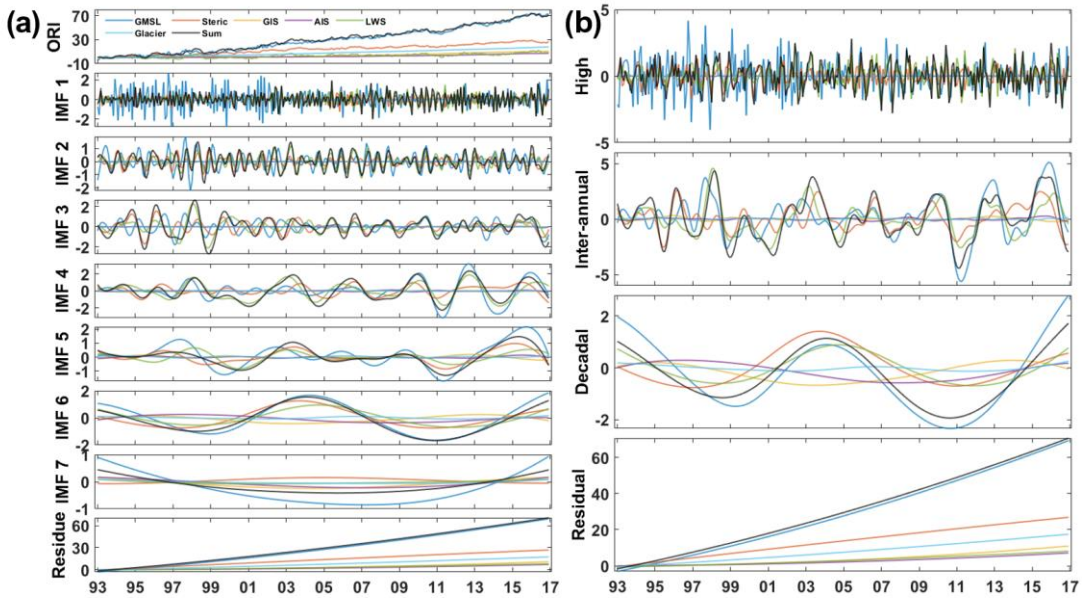

Figure 3.1.3. EEMD results for all components of global mean sea-level budget. (a) All of the original monthly data (top) are decomposed into seven intrinsic mode functions (IMFs) and the resulting trends (bottom) in ascending order. (b) Four major time-scale components representing high-frequency (IMFs 1–2), ENSO-scale frequency (IMFs 3–5), decadal-scale frequency (IMFs 6–7), and residual.

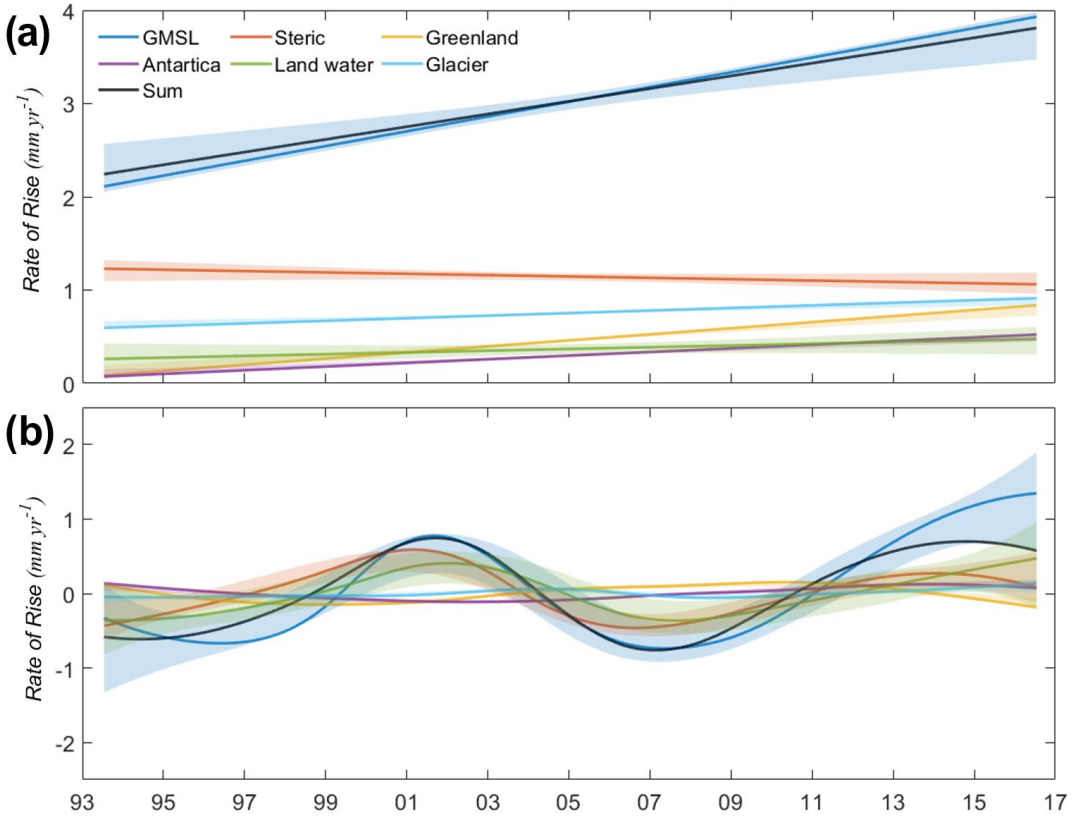

Figure 3.1.4. The instantaneous rate of GMSL (a) The instantaneous rate of GMSL trend from EEMD analysis. (b) The instantaneous rate of GMSL decadal-scale of each component. A bootstrap method based on random resampling to estimate confidence intervals (coloured shades) is used to test the significance.

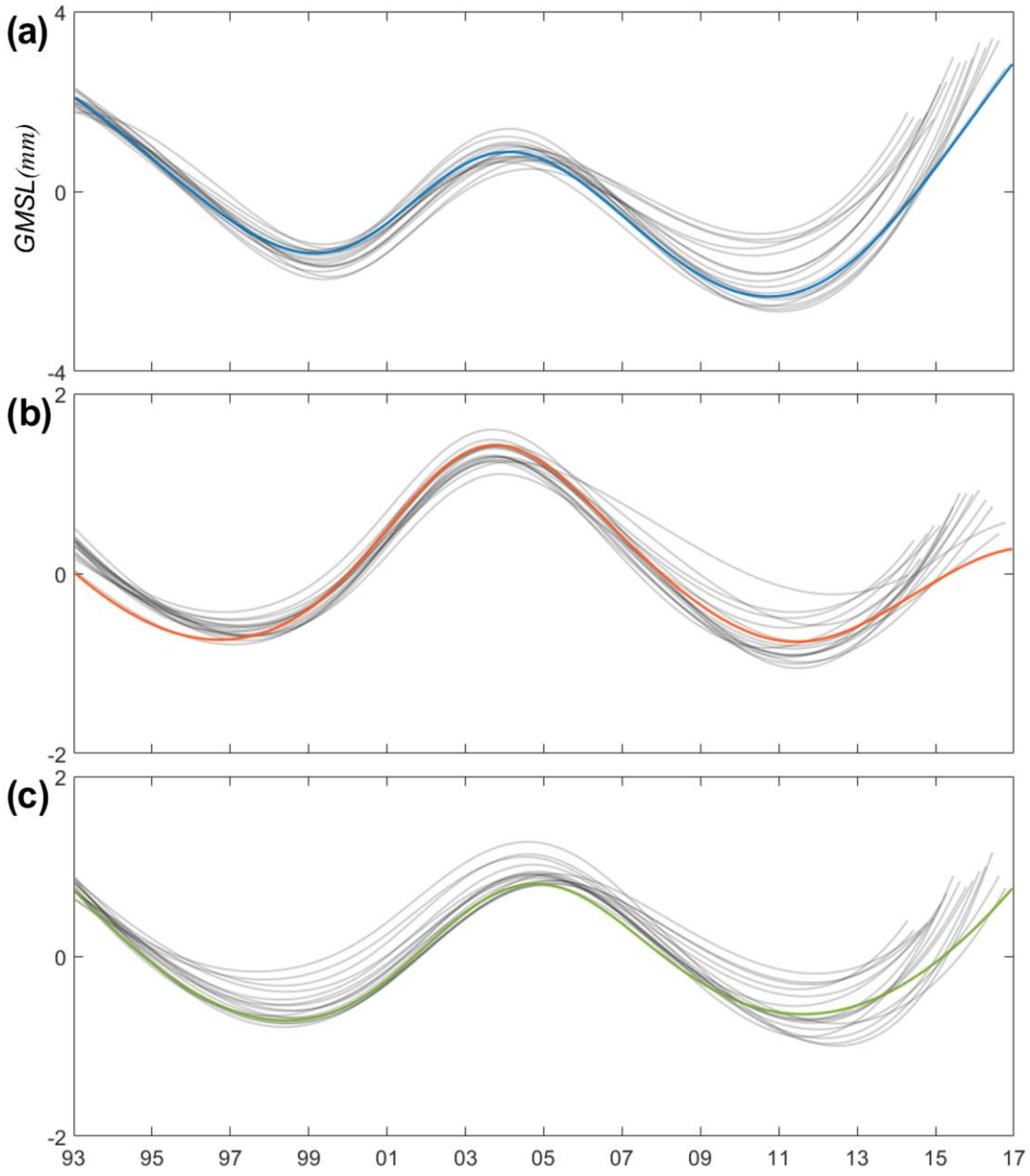

Figure 3.1.5. Robustness of decadal-scale variability. Decadal modes of the full record length from (a) satellite altimetry-based GMSL, (b) steric sea level, and (c) LWS components and incrementally shortened records (grey lines) of each component by removing 0–3 years of data from the end of the time series.

3.1.3. Decade-long fluctuation in GMSL

3.1.3.1. Temporal evolution of sea-level rise rate

We assessed the GMSL budget in terms of different contributions, using a number of available datasets for altimetry-based sea levels as well as mass and steric components (Figure 3.1.6). Ensemble means were applied for all sea-level budget components. The temporal evolution of altimetric GMSL agrees well with the sum of all the components (Figure 3.1.6a, upper) and the linear trend difference between the two GMSLs is small (0.01 mm/yr), thereby representing the GMSL budget closure and consistency of different datasets. These records show the sea-level fluctuations superimposed on the dominant background trend, with particularly significant ENSO-related changes in the GMSL rise.

This study focused on the 2000s, when GMSL rise rate slowed, and after 2011, when it increased (Figure 3.1.1). To diagnose the temporal change of sea-level rise rate over recent decades, we extracted decadal-scale variability from all components of the GMSL budget by using EEMD method. Throughout the altimeter era, a distinct decade-long fluctuation with a peak period of ~12 years was identified in the ensemble mean GMSL as well as in the sum of all components (Figure 3.1.6b, upper), which were in phase with a downward shift during the recent hiatus in the 2000s and in phase with an upward shift subsequently (Figure 3.1.6b, bottom). Without an intrinsic trend (i.e., a residual trend), the GMSL rates display a transition trend from positive to negative during the surface warming slowdown; however, this trend transitioned back to positive in 2011 (see Figure 3.1.4b), which corresponds to a recent resumption of surface warming after the decade-long hiatus (Hu et al., 2019; Lenssen et al., 2019). This decadal fluctuation extracted from the EEMD method is also supported by the first mode of the Empirical Orthogonal Function (EOF) analysis, which is derived using a successive 5-year running mean of the altimetric sea-level data with a linear trend removed

(Figure 3.1.7). The decadal pattern from the EOF analysis is very similar to a decadal fingerprint, which is represented by the sea-level regression in regard to the EEMD-determined decadal mode (Figure 3.1.8a), indicating the robustness of decadal sea level variability from EEMD analysis. These results show that the decadal GMSL fluctuation is separated from the interannual modes (i.e., periods of 3–7 years) and the intrinsic trend, thereby supporting the results of previous studies that have used different methods; e.g., the multiple linear regression (Zhang and Church, 2012; Moreira et al., 2021) and the cyclo-stationary EOFs (Hamlington et al., 2017, 2019).

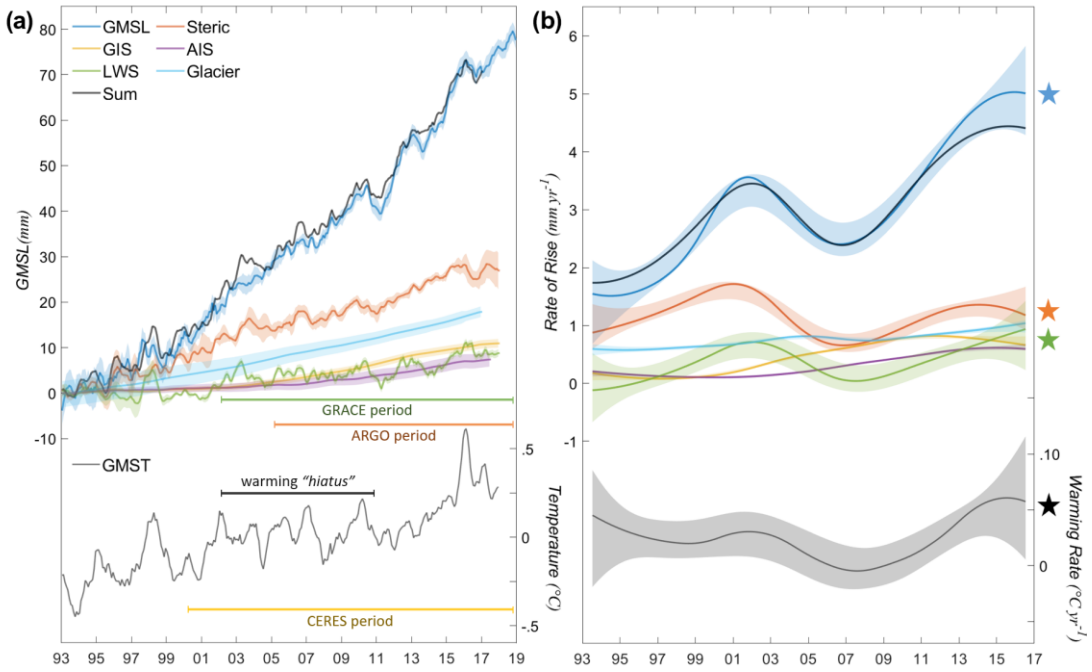

Figure 3.1.6. (a) Time series of all sea-level components (upper) and GMST (bottom), including the ensemble mean GMSL using altimetry data from six processing groups (blue), sum of ensemble mean components (black), individual ensemble mean components, and GMST using the Goddard Institute for Space Studies Surface Temperature Analysis v4. Uncertainties are based on the dispersion among different time series around the mean (colored shades). (b) Instantaneous rate of GMSL trend with decadal variability (upper) and GMST trend (bottom) from EEMD analysis. A bootstrap method based on random resampling to estimate confidence intervals (colored shades) was used to test the significance. Time series with decade-long fluctuations are highlighted (star symbols).

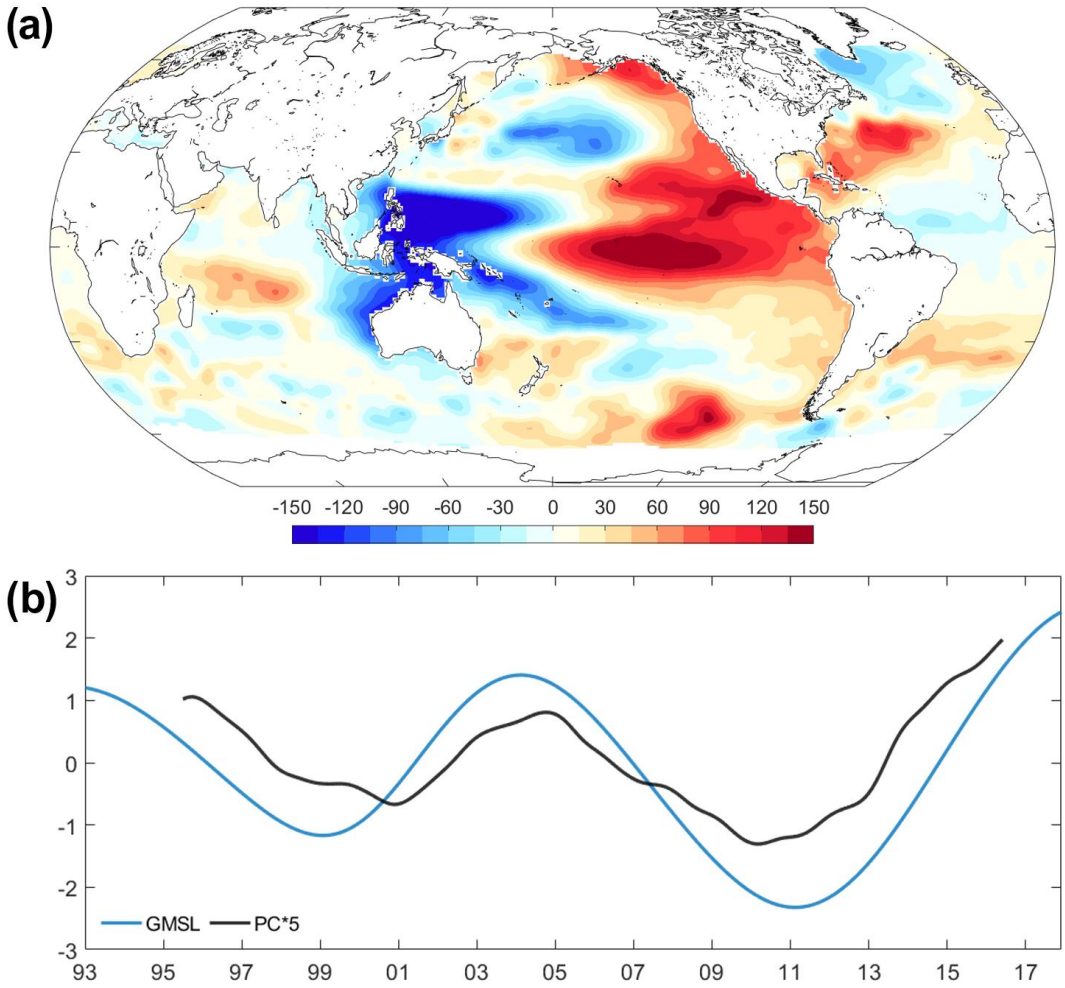

Figure 3.1.7. The 1st mode of the EOF decomposition. (a) Spatial pattern of the 1st mode of the EOF decomposition. (b) EEMD-determined GMSL decadal variability and principal component (PC) of 1st mode. To compare with decadal GMSL, PC time series is multiplied by five.

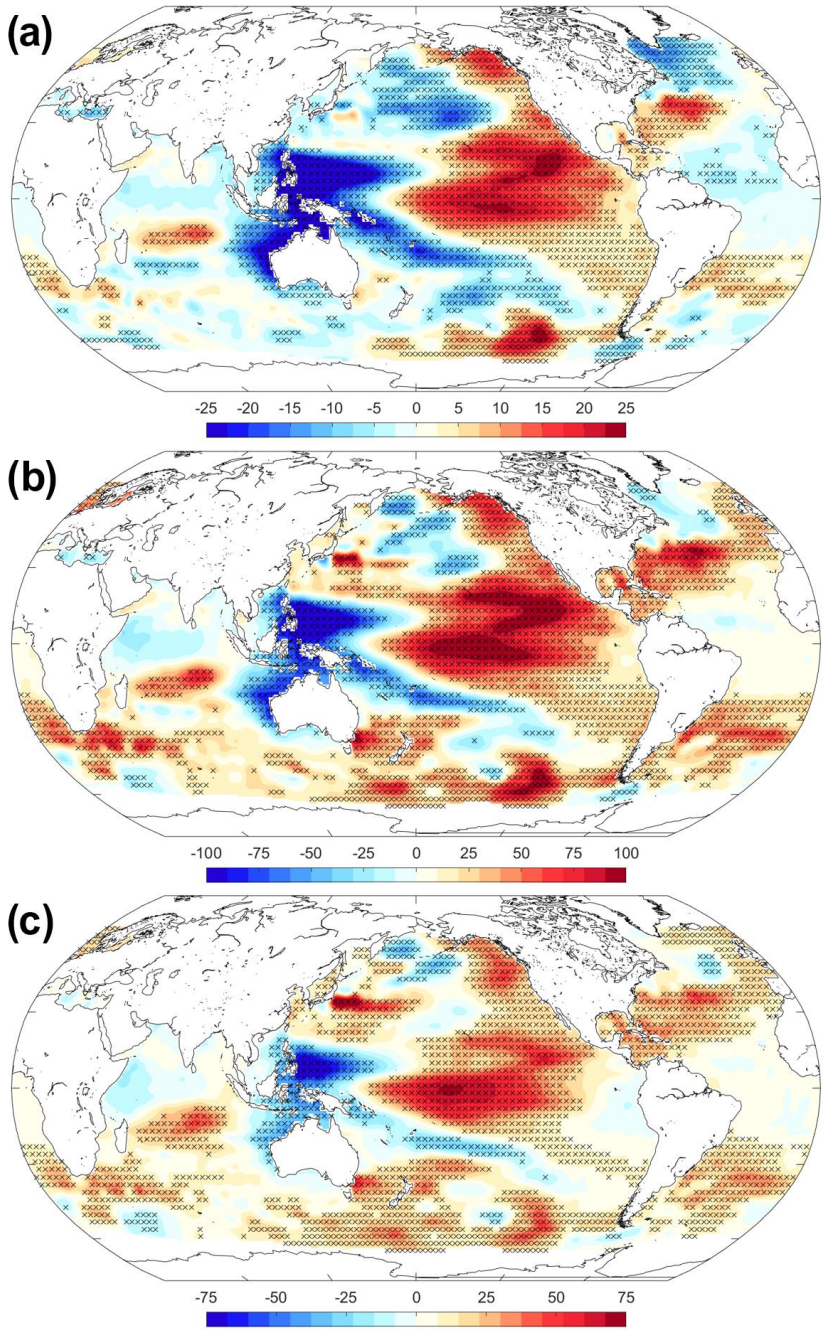

Figure 3.1.8. The sea level fingerprint with respect to decadal variability. Regression patterns of CSIRO sea level onto the decadal mode of (a) GMSL, (b) PDO, and (c) Sunspot number signals in Figure 3.1.9. Sunspot number signal was lagged by 30 months. The cross-symbol areas indicate significance at the 95% confidence level determined using Student's t-test.

3.1.3.2. Decadal GMSL fluctuation associated with Pacific climate variability

We further identified a strong relationship between the decadal modes of sea-levels and the Pacific decadal variability obtained from the EEMD of the PDO (Figure 3.1.9). Over the altimeter period, the transition times agreed well between the sea level components and the Pacific decadal variability, showing a distinct transition around 2011 that is consistent with the recent resumption of surface warming after the 2000s hiatus. The Pacific decadal mode has its largest correlation with both the GMSL and steric sea level at near-zero lag; however, there is a 7-month lag with the LWS. The spatial patterns of the regressed EEMD-derived decadal GMSL and PDO mode are also agree (Figures 3.1.8a and b), suggesting a relationship between sea level and natural variability on decadal timescale. This suggests that the climate-driven decadal mode strongly contributed to slowing the GMSL rise rate during the hiatus and increasing the trend rate after the hiatus. Furthermore, there is a possible link between these climate-driven fluctuations and sunspot activity (dashed red line in Figure 3.1.9), which is known to exhibit a cycle that lasts approximately 11 years (Hathaway, 2015). It has been noted that the cycle of solar forcing can be amplified to produce a measurable climate response on decadal timescale through at least two mechanisms of 'top-down' stratospheric response and 'bottom-up' coupled ocean-atmosphere surface response (e.g., White et al., 1997; Kodera and Kuroda, 2002; Haigh et al., 2005; Matthes et al., 2006; Meehl et al., 2009). The sunspot activity on a decadal timescale is in phase with the Pacific decadal variability and the GMSL fluctuation, but their correlations lag at a maximum of ~30 months. This relation is evident from the regression pattern of sea level onto the decadal sunspot activity (Figure 3.1.8c), which shows that there is oceanic response to the solar cycle on decadal timescales. Previous observational and modeling studies have shown a delayed surface response at 1−3 years after the solar cycle (Gray et al., 2013; Hood et al., 2013) and proposed a mechanism that involves interaction between atmosphere and OHC in the mixed layer (Scaife et al., 2013; Misios et al.,

2016). More recently, analysis by Lin et al. (2021) identified the solar activity-induced the SST footprint in Northeast Pacific that modulates the background surface temperature in the Pacific and the associated central Pacific ENSO activity on decadal timescales. However, there are still some uncertainties, not only in the reliability and characteristic of observational solar activity signals but also in understanding of the mechanisms (e.g., Gary et al., 2013). Because of the complex processes in air-sea feedback, the physical mechanisms that lead to the impact of the solar cycle on the climate are not fully understood, and thus further investigations are required in the future; nevertheless, the findings from previous studies showed that the solar cycle on decadal timescale can be a relevant source of decadal climate variability both on global and regional scales. These comparisons suggest that the decadal fluctuation in GMSL reported here is a distinct and robust signal associated with the earth's climate system, which is different from the ENSO-related interannual variability.

We also note that the climate decadal mode can result in the modulation of GMSL response to ENSO events (Figure 3.1.10). The El Niño in 2015/2016 was one of the strongest events in history, which was comparable to the El Niño events in 1997/1998. The strengths of amplitude were comparable between these two events; however, the sea-level response to El Niño was weaker during the 1997/1998 El Niño than during the 2015/2016 El Niño (Figure 3.1.10a) as previously discussed in Piecuch and Quinn (2016) and WCRP (2018). To examine how the decadal mode modulates with the GMSL response to ENSO events, the contributions of interannual and decadal variability to the observed three-month mean GMSL (with an intrinsic trend removed) were analyzed (Figure 3.1.10b). The decadal mode contributed to ~23% of a decline in GMSL during the El Niño in 1997/1998, but made a positive contribution of ~21% to the GMSL rise in the 2015/2016 El Niño. With the decadal mode removed, the sea-level responses to the two strong El Niño events show a similar amplitude (~5.3 mm in 1997/1998 and ~5.4 mm in 2015/2016). The decadal mode also has a positive contribution (~28%) to the

largest decline in the 2010/2011 La Niña, as discussed in previous studies (Boening et al., 2012). Our analysis shows that the GMSL responses to ENSO can be depressed or amplified by the relation with the Pacific decadal mode. Recent studies suggested the differences in underlying dynamics between the 1997/1998 and 2015/2016 extreme El Niños (Paek et al., 2017; Long et al., 2020). Peak et al. (2017) argued that the 2015/2016 event is not a pure tropical forced Eastern Pacific (EP) El Niño but a mixture of the EP and the Central Pacific (CP) El Niños, emphasizing the CP El Niño dynamics more affecting on the 2015/2016 event than on the 1997/1998 event. Unlike the EP El Niño, the CP El Niño events include strong decadal signals associated with air-sea feedback in mid-latitudes and Pacific climate modes (Chiang and Vimont, 2004; Yu and Kim, 2011) and become more remarkable after 1980s (Lee and McPhaden, 2010). The atmospheric circulation and global water cycle from the CP El Niños may contribute more to the GMSL fluctuation on decadal time scale, leading to higher sea-level in 2015/2016 event than in 1997/1998 event.

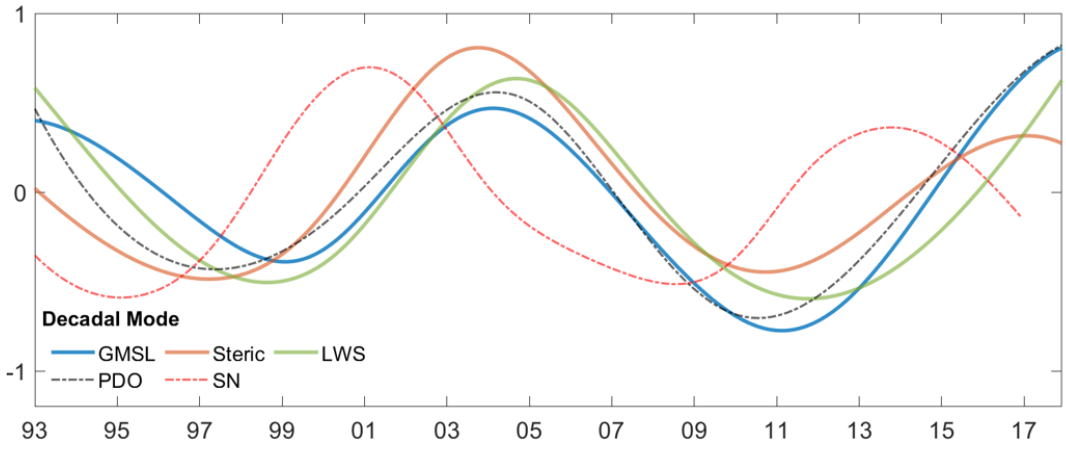

Figure 3.1.9. Timeseries of decadal modes in GMSL (blue), Steric (orange), LWS (green), PDO (dashed black) and Sunspot number (dashed red) over 1993–2017. These decadal modes are extracted by EEMD method from original timeseries of each component. Each timeseries are normalized by their standard deviation for comparison.

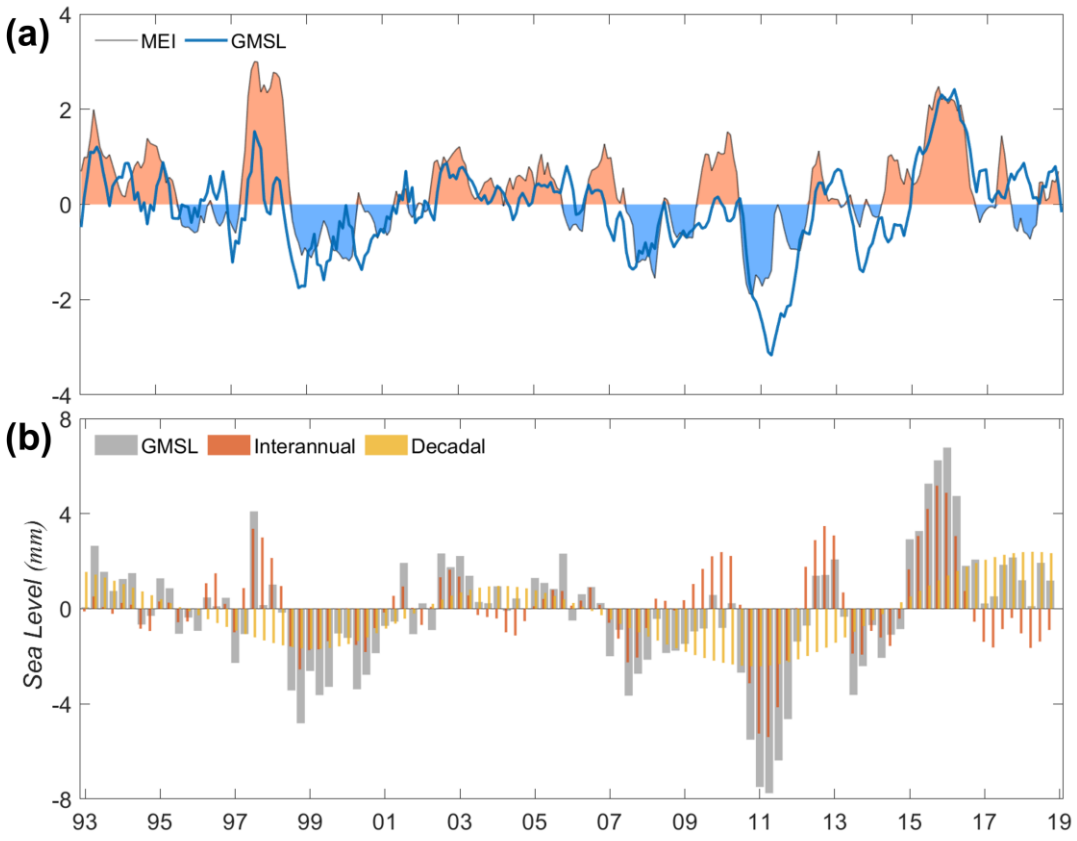

Figure 3.1.10. Contribution of decadal mode to GMSL response to ENSO. (a) Monthly timeseries of GMSL with an intrinsic trend removed (blue) and MEI index (shading) over 1993-2018. Each timeseries are normalized by their standard deviation for comparison. (b) three-month averaged GMSL (grey bar) and the contribution of each EEMD-derived interannual (red bar) and decadal (yellow bar) mode to the GMSL.

3.1.4. Climate-driven Land water storage

To investigate the response of global hydrology and ocean heat storage to climate decadal variability, the following two decadal periods were compared: 2002–2010 (i.e., hiatus period) and 2011–2017. Prior to the Gravity Recovery and Climate Experiment (GRACE) record that extends back to 2002, global hydrological models estimated the trend and fluctuation of total LWS. However, there were still uncertainties regarding the ability of model to simulate the interannual to decadal variability in global LWS (Scanlon et al., 2018). Moreover, the uncertainty in the OHC calculation that arises from insufficient sampling and instrumental biases was mainly observed for the period before the early 2000s; that is, the pre-Argo period (Durack et al., 2014). Therefore, we used the GRACE and Argo-based products to estimate the global patterns of decadal trends in the LWS and OHC for the two analysis periods. The global estimate of the GRACE trend over 2002–2010 revealed an increasing LWS (wetting) at low latitudes, and decreasing LWS (drying) at the mid-latitude of the southern hemisphere (Figure 3.1.11); these results coincides with previous GRACE studies (Chen et al., 2010; Reager et al., 2016). The latitudinal trends in LWS shifted since 2011 and showed a distinct pattern of low latitude drying and mid-latitude wetting, which is more prominent in the southern hemisphere. The decadal trend shift resulted from changes in the LWS regime since 2011; that is, the wet conditions transformed to dry conditions at low latitudes, while the opposite effect was observed at mid-latitudes (Hamlington et al., 2017). The spatial distributions of the LWS trend strongly resembled the LWS pattern regressed on the EEMD-determined decadal mode of the PDO (Figure 3.1.12a), thereby implying an important decadal persistence in the Earth's climate systems (Hamlington et al., 2017). The GRACE-derived LWS was consistent with the observed land precipitation from the Global Precipitation Climatology Project (GPCP) in the decadal trends and in its interannual variations throughout the GRACE period (Figure 3.1.11c). There was a delayed (maximum correlation at 7 months)

response of LWS to the precipitation in land. When the precipitation falls onto land, much of it soaks into the ground as infiltration and some water infiltrates deep into the ground and recharges groundwater in aquifer. This process can make a time lag response of LWS to precipitation (Eagleson, 1978). Previous studies demonstrated a delayed response between LWS and precipitation (Humphrey et al., 2016; Zhang et al., 2019). The lags between LWS and precipitation are about 1−3 months in the low- and mid-latitude basins. However, the effect of seasonal snowpack accumulation and the melting process causes the longer lag (6−9 months) response of LWS to precipitation at high latitude (Humphrey et al., 2016; Zhang et al., 2019).

The glacier-free LWS contributed 0.14±0.11 and 1.04±0.21 mm/yr to the sea level rise during the first and second decades of the GRACE period, respectively (Figure 3.1.13). Because the net LWS changes estimated here include human- and climate-driven components in storage, an Intergovernmental Panel on Climate Change (IPCC) estimate (IPCC, 2013) of direct human-induced LWS changes (0.38±0.12 mm/yr) was used to calculate the climate-driven LWS contribution to GMSL (Reager et al., 2016). Therefore, the climate-driven LWS suppressed the GMSL rise (-0.23±0.16 mm/yr) during the hiatus period and subsequently enhanced it (0.66±0.24 mm/yr), which suggests that the natural LWS variability significantly contributed to the decade-long shift in the GMSL. These LWS changes determined by GRACE indicate that naturally occurring variability in precipitation leads to decadal variations in the water exchange between ocean and land, thereby supporting the findings of several studies mentioned above.

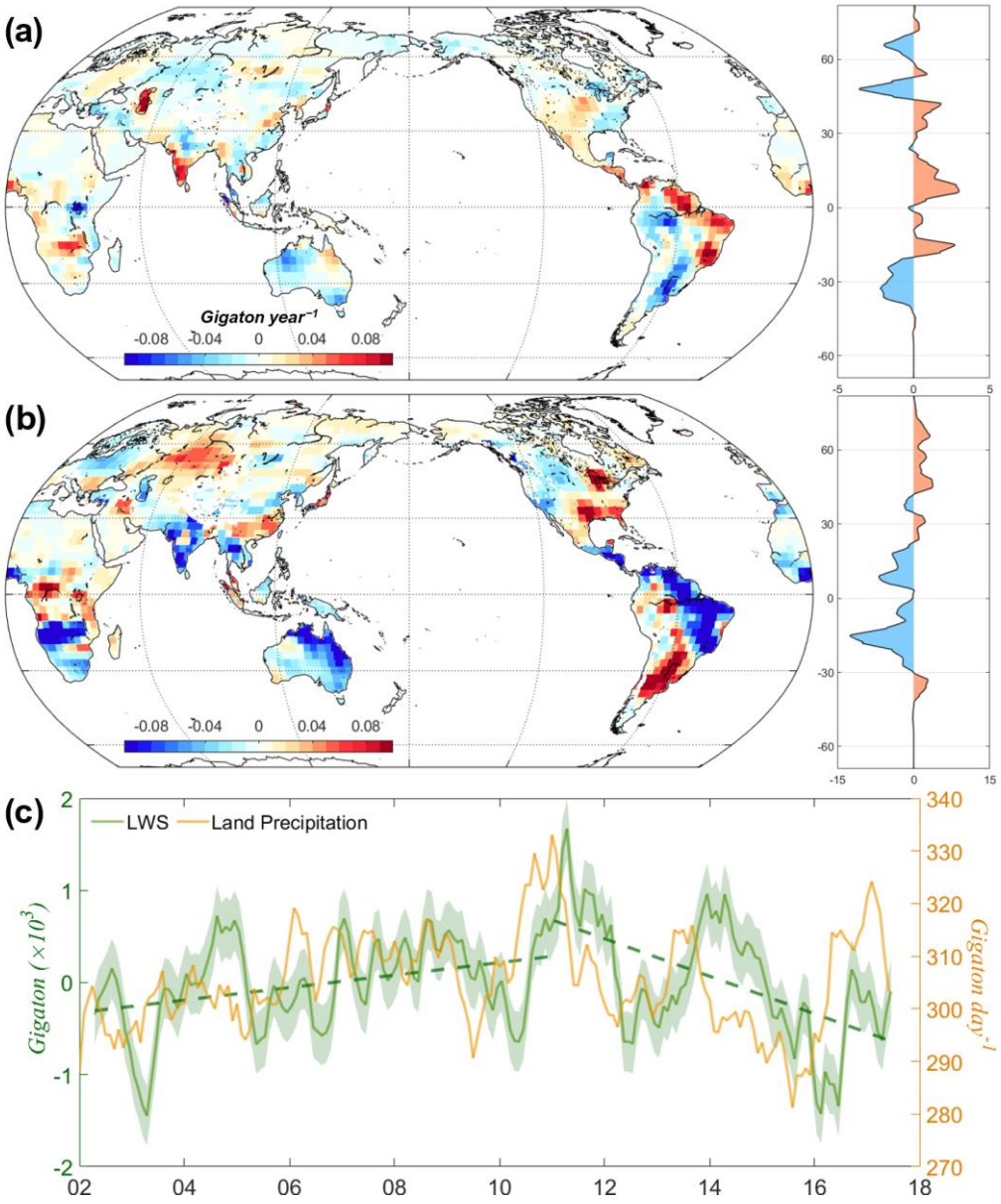

Figure 3.1.11. Global map of LWS trend (gigatons per year) and its zonal total trend (gigatons per year per 1/2 degree grid) in (a) in 2002–2010 and (b) 2011–2017. (c) Time series of global LWS (green) from GRACE and land precipitation (yellow) from GPCP. The linear trend throughout the GRACE period was removed to highlight climate-driven decadal trend shift in LWS. The dashed lines indicate the linear trends in 2002–2010 and 2011–2017. The LWS uncertainties are shown in colored shades.

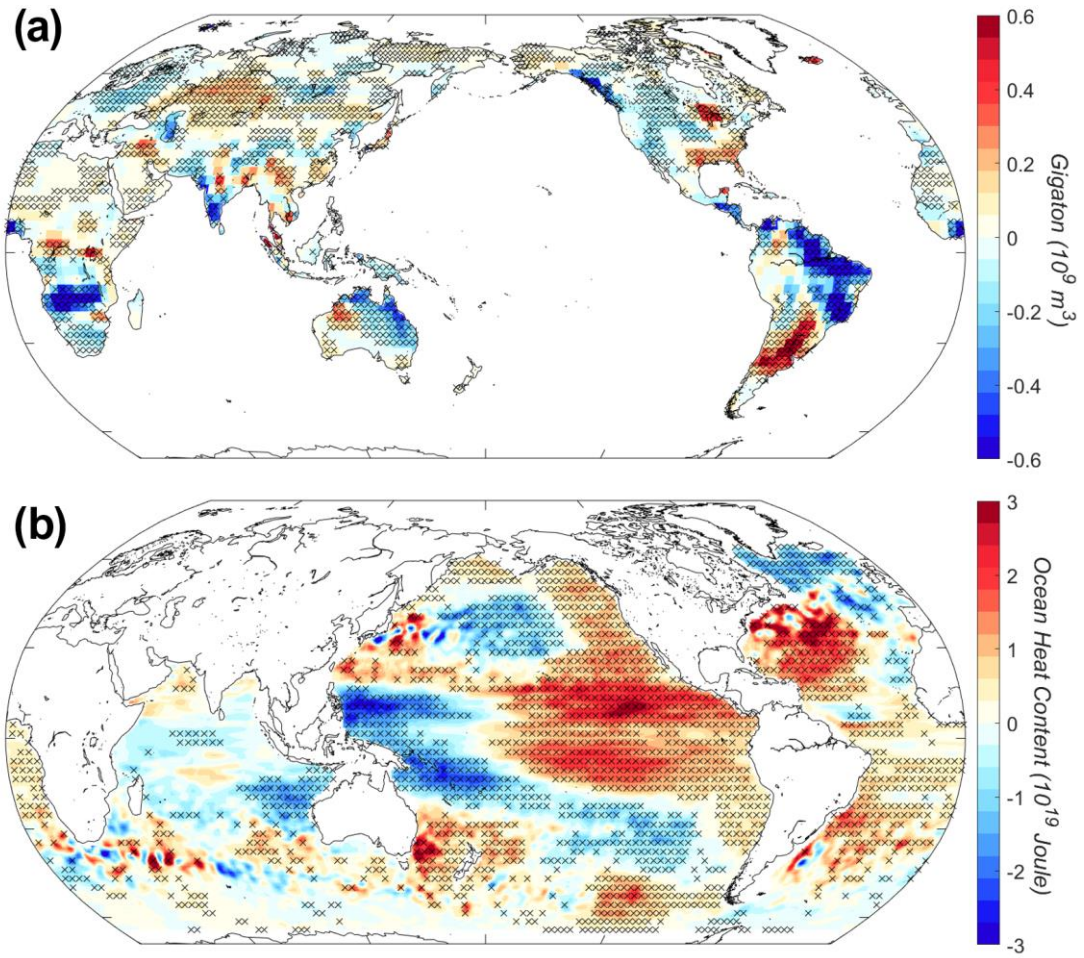

Figure 3.1.12. Global LWS and OHC fingerprints with respect to the PDO. (a) LWS and (b) OHC (0-2000 m) regressed onto the decadal mode of the PDO (shown in Figure 3.1.9) over 2002–2017 and 2005–2017, respectively. Data sources are GRACE mascon solution (JPL RL06Mv2) for LWS and SCRIPPS for OHC, respectively. The cross-symbol areas indicate significance at the 95% confidence level determined using Student's t-test.

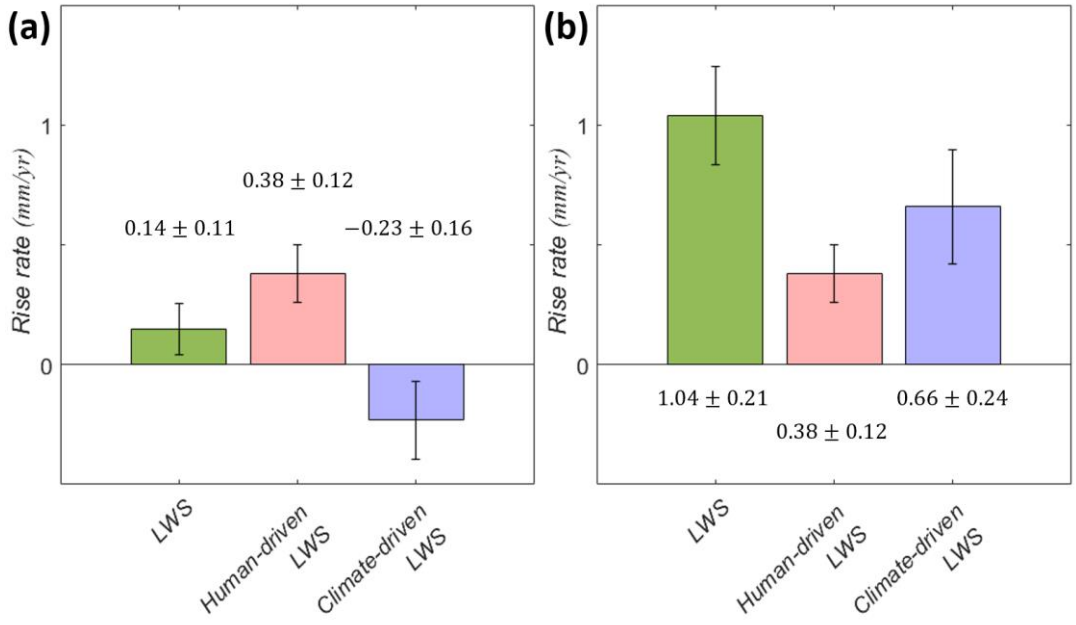

Figure 3.1.13. Disaggregation of net LWS terms over (a) 2002–2010 and (b) 2011–2017. Left bar: Glacier-free LWS, middle bar: human-driven LWS estimated by IPCC AR 5 (IPCC, 2013), and right bar: Climate-driven LWS (i.e., subtracting the IPCC estimate for human-driven change). Error bars represent 95% confidence intervals estimated from slope of uncertainty and the quadratic sum.

3.1.5. Ocean effect on the Earth Energy Imbalance

The steric contribution to the rise in GMSL arises from changes in ocean heat content (OHC), which is the major factor sequestering the EEI resulting from rising CO2 concentrations. To elucidate OHC fluctuations contributing to the rate of GMSL rise, we analyzed the temperature profiles recorded by Argo array floats since 2005, which provided a reliable OHC estimate over 0–2000 m (Cheng et al., 2015). The OHC for upper 2000 m is given by:

$$Q = \rho \cdot C_p \iiint \theta \cdot dx \cdot dy \cdot dz$$

where C_p is the specific heat capacity of seawater (4,000 J/kg/K) and ρ is the water density.

Global maps of OHC (derived from the SCRIPPS product) trends over the two decadal periods revealed that since 2011, the trend has been changing toward an opposite trend compared to that of the preceding period (Figure 3.1.14). It is manifest from the regression pattern of the EEMD-determined decadal mode of the PDO that there are global ocean responses to Pacific climate variability (Figure 3.1.12b), which agree with the linear trend patterns of the OHC. In 2005–2010, the OHC showed strong warming trends in the eastern/southeastern Indian and western tropical Pacific oceans; a warming structure was also centered in the western/central North Pacific, and surrounded by cooling along the west coast of North America. With the PDO transitioning back to positive since 2011, the spatial patterns of the OHC trend were reversed; this was accompanied by a positive (warming) trend in the eastern Pacific ocean and a negative (cooling) trend in the western tropical Pacific and northern and southeastern Indian oceans. The Pacific patterns of the decadal OHC trend are linked to the PDO-related trade trends on a decadal timescale, i.e. a strengthening of trade winds during

the 2000s, followed by a weakening trend of trade winds since 2011. Climate-altered trade wind results in changes of the upper-ocean circulations, redistributing heat in the Pacific (Merrifield, 2012; Moon et al., 2013; England et al., 2014; Hamlington et al., 2014; Cha et al., 2018; Maher et al., 2018). The trend reversal was also observed in the North Atlantic, with warming in the subtropical gyre and cooling in the subpolar gyre; this result indicates a significant influence of ocean circulation on heat redistribution. It is worth noting that the decadal OHC trend of subpolar gyre in the North Atlantic may be attributed to the shifts in the melting rate of GIS. For instance, the cooling in the subpolar gyre since 2011 contributed to the slowdown of mass loss in the GIS, which is consistent with the findings of a recent study (IMBIE team, 2020) that identified a persistent increase in ice loss rate prior to 2012. The combined impacts of warming and cooling regions in the OHC resulted in a GMSL fluctuation that can be caused by decadal-scale climate variability.

The other two datasets (i.e., IPRC and JAMSTEC) also show the decadal trend shifts of global OHC, which generally agreed with the pattern of SCRIPPS (Figure 3.1.15); however, we note some differences in magnitude between the Argo products. For example, the largest differences appear along strong current systems, such as the Antarctic circumpolar current in the Indian Ocean and the Gulf stream in the North Atlantic. The SCRIPPS product shows a more negative trend than the other two products in Atlantic Ocean over 2005–2010, while it has a positive trend in the Atlantic and the Pacific Oceans over 2011–2017 (Figure 3.1.16). Overall, the spatial trend between the Argo products over 2005–2010 exhibits relatively large discrepancies compared with the trend over 2011–2017. At the beginning of the data collection process performed using the Argo products, there is a large deviation due to sparse data coverage (Roemmich et al., 2015; Schuckmann and Traon, 2011). These differences between the datasets might be a result of the choices made by the data producers to ensure that mapping strategies with quality-control and vertical resolutions are implemented together with suitable

baseline climatology (Llovel and Terray, 2016; Lyman et al., 2010; Piecuch and Quinn, 2016).

The globally integrated OHC calculated from the surface to a 2000 m, based on the three Argo products, is shown in Figure 3.1.14c. Despite some spread around the ensemble mean, all datasets show an increase in global OHC since 2005, which demonstrates that the estimates of ocean warming are robust. The time series of annual global OHC revealed that the rate of ocean heat uptake was slower prior to 2011 and faster after 2011. The global volume-integrated OHC trend accounts for 59 ± 15 ZJ/decade (1ZJ = 10^{21} J) over 2005–2010, based on the mean estimate for the Argo products. Since 2011, the global upper-2000 m ocean heat rises at a rate of 105 ± 13 ZJ/decade, and oceans gain more heat in comparison with the preceding period. To directly compare OHC with the satellite-observed Earth's energy storage, time-integrated TOA net flux estimated from the Clouds and the Earth's Radiant Energy System (CERES) measurement was used; the Argo-based OHC tracked the phase of the TOA net energy storage reasonably well (Figure 3.1.14d). Yearly variations of global OHC and CERES TOA net energy storage were correlated at 0.53; this was in good agreement with the results of previous works (Llovel and Terray, 2016; Johnson et al., 2016; Johnson and Birnbaum, 2017; Loeb et al., 2021). For the period of 2005–2010, the mean rate of steric sea-level rise estimated from three Argo measurements (i.e., SCRIPPS, IPRC, JAMSTEC) is 0.68±0.23 mm/yr; however, it becomes about two times faster (1.19±0.20 mm/yr) after 2011 (Figure 3.1.17). A previous study has determined the sea level rise (0.75±0.15 mm/yr) based on the thermal expansion trend by using upper-1500 m Argo data for the 2005–2010 period (Schuckmann and Traon, 2011), which is comparable to our estimate within the uncertainties.

To illustrate the OHC contribution to the Earth's energy budget, we estimated the EEI during and after the warming hiatus in terms of the heating rate applied over the Earth's surface area; this was achieved by combining Argo-observed upper-2000 m OHC with previously

published estimates of heat uptake, using the deep ocean and non-ocean terms (Figure 3.1.18). The global volume-integrated OHC trend (Figure 3.1.14c) demonstrates that the planetary heating rates are 0.37 ± 0.15 W m^{-2} over 2005–2010 and 0.65 ± 0.18 W m^{-2} over 2011–2017 (per unit of Earth's surface of 5.1×10^{14} m^2). Considering a constant heating rate of 0.099±0.066 W m^{-2} at ocean depths below 2,000m depth (Purkey and Johnson, 2010), as well as the sum of non-ocean terms by von Schuckmann et al. (2020), we obtained a net heat uptake of 0.55 ± 0.12 and 0.85±0.10 W m^{-2} for 2005–2010 and 2011–2017, respectively. The comparison between the two periods indicates that the global ocean gained more heat energy from 2011 onwards (0.30±0.16 W m^{-2}), as compared with the previous period. The EEI estimated from the latest release of CERES satellite data was 0.60±0.10 W m^{-2} for 2005–2010 and 0.95±0.10 W m^{-2} for 2011–2017, which indicates a close correspondence between two completely independent EEI estimates on decadal time scales. These EEI estimates were not distinguishable within the uncertainty and thus, the increase in the ocean heat uptake since 2011 seems to be robust. The benefits of these two independent approaches are also demonstrated in a recent study by Loeb et al. (2021) that showed a robust positive trend in EEI from mid-2005 to mid-2019 due to mainly changes in clouds, water vapor, and trace gases. Figure 3.1.18 further demonstrates the agreement with the EEI obtained from the altimetry minus GRACE residual approach (Fu, 2016; Levitus et al., 2012). These results enhance the confidence in all three complementary climate observing systems (Meyssignac et al., 2019). Furthermore, the consistency shown here suggests that there was no shortfall in closing the global energy budget during the 2000s; this was in contrast to the so-called "missing energy" problem (Trenberth and Fasullo, 2010).

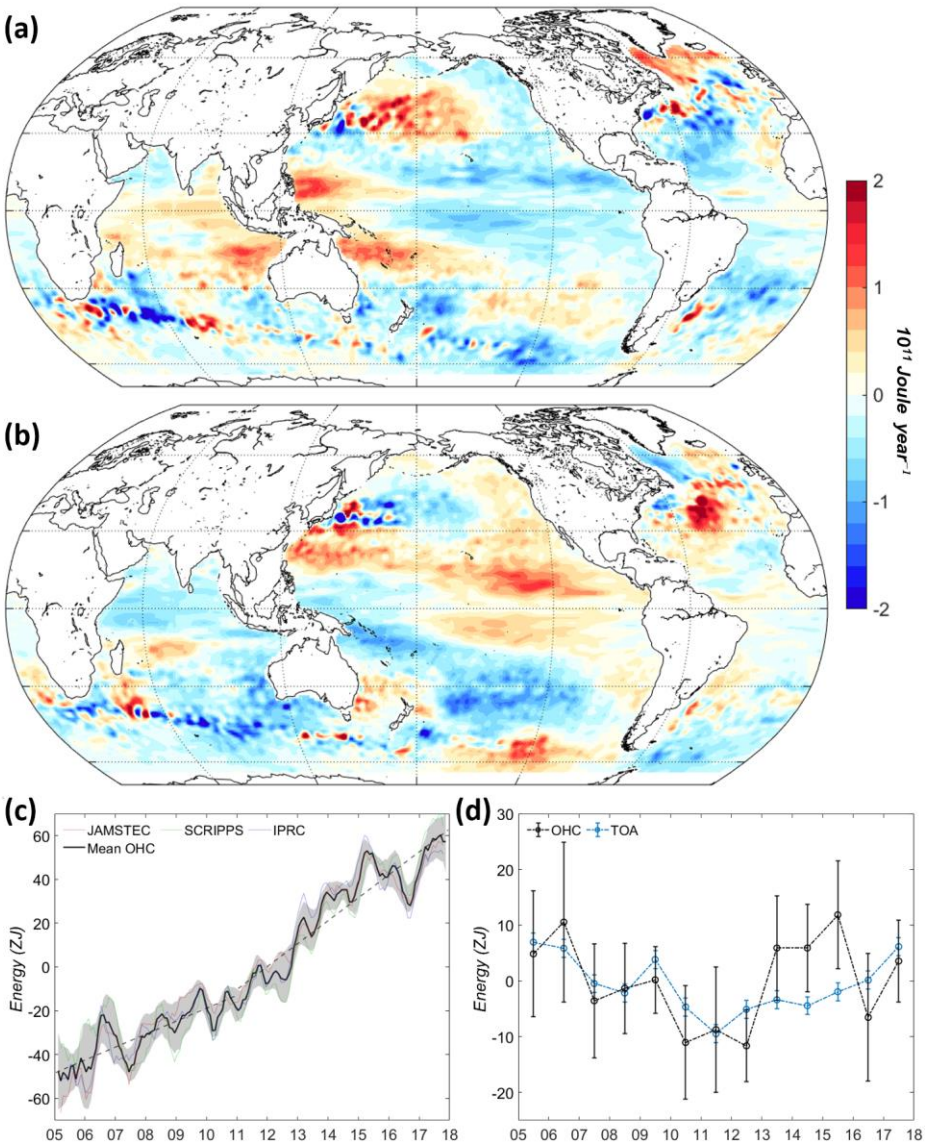

Figure 3.1.14. Global map of upper-2000 m OHC trend (joules per year) from the SCRIPPS data during (a) 2005–2010 and (b) 2011–2017. (c) Ensemble mean of globally integrated OHC (black) based on three Argo products and their individual values (colored lines). The shaded areas denote one standard deviation around the mean. (d) Comparison between the yearly OHC (black) and TOA net energy storage (blue). Each component was detrended for the study period. The OHC uncertainties (black bar) are shown at one standard error of the mean, and TOA annual random errors (blue bar) are based on Johnson et al. (2016).

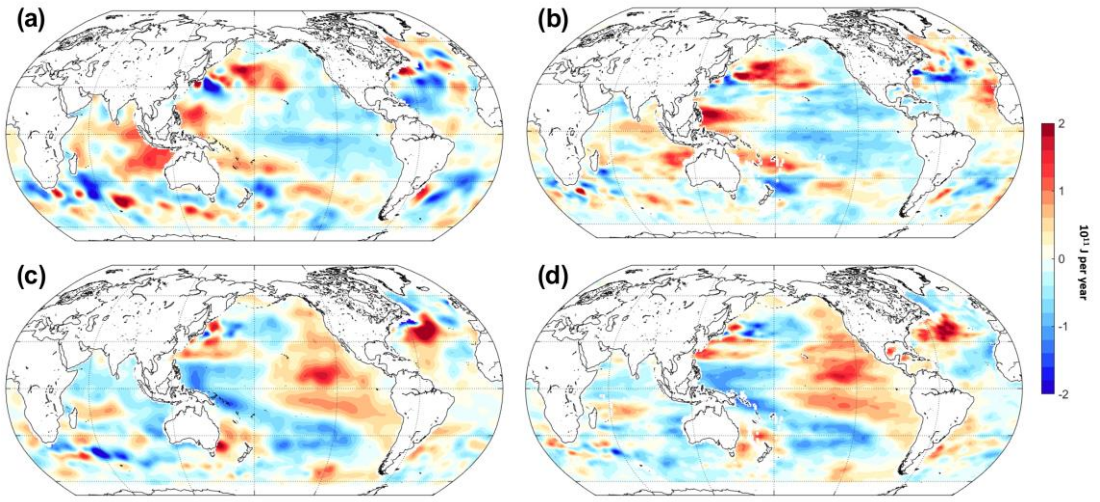

Figure 3.1.15. Argo-derived OHC trends over (a, b) 2005-2010 and (c, d) 2011-2017. Global maps of upper-2000 m OHC trends based on IPRC (a, c) and JAMSTEC (b, d).

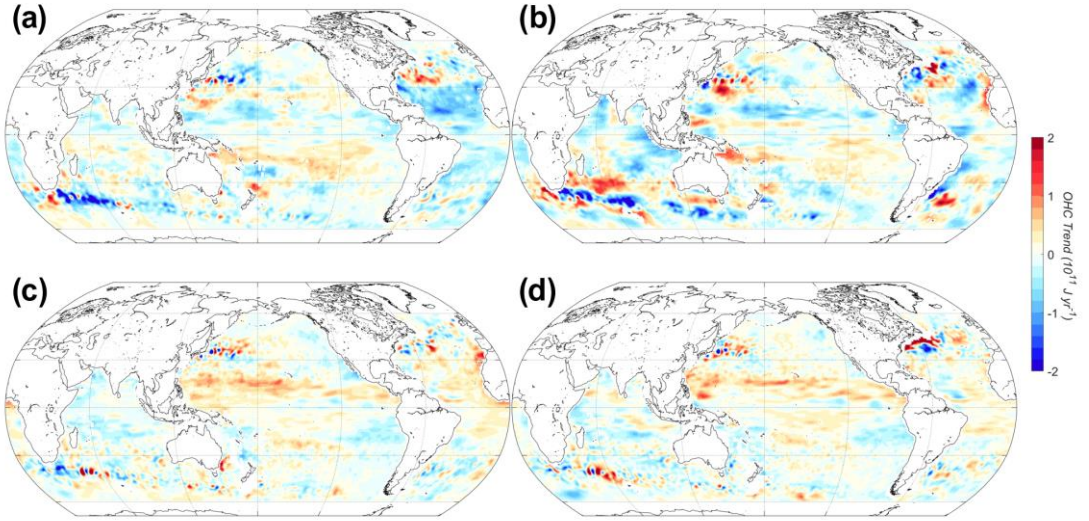

Figure 3.1.16 Spatial pattern of the trend difference between (a, c) SCRIPPS with IPRC (SCRIPPS minus IPRC) and (b, d) SIO with JAMSTEC (SCRIPPS minus JAMSTEC), over 2005-2010 (a, b) and 2011-2017 (c, d).

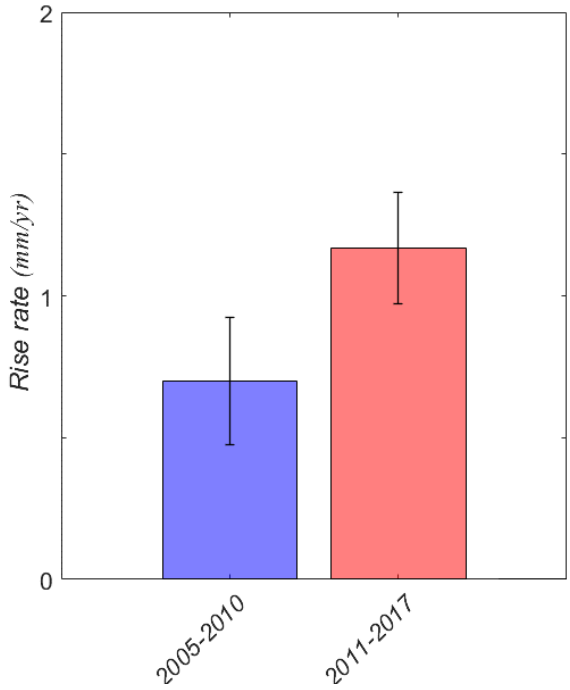

Figure 3.1.17. Steric sea level trends based on averaged three Argo products over 2005-2010 (Left) and 2011-2017 (Right). Error bars represent 95% confidence intervals estimated from slopes of uncertainty.

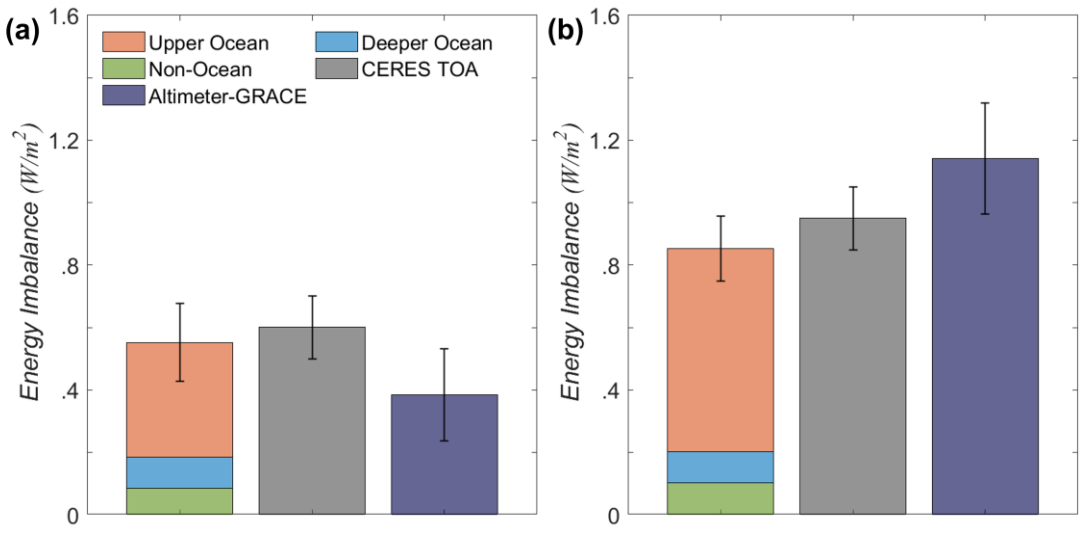

Figure 3.1.18. Three independent estimated contribution to EEI over (a) 2005–2010 and (b) 2011–2017. Left bar: in situ observational estimate of ocean heat uptake by combining Argo-based upper ocean (0–2000 m) and previously published estimates of heat uptake by the deeper ocean terms (Purkey and Johnson, 2010) and non-ocean term (von Schuckmann et al., 2020); middle: direct CERES satellite measurements of TOA net energy flux, and right: altimetry minus GRACE residual approach. Error bars represent 95% confidence intervals estimated from slopes of uncertainty fitted to each data. Uncertainties of CERES TOA flux are shown at one standard deviation (0.1 W m^{-2}) based on Johnson et al. (2016).

3.1.6. Conclusion and Discussions

Understanding the GMSL responses to natural variability can provide important information on the ocean's role in controlling the Earth climate system (Leuliette and Willis, 2011; Trenberth and Fasullo, 2010). In this study, we conducted observational analyses to examine the decade-scale fluctuation in GMSL rate and its connection to variations in ENSO, while discussing the impact of climate decadal variability on the Earth's energy budget and global hydrological cycle. The resulting relationship among sea-level rise, precipitation, ocean warming, and TOA net flux demonstrates a physically consistent expression of decadal climate variability on global scales. Based on the analysis conducted here, the following results can be highlighted: 1) a distinct decadal fluctuation in the rate of GMSL has been identified; 2) the GMSL responses to interannual ENSO signals can be modulated at times of transition in the Pacific decadal mode; 3) both the steric and LWS components account for a large fraction of the decadal fluctuation in the GMSL rate; and 4) the change in ocean heat uptake before and after 2011 is consistent with TOA net energy flux within observation uncertainties and linked to the Pacific decadal climate variability.

Our results can further clarify the ocean's role in EEI, global hydrology, and perspectives on ongoing sea-level change. An ongoing GMSL rise can be influenced by climate-driven signals that can accelerate or decelerate the underlying sea-level trend for decadal time periods. Furthermore, the estimate conducted here illustrates the utility of completely independent datasets for the cross validation of EEI by emphasizing the consistency of thermal energy in the Earth system (Loeb et al., 2021). Although systematic errors of space observations and in situ uncertainties still remain large owing to unsampled regions and/or mapping choice, efforts to extend both satellite measurements and Argo records with ongoing development of Deep Argo floats (Johnson et al., 2015) will allow better monitoring of EEI changes and give

accurate datasets to estimate the role of ocean in the Earth's energy and GMSL rise in the future (Llovel and Terray, 2016).

3.2. A decadal shift toward and El Niño-like ocean state in the tropical Pacific and the recent resumption of ocean warming

3.2.1. Introduction

Since the beginning of the 21th century, there has been tremendous public and scientific interest in a pause in global mean surface temperature (GMST) warming known as the recent "hiatus" (Kosaka and Xie, 2013; England et al., 2014; Lee et al., 2015; Maher et al., 2018). Various mechanisms have been proposed for this hiatus; however, most studies support the possible importance of internal climate variability, including the Interdecadal Pacific Oscillation (IPO, Power et al., 1999) or the Pacific Decadal Oscillation (PDO, Mantua et al, 1997), in modulating global warming. Recent analyses of observations and climate models revealed that the recent hiatus period was closely linked to the negative phase of the IPO, which manifests as a low-frequency La Niña-like pattern, with enhanced trade winds, warming of the western Pacific subsurface, strengthening of the Equatorial Undercurrent (EUC), and cooling of the eastern Pacific surface (Meehl et al., 2011, 2013; Maher et al., 2014, 2018; Nieves et al., 2015; England et al., 2014).

In contrast to the hiatus period, since approximately 2011, the tropical Pacific has experienced a remarkable shift, including a strong La Niña in 2011/2012 followed by a strong El Niño in 2015/2016 (McPhaden, 2015). The sea surface temperature (SST) in the central-to-eastern tropical Pacific (CETP) has risen persistently, shifting more toward an El Niño-like state over the last few years (Levine and McPhaden, 2016). Interestingly, the recent warming in the tropical Pacific coincides fairly well with the new increasing trend in the GMST after the end of the early-2000s hiatus (NASA news, 2017). Hu and Fedorov (2017) emphasized the role of the extreme 2015/2016 El Niño as a dominant factor contributing to the ending of the

recent warming hiatus. At the same time, a dramatic shift in the Pacific sea level has also occurred, compared to earlier decades. Using a cyclostationary empirical orthogonal function (CSEOF), Hamlington et al. (2016) extracted the dominant modes of the sea level variability and suggested an ongoing shift in the phase of the low-frequency climate signal in the Pacific Ocean.

Recently, Meehl et al. (2016) predicted a transition in the IPO from negative to positive, with a resumption of global warming, in a decadal prediction for the period of 2015–2019 that was initialized in 2013. Indeed, the PDO (highly correlated with the IPO) has been shifting toward a positive peak since approximately 2011 (Maher et al., 2018). With the PDO transitioning back to positive, previous studies suggest that an El Niño-like state should exist, with a weakening of the trade winds and associated changes in the ocean circulations. To examine the recent shift compared with the earlier decades, we first use an ensemble empirical mode decomposition (EEMD) method to adaptively decompose the non-stationary ocean/climate signal into a set of intrinsic mode functions (IMFs) (Wu and Huang, 2009). Then, we investigate the recent shift in the Pacific Ocean toward an El Niño-like state, particularly with respect to climate-altered trade winds and associated ocean circulations in the tropical Pacific, and discuss its connection to the recent resumption of global warming. An ocean circulation model is also used to identify the dynamical responses of the ocean circulations to large-scale trade wind changes, which are purely related to the variability of the Pacific climate.

3.2.2. Data and Methods

3.2.2.1 Observational Data sets

We used altimetry-based monthly sea level data for the period of 1993–2017 processed by the Commonwealth Scientific and industrial Research Organization (CSIRO; http://www.cmar.csiro.au/sealevel/sl_data_cmar.html). In addition, we used two in-situ-based temperature and salinity data sets from the Met Office Hadley Centre (EN4; http://www.metoffice.gov.uk/hadobs/en4/download-en4-2-0.html, Good et al., 2013) and the Japan Agency for Marine–Earth Science and Technology (JAMSTEC; http://www.jamstec.go.jp/ARGO/argo_web/argo/?page_id=83&lang=en, Hosoda et al., 2008), both of which provide 1°×1° spatial resolution and standard level monthly data during the period of 1993–2017 for EN4 and the period of 2001–2017 for JAMSTEC. These datasets allow us to calculate changes in the steric sea level (SSL) and ocean heat content (OHC) from the surface to a depth of 2000 m (equation in section 3.1.5). Three different surface wind products were used; the 2.5° National Centers for Environmental Prediction/National Center for Atmospheric Research Reanalysis product (NCEP/NCAR; https://www.esrl.noaa.gov/psd/data/gridded/data.ncep.reanalysis.html, Kalnay et al., 1996), the 1° European Center for Medium-Range Weather Forecasts ERA-Interim product (ECMWF; https://www.ecmwf.int/en/forecasts/datasets/archive-datasets/reanalysis-datasets/era-interim, Dee et al., 2011) and the 1/4° Cross-Calibrated Multi-Platform surface vector winds product (CCMP; http://www.remss.com/measurements/ccmp, Wentz et al., 2015). We defined the Pacific trade wind by averaging the u-component of the wind between 140° E and 200° E and between 10° S and 10° N. The two climate indices, PDO and IPO were downloaded from public sites (PDO; http://research.jisao.washington.edu/pdo, IPO; http://www.esrl.noaa.gov/psd/data/timeseries/IPOTPI/).

3.2.2.2. EEMD Analysis

The main analysis method used in this study is the EEMD method, which is based on an empirical mode decomposition (EMD) designed to separate the dataset into a finite number of IMFs and a residual representing the long-term adaptive trend (Huang et al., 1998). In EEMD, the final IMF is obtained as an ensemble average of the corresponding IMFs that were decomposed from the time series with the addition of Gaussian white noise by the EMD (Huang and Wu, 2008). This advanced EEMD method significantly improves the mode mixing problem in the original EMD (Wu and Huang, 2009). The benefit of using EEMD is that it allows for the separation of non-stationary oscillations, such as natural variability on different time scales, into the intrinsic modes; therefore, we used EEMD to capture the temporal evolution of the ocean and/or climate mode in the tropical Pacific (e.g. Franzke, 2010, 2012; Ji et al., 2014; Kidwell et al., 2014). The EEMD results were tested using the method suggested by Wu and Huang (2004) to determine the significance of each IMF (more details in section 2.3).

3.2.2.3. Ocean Circulation Model

The ocean circulation model used here is the Regional Ocean Modeling System (ROMS) (Haidvogel et al., 2000; Shchepetkin and McWilliams, 2005). The model was configured globally with a 1° spatial resolution with 30 layers in the stretched terrain-following vertical coordinate (Song and Haidvogel,1994; Haidvogel et al., 2008). The grid contains both polar regions, with the northern pole shifted toward the Russian continent. The model was initialized using the climatological World Ocean Atlas (Levitus et al., 2009) and was spun up for 60 years from its initial state using the NCEP/NCAR monthly climatology. A nonlocal, K-profile parameterization developed by Large, McWilliams, and Doney (Large et al., 1994) was used for the vertical mixing scheme. The surface fluxes of the heat and momentum are calculated

in ROMS using the bulk formulation (Fairall et al., 1996). After spin-up, the model was integrated using the daily NCEP/NCAR reanalysis forcing from 1948 to the present day; this simulation is referred to as the "hindcast" simulation. Monthly averaged results from 1993 to 2017 are used for comparisons with the observational datasets. As will be discussed later (section 3.2.5), an additional experiment was computed with the PDO-related decadal surface wind pattern during the period of 1993–2017.

3.2.3. The recent swing toward an El Niño-like state

Since approximately 2011, the sea level rise (SLR) trends have been sharply shifting toward an opposite pattern that of the previous decade (Figure 3.2.1). Two dominant features of the SLR trend are apparent in the Pacific during the period of 2011–2017: one is a strong east–west dipole pattern in the tropical Pacific, with negative trends in the west and positive trends in the east, and the other is a horseshoe shape, indicative of the PDO in the North Pacific (Hamlington et al., 2016). For the western tropical Pacific (WTP), there has been a decreasing sea level trend (approximately -24.2 mm/yr) since approximately 2011, including the ENSO-related interannual and longer-term variations; conversely, the CETP has been completely out-of-phase with the sea level in the WTP (Figures 3.2.1c and e). These features of the sea level shift were also found in the SSL using a range of subsurface measurements from the temperature and salinity datasets (i.e., EN4 and JAMSTEC), indicating the importance of steric expansion in tropical regions. The hindcast simulation reproduced the large-scale patterns of the observed SLR (Figure 3.2.1b), as well as the temporal changes in these patterns associated with the ENSO and the estimated recent trend in the SLR.

To identify whether the recent shift in the SLR is a short-term change associated with the ENSO or longer-term change in the sea levels, we conducted an EEMD analysis of the time

series in the two regions for all data sets including the hindcast result, which yielded seven IMFs and a residual in ascending order based on their timescales (Figure 3.2.2). With the exception of IMF 7, the resulting IMFs are significant compared to white noise for all data records (Figure 3.2.3). As determined via a spectral analysis, IMF 4-6 indicates a high energy (Figure 3.2.4). The first two IMFs display high-frequency components of less than a year, while IMFs 3–5 cover the ENSO-scale frequencies, varying from 1.5 yr to 7 yr. Importantly for this study, these ENSO signals were clearly separated from a the IMF 6 low-frequency mode and the secular trend. For all records, IMF 6 has a peak period of ~12.4 yr, showing trend shifts in the mid-1990s, early-2000s, and early 2010s (Figures 3.2.1d and f). To test whether this decadal mode was affected by the end-point of the time period including the significant 2015/2016 El Niño event, similar to Kidwell et al. (2014), we compared the decadal mode of the full record length with incrementally shortened records of the same data by removing 1–36 months of data from the end of the time series (Figure 3.2.5). Even though the amplitudes of the decadal mode were slightly changed, their variability persisted regardless of the impact of the 2015/2016 El Niño event. In addition, previous studies have demonstrated the robustness of decadal mode, which is distinct from the interannual mode, using EOF and cyclo-stationary EOFs (Zhang and Church, 2012; Hamlington et al., 2016). Decadal modes in these studies show the high consistency with IMF 6. These results indicate that the decadal mode is robust in the tropical Pacific.

The vertical profile of the observed temperature exhibited significant trends, with warming in the upper CETP and cooling in the thermocline of the WTP (Figure 3.2.6a). A maximum cooling in excess of 0.6°C occurred in the thermocline between 100 m and 300 m, extending to the central Pacific. Conversely, there was a strong warming trend in the CETP thermocline that extended to the surface over nearly the entire tropical Pacific. The simulated trends are similar to those found in the observations (Figure 3.2.6b); however, the simulated tropical

thermocline is a little shallower than that indicated by observational evidence. This discrepancy may be due to difficulties in the model with handling the vertical mixing processes (Moum et al., 2013; Maher et al., 2018). The temperature trends of all the datasets demonstrate a weakening of heat convergence in the WTP thermocline and a warming of the upper CETP, as opposed to the La Niña-like trends identified during the recent hiatus period (England et al., 2014; Nieves et al., 2015). The recent trend is clearly evident in the two in-situ-based OHC (upper-2000-m) records, which also agree with the hindcast result (Figures 3.2.6c and 3.2.6e). Note that the temperature above 300 m contributed to nearly 85% of the recent trends in the upper-2000-m OHC in the tropical Pacific (not shown). As expected, the EEMD-determined IMF 6 of the OHC corresponds to the decadal modes of the sea level and SSL in the tropical Pacific. Taking the IMF 6 as a proxy of the evolution of the tropical Pacific, it is reasonable to believe that, over the last few years the tropical Pacific has shifted toward an El Niño-like ocean state, with a weakening of heat convergence in the equatorial thermocline and an enhanced SST in the CETP.

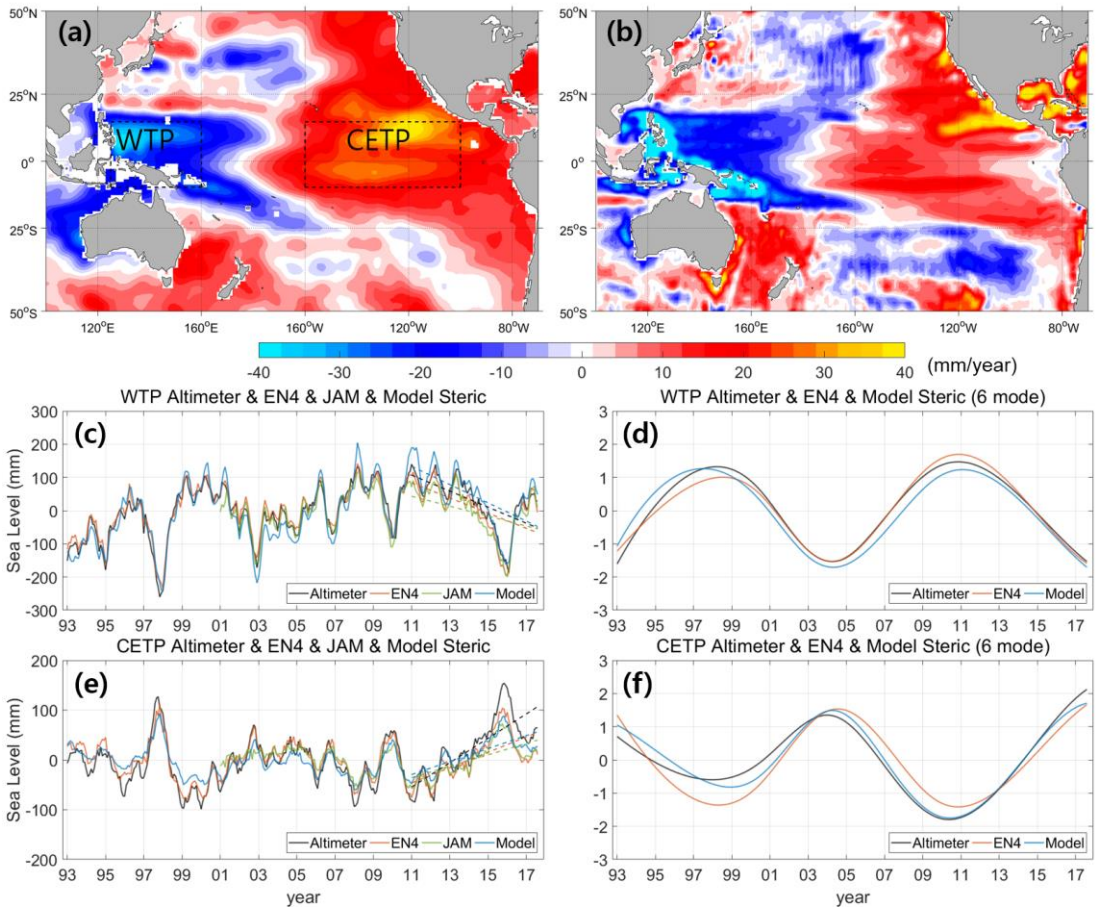

Figure 3.2.1 Trends in (a) the satellite-based sea level and (b) the modeled steric sea level (SSL) for the period of 2011–2017. Time series of the monthly SSLs of EN4, JAMSTEC, the hindcast result, and the satellite-based sea level for (c) the WTP and (e) the CETP. The dashed lines indicate the linear trends during the period of 2011–2017. Decadal modes derived from the EEMD decompositions of the satellite-based sea level, EN4 SSL, and the model SSL time series in (d) the WTP and (f) the CETP.

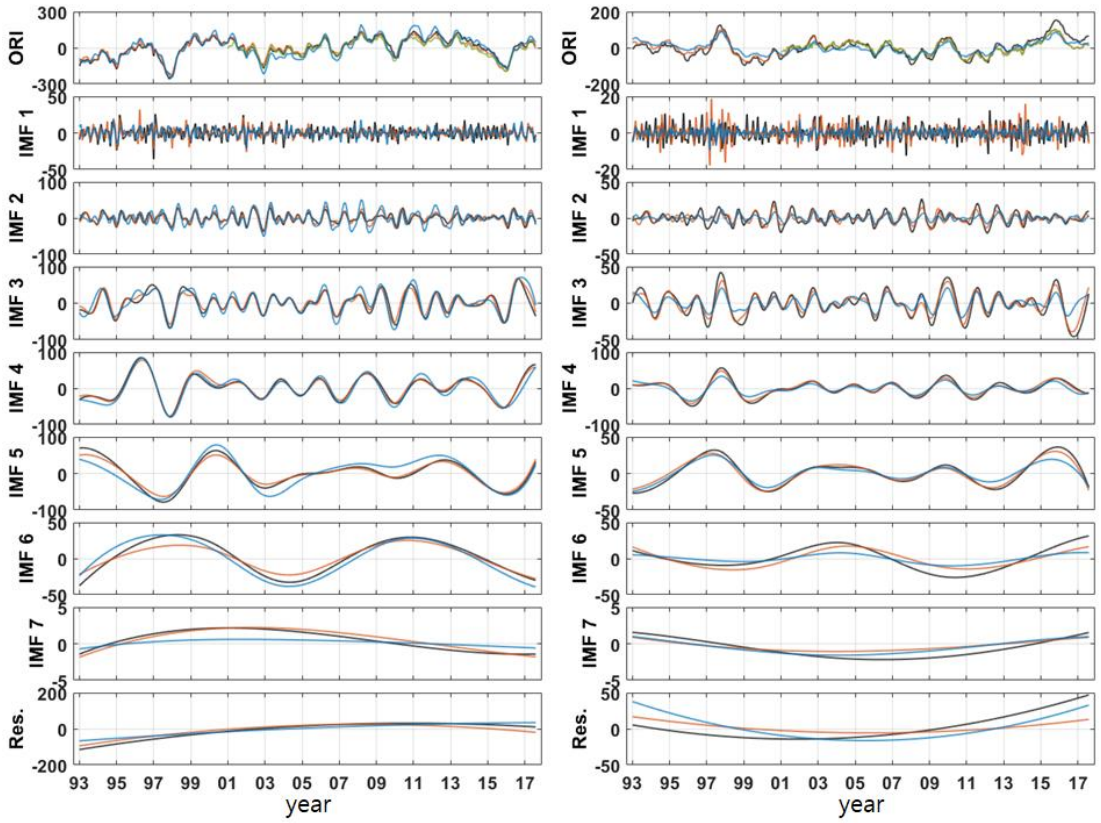

Figure 3.2.2. EEMD decompositions of time series in the WTP (left) and CETP (right panels) for the altimetry-based sea levels (black), EN4 SSL(orange), and model SSL (blue). All of the original monthly data (top) are decomposed into seven IMFs and the resulting trends (bottom panels) by EEMD method.

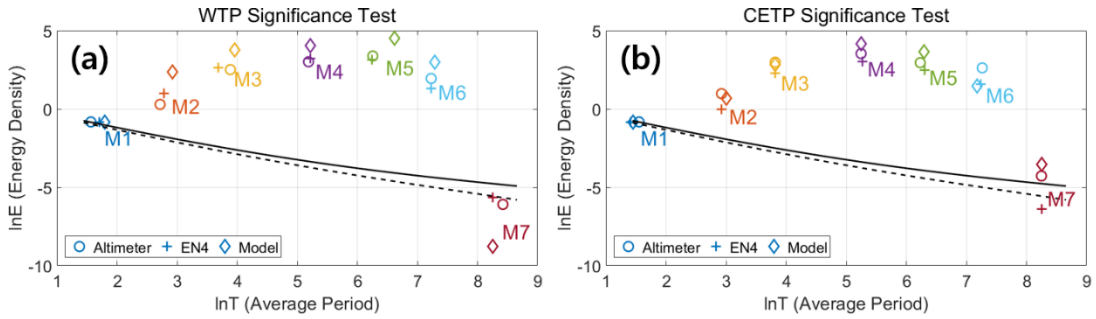

Figure 3.2.3. Statistical significance tests of the seven IMFs of the monthly altimetry-based sea level, EN4 SSL, and model SSL in the (a) WTP and (b) CETP. The dashed lines represent the 95% confidence level and the solid lines are the 99% confidence level. With the exception of IMF7, all IMFs are distinguishable from Gaussian white noise at both confidence levels.

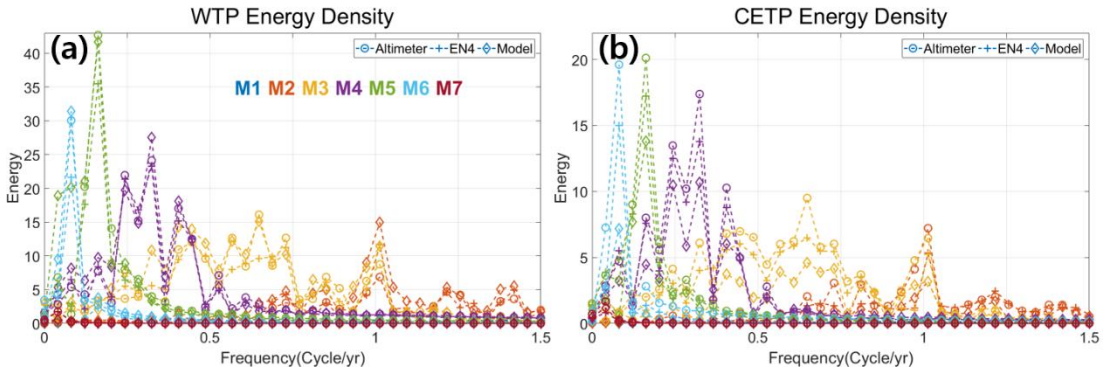

Figure 3.2.4. Spectral energy density of each IMF mode for the monthly altimetry-based sea level, EN4 SSL, and model SSL in the (a) WTP and (b) CETP.

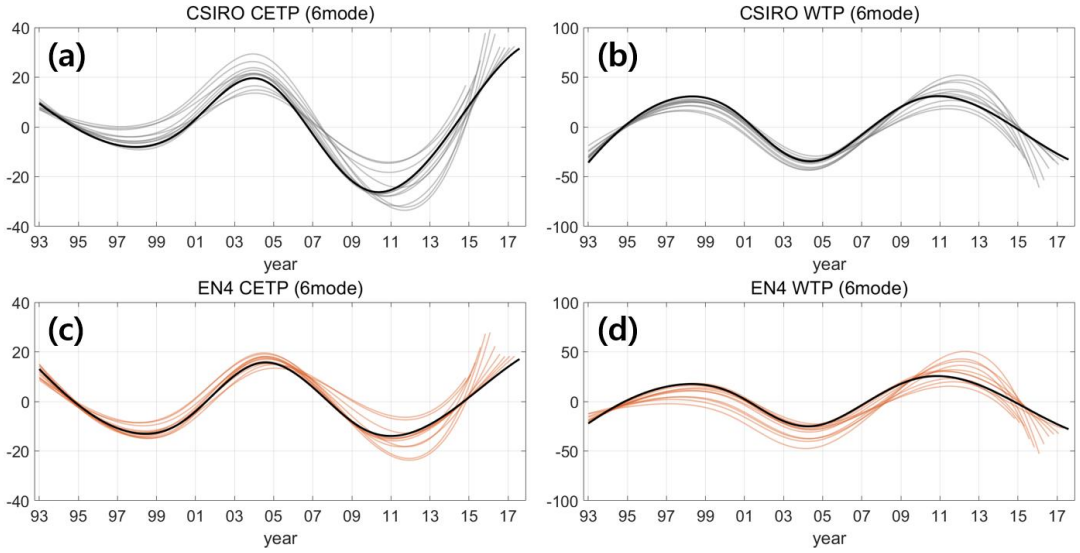

Figure 3.2.5. Decadal modes (IMF 6) of the full record length (black) and incrementally shortened records (grey lines) of the same sea level and SSL data in the WTP (left) and CETP (right panels) by removing 1–3 years of data from the end of the time series.

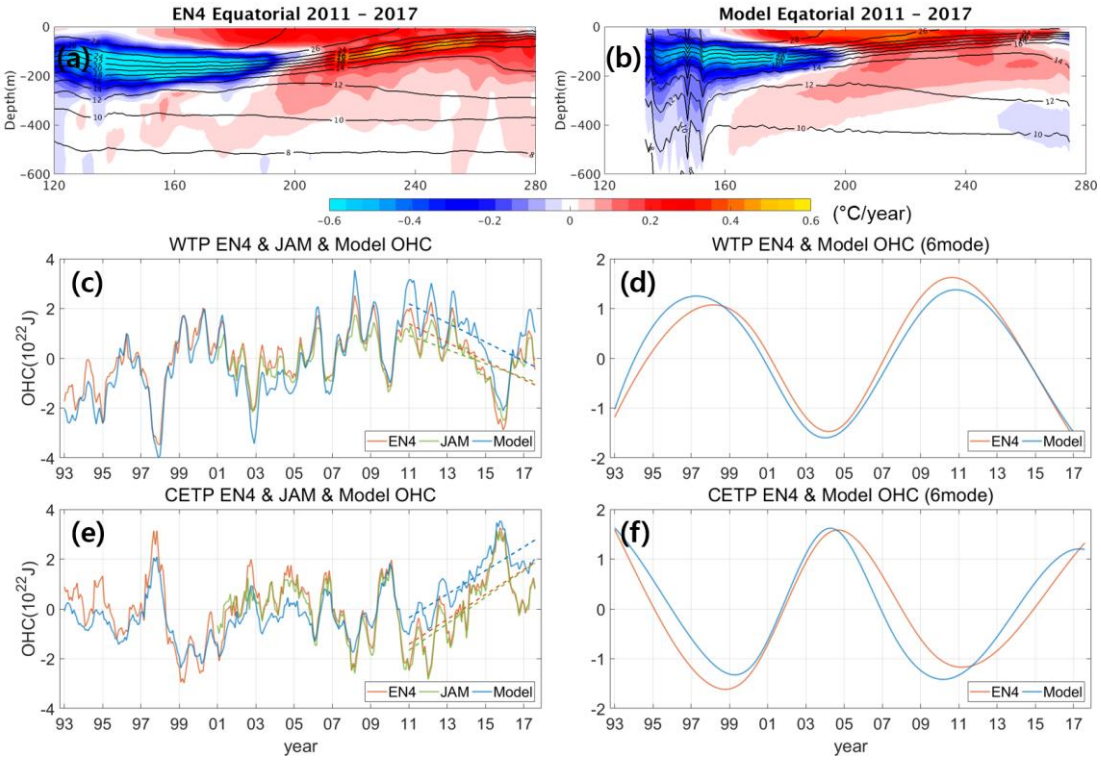

Figure 3.2.6. Trends in the meridionally averaged temperature between 5°S and 5°N the period of 2011–2017 from (a) EN4 and (b) the hindcast result. The mean temperature contours are overlaid. Time series of the monthly OHCs calculated from EN4, JAMSTEC, and the hindcast result for (c) the WTP and (e) the CETP. The dashed lines indicate the linear trends during the period of 2011–2017. Decadal modes derived from EEMD decompositions of the EN4 SSL and model SSL time series in (d) the WTP and (f) the CETP.

3.2.4. The recent resumption of global ocean warming and Pacific decadal variability

Following the discussions provided by Kosaka and Xie (2013) and England et al. (2014), the La Niña-like cooling in the CETP is likely a key component of the global warming hiatus that had been identified since the early 2000s, reflecting a connection between the Pacific climate variability and global warming. These authors predicted a resumption of global warming if the tropical Pacific shifts to an El Niño-like state in line with the Pacific decadal variability in the coming decades. Both the observations and the model revealed an acceleration in global ocean warming since approximately 2011 when an El Niño-like state began to prevail in the tropical Pacific (Figure 3.2.7a). Note that the global upper-100-m OHC is highly correlated with both the global SAT and the SST (Figure 3.2.8, 0.78 and 0.89 for SAT and SST, respectively, with statistically significance being above 95%). The CETP Ocean contributed nearly ~29% of the observed global OHC trend during the period of 2011–2017. The EEMD-determined decadal modes (i.e., IMF 6) in both the global oceans and the CETP Oceans are in phase with a downward shift in the early 2000s and following an upward shift around 2011 (Figure 3.2.7b). This decadal mode in the tropical Pacific may be contributing to the enhanced global ocean warming over the last few years, as well as the suppressed global ocean warming during the early 2000s hiatus, which is consistent with the studies described above. With the exception of their amplitudes and trend rates, the hindcast simulation successfully captured the recent acceleration of the warming trends both in the CETP and in the global oceans, including their decadal mode. The model-data analysis using EEMD demonstrates that the recent resumption of global warming is associated with the decadal warming of the tropical Pacific over the last few years, as opposed to the behavior seen in earlier La Niña-like decades.

The decadal shift in the tropical Pacific is tightly linked to climate-related trade winds,

which are an important contributor to regional heat and mass redistributions (Timmermann et al., 2010; Merrifield et al., 2012; Moon et al., 2013). For all wind products, the Pacific trade winds increased substantially from the early 2000s to 2011, while a decreased trend in the easterly wind can be seen over the most recent decade (Figure 3.2.7c). This altered trade wind pattern resulted in changes in the upper-ocean circulations in the tropical Pacific, redistributing heat and mass via Ekman dynamics. For example, the recent weakening of the trade winds can account for the weakening of the heat convergence in the equatorial thermocline, which in turn caused a cooling of the thermocline in the WTP. At the same time, the equatorial upwelling in the tropical Pacific was suppressed, which resulted in enhanced SST warming in the CETP that could drive further warming in other regions. The EEMD results show that the transition times of the decadal mode (IMF 6) agree well between the time series of the trade wind and the Pacific climate indices, i.e., PDO and IPO (Figures 3.2.7e and f). In particular, both time series show a clear transition around 2011, agreeing with the period of strong tropical warming in the Pacific being an El Niño-like ocean state and the concurrent resumption of global ocean warming. It is evident from the regression patterns for the decadal mode derived from the EEMD decomposition of the PDO (Figure 3.2.9) that there are dynamic oceanic responses to climate-related decadal surface wind patterns, consistent with the linear trend maps of the sea level (Figure 3.2.1a).

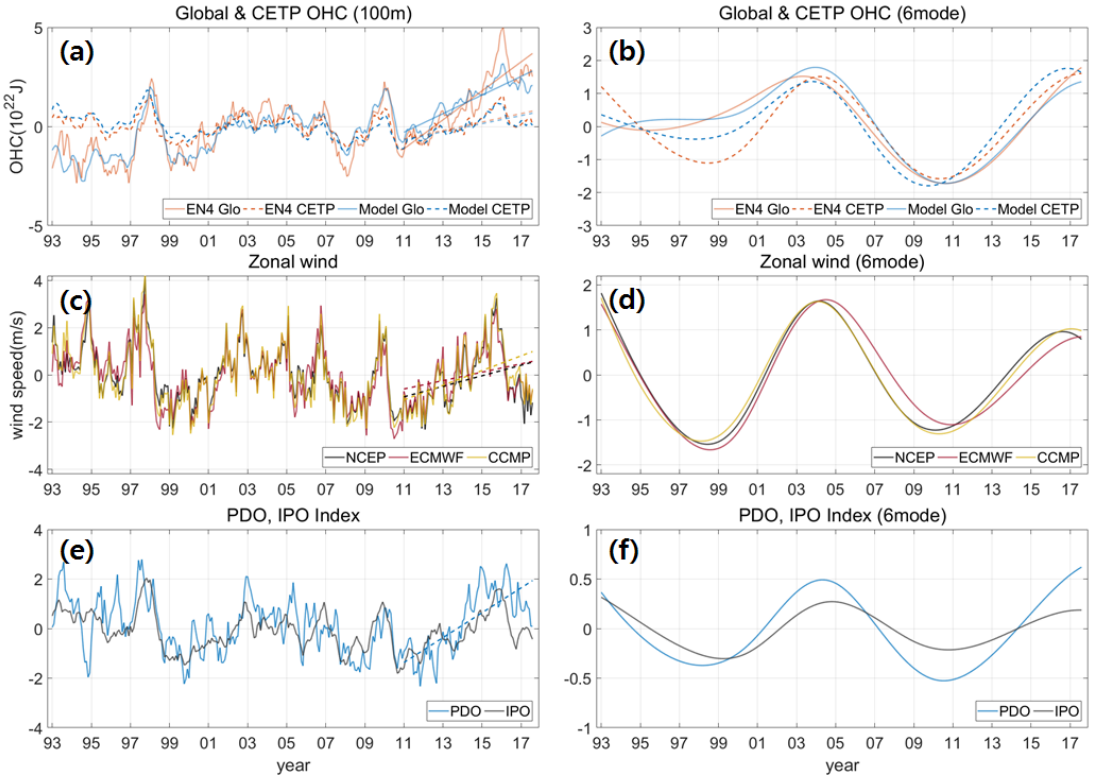

Figure 3.2.7. (a) Comparison of the upper-100 m ocean heat content (OHC) between the global oceans and the CETP Ocean from EN4 and the hindcast result and (b) their normalized decadal modes derived from the EEMD decompositions. (c) Time series of the zonal mean wind in the tropical Pacific (140°E–160°W, 10°S–10°N) from the NCEP, ECMWF, and CCMP products, and (d) their decadal modes derived from the EEMD decompositions. (e) Time series of PDO and IPO and (f) their decadal modes derived from the EEMD decompositions. The dashed lines indicate the linear trends during the period of 2011–2017.

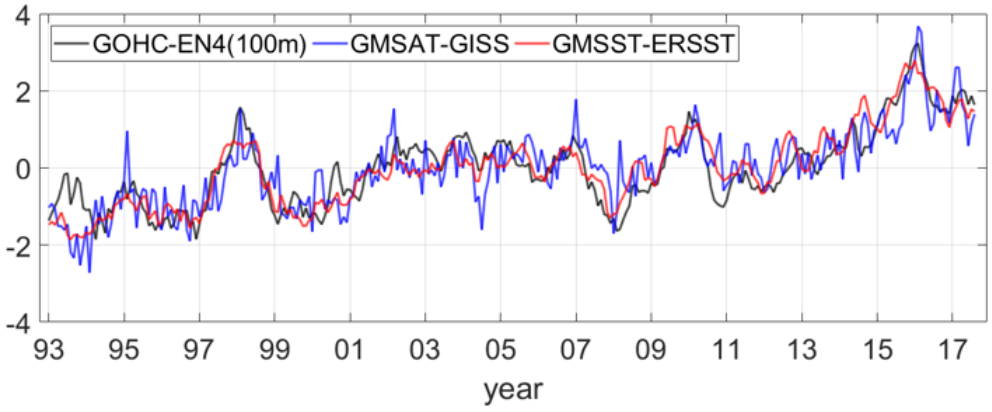

Figure 3.2.8. Time series of upper-100 m global ocean heat content (OHC) from EN4 (black), global mean surface air temperature (SAT) [Huang et al., 2015,2016; Liu et al., 2015] from GISS (blue) [Hansen et al., 2010; GISS Surface Temperature Analysis Team, 2018], and global mean SST from ERSST (red) during the period of 1993–2017. All data values were normalized by their respective standard deviation.

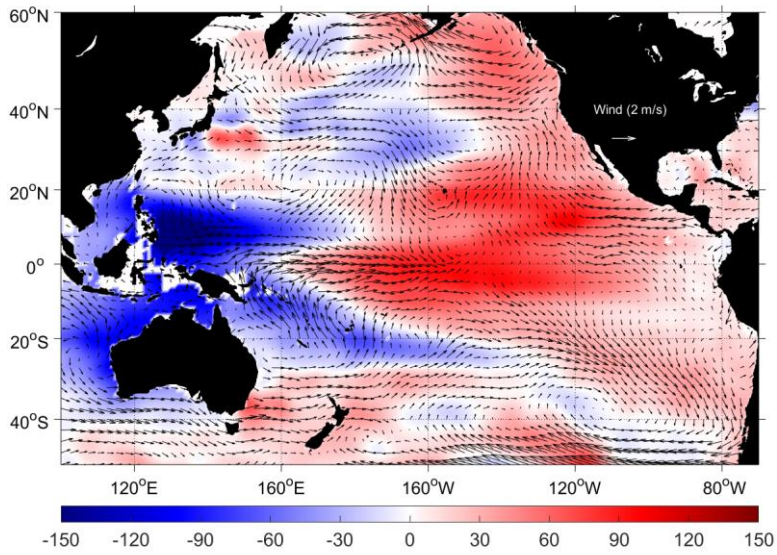

Figure 3.2.9. NCEP wind (vector) and altimetry-based sea level (color) regressed on the decadal mode (IMF 6), which was extracted from the EEMD of the PDO time series from 1993 to 2017.

3.2.5. Response of the tropical Pacific Ocean to clim`ate-related trade winds

To highlight how the ocean responds to climate-related decadal wind patterns, we conducted an additional experiment with the surface wind forcing regressed on the decadal mode, which was extracted from the EEMD of the PDO time series from 1993 to 2017 (Figure 3.2.9). Other conditions including the surface heat fluxes were unchanged relative to the hindcast simulation. Without the long-term wind trend and the high-frequency modes, the resulting SSL trend pattern exhibits a low-frequency La Niña-like pattern during the 2003–2010 period when the PDO transitioned to negative, while an El Niño-like pattern occurs during the period since 2011 when the PDO transitioned from a negative state back to a positive state (Figures 3.2.10a and b). In particular, the recent trend shifts in the Pacific SSL, as seen in the observations, were reproduced in the experiment even though the magnitude of the trend pattern was smaller than that of the observed trends. The modeled SSL no longer has strong interannual ENSO signals but reproduces distinct decadal fluctuations corresponding to the times of the PDO transitions (Figure 3.2.11). The PDO-related decadal mode contributed nearly 40% and 75% of the recent SSL trends in the WTP and CETP, respectively, according to the hindcast result. Note that, because the surface heat flux continues to increase in this additional experiment, there still exists an upward SSL trend over the period of 1993–2017. The superposition of the decadal and long-term trends may result in a larger contribution of the decadal mode to the recent upward trend in the CETP.

The decadal fluctuations of SSL in the tropical Pacific are reflected in the temperature trends along the equator (Figures 3.2.10c and d). There was warming in the tropical Pacific and cooling in the western thermocline between 100 m and 300 m during the 2011–2017 period with the weakening of the PDO-related decadal trade winds. These trends are very similar to those found in both the observations and the hindcast simulation; however, these trends are

slightly underestimated. Conversely, the temperature trends during the 2003–2010 period are well matched by a recent opposing trend due to the reversed trend of the wind patterns on a decadal time scale. These decadal temperature variations are also consistent with changes in the strength of the EUC that, in general, bring cooler subsurface water from the western to the eastern tropical Pacific in the upper layer (Maher et al., 2018). During the 2003–2010 period, the strengthened trade winds induced the SSL rise in the WTP due to convergences of the heat and mass, which generate a strengthening of the EUC and the equatorial upwelling (Figure 3.2.10e). The circulation changes resulted in warming of the WTP subsurface and cooling of the upper CETP, which may drive cooling in other regions due to interactions with the atmosphere (England et al., 2014). Conversely, the oceanic responses have been reversed since 2011 when the trade winds adopted a decreasing trend accompanied by weakening of the EUC and warming of the upper CETP (Figure 3.2.10f). This confirms that the decadal changes in wind forcing associated with Pacific climate variability have played an important role in driving the dynamic upper-ocean circulations, at least over the two most recent decades, and modifying the SSL trends, subsurface temperature changes, and the strength of the EUC in the tropical Pacific.

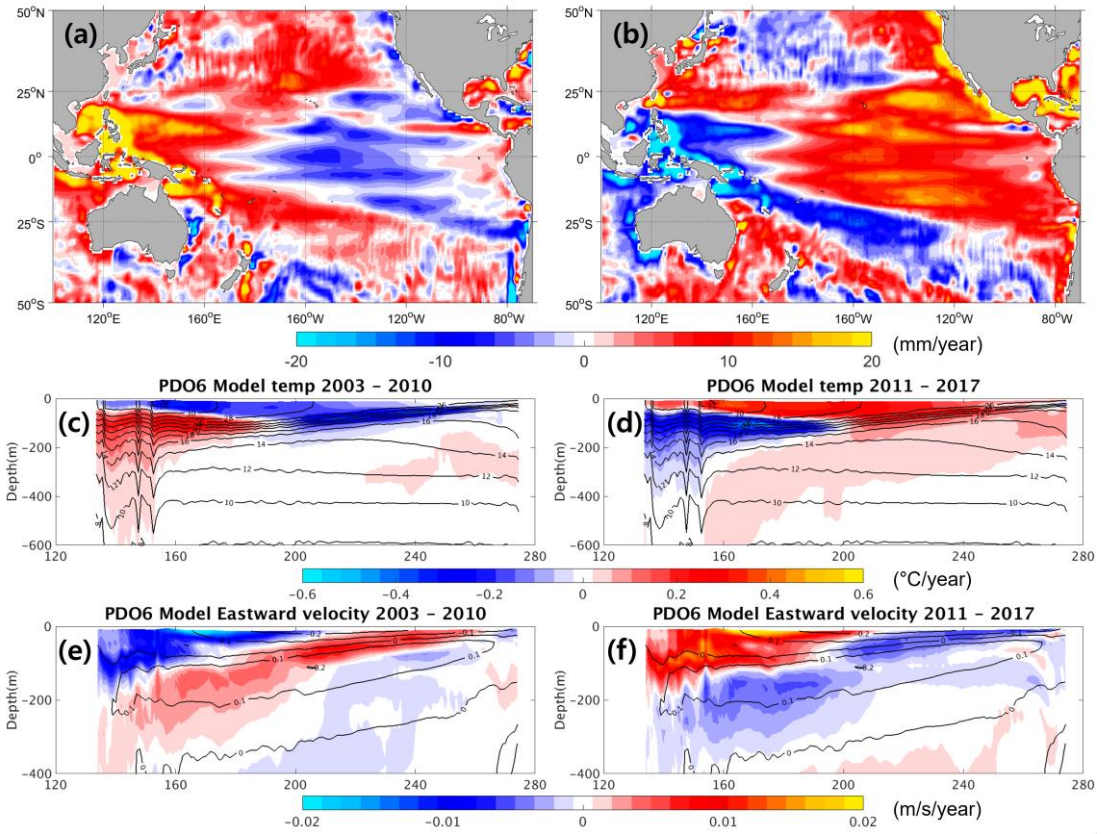

Figure 3.2.10. Trends in (a, b) SSL (mm/yr), (c, d) temperature (°C/yr), and (e, f) eastward velocity (m/s/yr) derived from the model experiment with decadal wind forcing during the periods of 2003–2010 and 2011–2017, respectively. The temperature and eastward velocity fields were meridionally averaged between 5°S and 5°N. The mean temperature and eastward velocity contours are also overlaid.

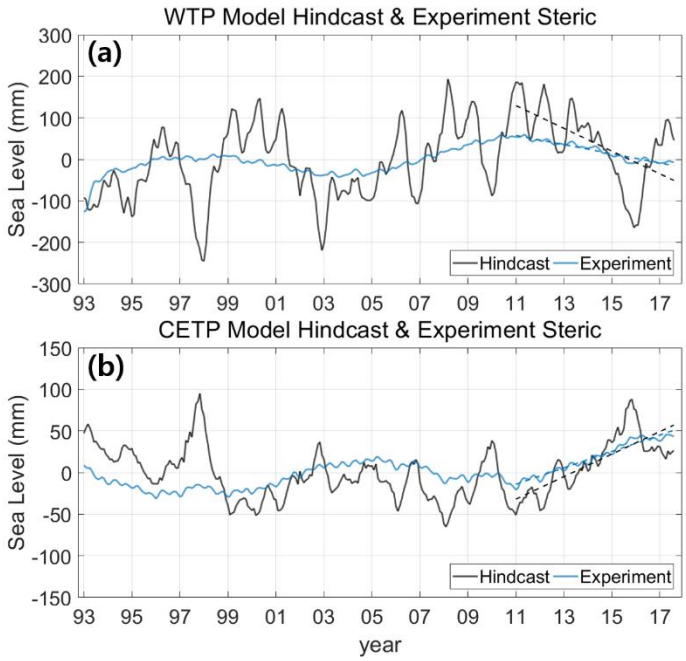

Figure 3.2.11. Comparison of SSL between the hindcast (black) and model experiment with decadal wind forcing (blue) for the (a) WTP and (b) CETP, respectively. The dashed lines indicate the linear trends during the period of 2011–2017.

3.2.6. Conclusion

Since approximately 2011, a dramatic shift toward an El Niño-like state in the tropical Pacific Ocean has been detected in both satellite altimeters record and in situ-based upper-ocean measurements. The sea level in the CETP increased substantially, including the SSL component, as reflected by a strong warming trend in the CETP thermocline that extends to the surface layer. Conversely, a sea level drop and subsurface cooling occurred in the WTP, compared the previous decade. A hindcast simulation was able to reproduce the spatial patterns of the observed SSL and OHC trends, as well as their temporal variations, over the period of 1993–2017. Using an EEMD analysis, we identified a distinct decadal mode in the tropical Pacific, which corresponds to the recent shift in the sea level and SSL. The decadal fluctuation also showed a clear connection with the decadal period of global ocean warming, likely contributing to the resumption of global warming during the last few years as well as the suppression of the warming during the early 2000s hiatus. The decadal mode in the tropical Pacific is associated with the PDO-related trade wind trends on a decadal time scale; this can control the SSL trends, subsurface temperature changes, and the strength of the EUC in the tropical Pacific. This oceanic response was demonstrated by comparing the model results to only the decadal oscillating wind pattern, which indicates the important role played by the upper-ocean circulation associated with the Pacific climate variability in redistributing heat in the tropical Pacific Ocean. These results suggest that climate-forced regional variability can have a significant global impact on low-frequency modes. Several studies have reported on the relationship between the global and regional oceans with respect to ENSO, but we here emphasize that other natural climate variability like the PDO and the IPO have a possible link to global ocean warming. Compared to statistical descriptions provided in recent studies, the model-data analysis using EEMD may provide more convincing support to the dynamical descriptions, as well as a reliable methodology for extracting climate-forced signals and

exploring its connection to global warming.

This study has implications for decadal predictions of sea level and ocean warming, which are still challenging issues. For example, if the decadal surface wind pattern fluctuates persistently, associated shifts in the Pacific climate mode would result in suppression of the eastern Pacific SLR and concurrent cooling of the eastern Pacific surface contributing to less global ocean warming, which may appear as a “hiatus” in the future (Kosaka and Xie, 2013). However, while the ocean model experiment provided considerable insights into oceanic responses to climate-related wind forcing, one limitation that remains in this study is the neglecting of the interaction between the ocean and atmosphere in the different natural climate modes. Therefore, additional studies using climate modeling are clearly needed to better understand the tropical Pacific processes that are linked to global ocean warming.

3.3. A process-based assessment of the sea-level rise in the northwestern Pacific marginal seas

3.3.1. Introduction

Recent improvements in in-situ observations and satellite measurements have enabled the monitoring of the sea-level budget on both global and regional scales (Chen et al., 2017; Dieng et al., 2017; WCRP, 2018; Royston et al., 2020; Cha et al., 2021). Assessments of the sea-level budget (i.e., comparing the observed sea-level changes with the sum of contributions) have recently been conducted, showing the closure of the global mean sea-level (GMSL) budget within data uncertainties (WCRP, 2018; Oppenheimer et al., 2019; Frederikse et al., 2020). However, because of various physical processes, such as regional ocean dynamic effects, changes in regional sea-level and their contributions to the sea-level rise (SLR) budget on regional scales still remains a challenging issue (Rietbroek et al., 2016; Royston et al., 2020; Yang et al., 2022; Camargo et al., 2023).

Regionally, the SLR deviates significantly from the global mean, with rates several times faster than the GMSL rate in some regions while being near zero in other regions (WCRP, 2018; Hamlington et al., 2019; Harvey et al., 2021). Unlike the processes of the GMSL budget, regional geocentric SLR should match the sum of three major contributors: (1) the steric effect due to density changes in the regional water column, (2) the manometric contribution due to changes in mass, sometimes referred to as the bottom pressure term (Gregory et al., 2019), and (3) the glacial isostatic adjustment (GIA) effect related to long-term solid earth response to the last deglaciation (Peltier, 2004). The manometric SLR comprises of ocean mass redistribution (OMR) changes driven by ocean circulation and gravitational, rotational, and deformational (GRD) effects due to contemporary land ice mass and terrestrial water storage changes, i.e.,

the contemporary-GRD (Gregory et al., 2019; Harvey et al., 2021; Camargo et al., 2023). The sum of the local steric sea-level (SSL) and circulation-driven OMR is sometimes referred to as sterodynamic sea-level (Gregory et al., 2019; Chen et al., 2021; Wang et al., 2021; Camargo et al., 2023). Both the sterodynamic process and contemporary-GRD are known as the driving processes behind the observed regional SLR pattern, which substantially differs from the GMSL rise (Wang et al., 2021).

The northwestern Pacific region is characterized by a distinct geographical feature, with a series of marginal seas including the Yellow and East China Seas (YECS), South China Sea (SCS), and East/Japan Sea (EJS), which separate the eastern Asian continent from the North Pacific Ocean (Figure 3.3.1). Previous studies have reported that over the past decades, SLR rates higher than the GMSL rise have been observed in these marginal seas (Feng et al., 2012; Moon et al., 2013; Guo et al., 2015; Cheng et al., 2016; Yu et al., 2019). Most of these studies have focused on sea-level fluctuations in response to climate variability, such as the El Niño-Southern Oscillation (Cheng et al., 2016), North Pacific Gyre Oscillation (Moon et al., 2013; Yu et al., 2019), and Pacific Decadal Oscillation (Cheng et al., 2016), on interannual to decadal timescales. However, relatively less attention has been paid to assessing the underlying processes contributing to SLR budgets on marginal seas, including extensive continental shelves. Regional processes superimpose on the global mean, and thus, SLR on the marginal seas is expected to be largely different from that on the deep open ocean (Landerer et al., 2007; Chen et al., 2021). Because SLR occurring over the regional scale is threatening to inundate many low-lying islands and coastlines worldwide, understanding and quantifying the underlying regional processes is of high importance for projections of future ocean conditions.

In this study, we assess the regional SLR budget on three marginal seas in the northwestern Pacific (YECS, SCS, and EJS) and examine whether the combined contributions from

individual processes can explain the observed geocentric SLR on these marginal seas. To close the sea-level budget, individual contributors to regional SLR were first analyzed and their sum was compared with the altimeter-measured sea-level since 1993. The sterodynamic sea level can be estimated by combining the in situ-based global thermosteric sea-level (GMTS) with the dynamic sea-level from ocean reanalyses (Gregory et al., 2019; Harvey et al., 2021; Wang et al., 2021). This proposed method was used here to quantify the sterodynamic contribution during the altimeter era. In addition, we considered an observation-based approach for the sterodynamic SLR that directly combines in situ-based regional SSL with circulation-driven OMR derived from the Gravity Recovery and Climate Experiment (GRACE). This process-based assessment of the sea-level budget provides a more complete understanding of the underlying processes that drive regional sea-level changes and whether these regional processes fully account for the observed SLR in the northwestern Pacific marginal seas.

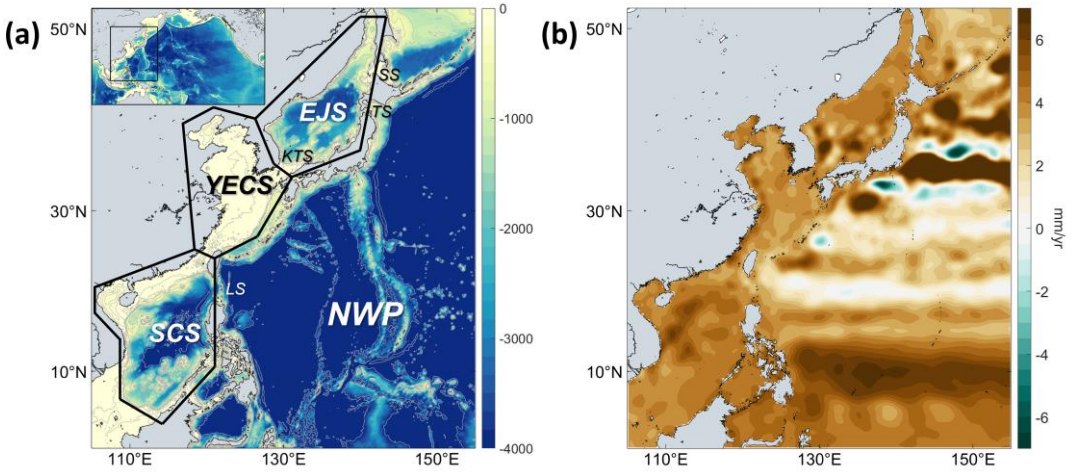

Figure 3.3.1. Geographic map of northwestern Pacific and sea-level rise trends. (a) Bathymetry of the northwestern Pacific (NWP) marginal seas including Yellow and East China Sea (YECS), South China Sea (SCS), and East/Japan Sea (EJS). Each marginal sea is defined as the area enclosed by solid lines. Abbreviation of KTS, LS, SS, and TS denotes the Korea/Tsushima Straits, Luzon Straits, Soya Straits, and Tsugaru Straits, respectively. (b) Trend of satellite-altimetry SLR in the northwestern Pacific over 1993-2017.

3.3.2. Data and Methods

Regional geocentric sea-level change can given by three main process: (1) sterodynamic sea-level (SL_{SD}), (2) changes in Gravity, Rotation, and Deformation (GRD) caused by contemporary mass redistribution from ice melting and land water storage changes (SL_{GRD}), and (3) ongoing land movement of glacial isostatic adjustment (SL_{GIA}, Peltier, 2004; Tamisiea and Mitrovica, 2011; Caron et al., 2018). Thus, the altimetry-derived geocentric regional sea-level change can be expressed by following budget equation: $SL_{ALT} = SL_{SD} + SL_{GRD} + SL_{GIA} + SL_{RES}$. The details of each process are described in section 2.2.

For the assessment of sea-level budget in the northwestern Pacific marginal seas, here we compare the regional SLR (SL_{ALT}) trends to the sum of estimates of individual contributor. The uncertainty of the sum of contribution is calculated by quadratic sum of each component ($\sqrt{\sum {\sigma_i}^2}$). σ_i is the uncertainty of each component. The 95% confidence level for the trend was calculated as follow: $b \pm t_{(1-\frac{\alpha}{2}, n-p)} * SE(b)$, where b is the trend estimate, $SE(b)$ is the standard error of the trend estimate, and $t_{(1-\frac{\alpha}{2}, n-p)}$ is the percentile of the t-distribution with $n-p$ degrees of freedom, n is the number of observation and p is the number of regression coefficients. Here p is 2 (trend estimate and intercept). Because each datasets have different resolution, the individual component of sea-level were regridded to a regular 1° grid by linear interpolation to facilitate comparison for spatial distribution. To assess the time series of regional sea-level budget, all individual datasets were averaged over all grid cells within each basin, as depicted in Figure 3.3.1. Then, the ensemble mean of each process dataset was computed to estimate the sea-level budget.

Sterodynamic process (SL_{SD}) leads to sea-level change due to ocean density and circulation changes. Also, SL_{SD} can be estimated by the sum of steric sea-level (SSL) due to density

changes in local water column and part of manometric sea-level induced by ocean mass redistribution (OMR). Recent advances in Gravity Recovery and Climate Experiment (GRACE) data processing and Argo array floats enable the estimate of manometric sea-levels due to changes in ocean mass and reliable SSL over 0–2000 m, respectively. Here, we estimate the observation-based sterodynamic contribution by combining Argo-observed SSL with GRACE-derived OMR.

The local SSL is calculated by vertically integrating density anomalies at each grid point and each time step: $SSL = \int_H^0 \frac{\rho(P,S,T)-\rho(P,S_0,T_0)}{\rho(P,S_0,T_0)} dz$, where T, S, and P are in-situ temperature, salinity, and pressure respectively, T_0, S_0 are reference temperature and salinity (0°C, 35psu), and H is local depth. For the SSL component, we use three monthly in situ-based products (IAP, EN4, and JMA) at 1° by 1° grid over 2003 January to 2017 June. An ensemble mean of these datasets is used to estimate the local SSL trend in each marginal sea and the uncertainty is given by standard deviation.

Since 2002, the GRACE provides global measurements of ocean bottom pressure that enable the monitoring of mass contribution to SLR budget. Local changes in ocean mass derived from GRACE measurements are represented by the sum of ICE, LWS, and OMR components: $Mass = ICE + LWS + OMR + Res$. From this relationship, we can estimate the OMR change by subtracting the ICE and LWS contributions from the water mass if assuming negligible residual component (Res) that includes earthquake (Chao and Liau, 2019) and sedimentation signals (Liu et al., 2016; Chang et al., 2019), and uncertainties in GRACE processing. We use monthly GRACE RL06 mass concentration (mascon) from the three products – the NASA Goddard Space Flight Center (GSFC, Loomis et al., 2019), the Jet Propulsion Laboratory (JPL, Wiese et al., 2016), and the Center for Space Research (CSR, Save et al., 2016) from 2003 January to 2017 June because the GRACE mission ended in

October 2017 due to battery failure (Tapley et al., 2019). The GRACE data includes a leakage near the coastline due to a mixture of land and ocean signals. To address this leakage problem in coastal areas, the unregularized least squares estimator was applied in GSFC products, a Coastline Resolution Improvement (CRI) filter was applied to JPL products, and the new hexagonal grid was defined in CSR products. All products applied GIA correction based on the ICE6G-D model from Peltier et al. (2018). For the mass changes from ICE and LWS, we use the estimate of Frederikse et al. (2020).

3.3.3. Regional SLR assessment and underlying processes

Over the altimeter era (1993–2017), the geocentric sea-level exhibited a faster SLR rate in three marginal seas than in the GMSL2 (3.1±0.4 mm/yr), with a relatively slower rate in the North Pacific subtropical gyre (Figure 3.3.1b). To identify the contribution of underlying processes to the regional SLR trend, we compare the observed SLR trends to the sum of estimates of individual contributors (Figure 3.3.2). The main contributions to the regional SLR trend are the ongoing mass redistribution including land-ice mass (ICE) and land water storage (LWS) changes, i.e., contemporary-GRD, and the sterodynamic components, while GIA has little effect on the rate of SLR by ~ 0.1 mm/yr along the continental shelves.

The SLR of contemporary ICE and LWS is nearly spatially uniform in the marginal seas, and the land-ice mass changes, due to glaciers and ice sheets, dominate the rate of the regional SLR trend associated with the redistribution of the ongoing mass (Figure 3.3.2a and b). The LWS also makes a positive contribution to the regional SLR trend, with a roughly uniform trend over the northwestern Pacific. GIA has a large effect on areas close to former ice-age burdens like North America, North Europe, and Antarctica (Peltier et al., 2004; Caron et al., 2018; Peltier et al., 2018), whereas it has little impact on the SLR trend in the northwestern Pacific, with a maximum of 0.14 mm/yr in the YECS (Figure 3.3.2c). In contrast, the spatial pattern revealed in the geocentric sea-level rise are primarily caused by sterodynamic contribution (Figure 3.3.2d), which is estimated by the sum of observation-based global mean thermosteric sea-level (GMTS) and the regional dynamic sea-level from ocean reanalysis products (Details in section 2.2). In the western Pacific, the most dominant feature of the sterodynamic sea-level trend is a strong north-south contrast, with positive trends in the tropical region and negative trends in the subtropical North Pacific. This spatial pattern may be related to a decrease in the wind stress curl over the north Pacific since the late 1990s, which

caused a weakening in the North Pacific subtropical gyre and Kuroshio intensity (Andres et al., 2011; Wu et al., 2019; Jo et al., 2022). Climate-related surface wind forcing can drive changes in ocean circulation, spatially redistributing heat and water masses, resulting in the regional dynamic changes (Timmermann et al., 2010; Piecuch and Ponte, 2011; Merrifield et al., 2012; Moon et al., 2013; Cha et al., 2018).

Figure 3.3.3 presents the mean sea-level budget time series for the three marginal seas, for which the sum of individual processes accounts for the observed SLR trends. According to the altimetry-based SLR trends, the SCS is experiencing the fastest rate (4.15±0.38 mm/yr) of SLR in the northwestern Pacific marginal seas, followed by the EJS (3.95±0.46 mm/yr) and YECS (3.5±0.48 mm/yr). Although there exists a disagreement between the sum of estimated contributors and geocentric SLR trends for the SCS (3.30±0.34 mm/yr), the sum of contributors is comparable to the geocentric SLR trends for YECS (3.62±0.42 mm/yr) and EJS (3.34±0.36 mm/yr). Trends of individual components show that the land ice melt and sterodynamic components are the major contributors, while GIA has a slightly positive contribution (Table 3.3.1). The mass loss from land ice that causes a roughly uniform trend explains approximately 45.4% to 51.3% of the sum of the contributors in these marginal seas, representing one of the dominant contributions to regional SLR trends. The contribution of the LWS is small with a positive trend for these marginal seas. The sterodynamic processes also determine most of the temporal evolutions in regional SLR, with 1.63±0.41 mm/yr, 1.38±0.38 mm/yr, and 1.28±0.35 mm/yr for the ECS, SCS, and EJS, which correspond to contributions of 45.1%, 42.0%, and 38.5%, respectively. Furthermore, interannual sea-level variations over these marginal seas are indeed driven by sterodynamic effects, which account for approximately 98% of the total variance of the regional SLR. The correlation coefficients between the total sea-level and sterodynamic component reach 0.95, 0.97, and 0.94 in the ECS, SCS, and EJS, respectively. These estimates reveal that sterodynamic effects play a critical

role in driving the spatial and temporal variations in regional SLR in the northwestern Pacific (Dangendorf et al., 2021; Wang et al., 2021).

Table 3.3.1. Trends (mm/yr) of satellite-altimetry, individual contributors, and the sum of all components over 1993-2017 and 2003-2016. The number in brackets represents explained percentage of the individual contributor to the sum of all contributions. Bottom numbers present the correlation between satellite-altimetry and the sum of all components.

	Trend (mm/yr) from 1993 to 2017		
	YECS	**SCS**	**EJS**
Satellite-altimetry	3.50±0.48	4.15±0.38	3.95±0.46
ICE	1.64±0.03 (45.4%)	1.55±0.03 (47.0%)	1.71±0.03 (51.3%)
LWS	0.25±0.02 (6.8%)	0.30±0.02 (9.1%)	0.29±0.02 (8.6%)
Sterodynamic	1.63±0.41 (45.1%)	1.38±0.38 (42.0%)	1.28±0.35 (38.5%)
GIA	0.10±0.05 (2.8%)	0.06±0.03 (1.9%)	0.06±0.05 (1.7%)
Sum of all components	3.62±0.42	3.30±0.34	3.34±0.36
Corr. (altimetry vs. Sum)	0.95	0.98	0.95

	Trend (mm/yr) from 2003 to 2016		
	YECS	**SCS**	**EJS**
Satellite-altimetry	4.48±1.06	5.24±0.95	3.88±1.00
ICE	2.05±0.02 (52.9%)	1.92±0.02 (63.7%)	2.14±0.03 (55.5%)
LWS	0.25±0.06 (6.6%)	0.32±0.06 (10.6%)	0.30±0.06 (7.8%)
Steric	0.24±0.18 (6.2%)	0.89±0.69 (29.5%)	0.68±0.29 (17.7%)
OMR	1.23±0.86 (31.8%)	-0.18±0.35 (-5.8%)	0.68±0.69 (17.6%)
GIA	0.10±0.05 (2.6%)	0.06±0.03 (3.3%)	0.06±0.05 (1.5%)
Sum of all components	3.47±0.89	2.86±0.79	3.64±0.77
Corr. (altimetry vs. Sum)	0.89	0.87	0.86

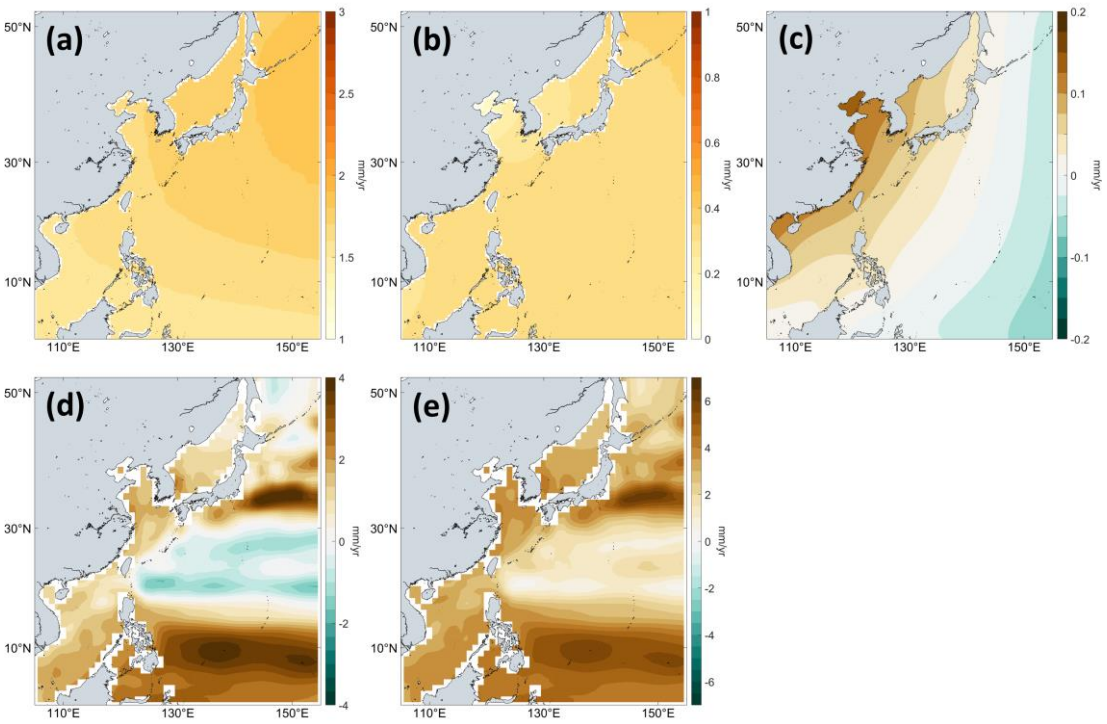

Figure 3.3.2. Sea-level rise trend from the individual contributor. Regional maps of the estimated individual contributor of SLR trend in the northwestern Pacific over 1993-2017: (a) ICE, (b) LWS, (c) GIA, (d) Sterodynamic effect, and (e) the sum of all components. The components of ICE and LSW are derived from the estimates from Fredrikese et al. (2020) and GIA contribution is examined using the estimate of Caron et al. (2018). The sterodynamic contribution is estimated by the sum of observation-based GMTS and regional dynamic sea-level from ocean reanalysis products (Figure 2.2). Details in section 2.2.

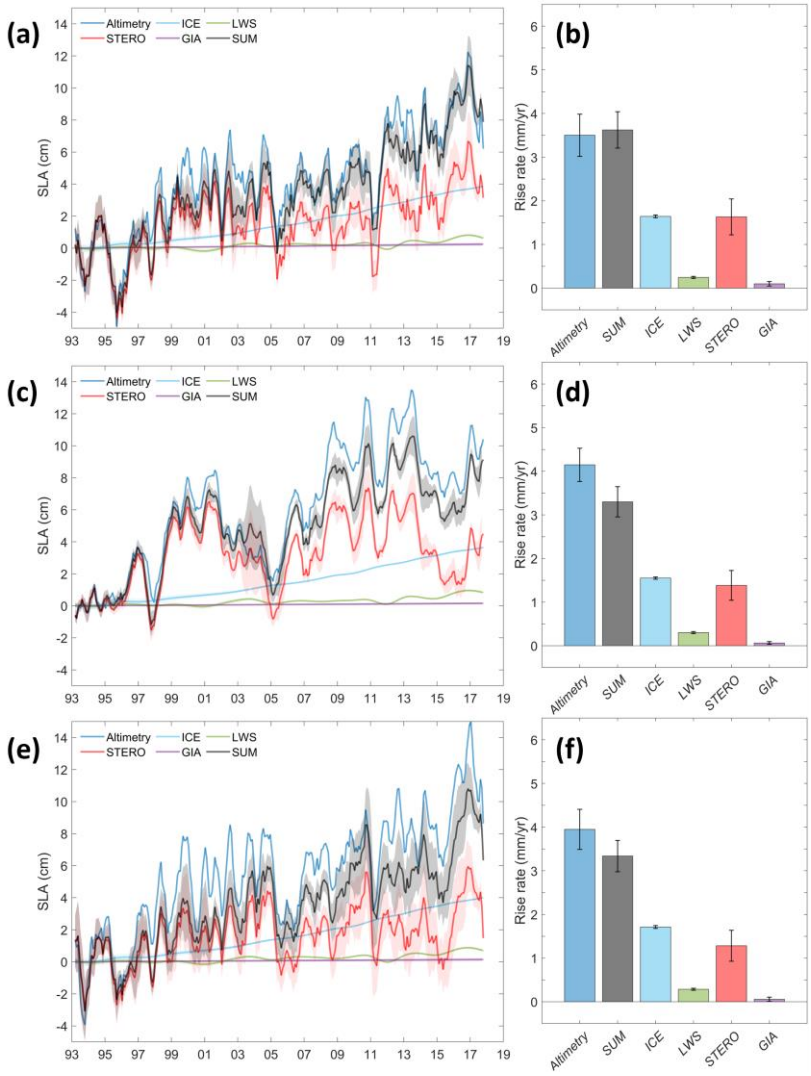

Figure 3.3.3. Mean sea-level budget time series and trends over 1993–2017. (a) Time series of mean sea-level in the YECS from altimetry (blue), ICE (light-blue), LWS (green), sterodynamic (red), and GIA (purple). Shaded areas represent one standard deviation uncertainty among each time series. (c) same as (a) but for SCS. (e) same as (a) but for EJS. The trend budget of SLR for (b) YECS, (d) SCS, and (f) EJS, respectively. Error bar represents 95% confidence intervals estimated slope of uncertainty.

3.3.4. Observation-based estimate of sterodynamic SLR

As described in the above subsection, the sterodynamic contribution was estimated by combining in situ-based global thermosteric signal with the regional dynamic sea-level from ocean models. Equally, the sterodynamic sea-level can be expressed by the sum of the SSL due to density changes in the local water column and sea-level induced by circulation-driven OMR. Recent advances in GRACE data processing and in situ-based profiles have enabled the estimate of manometric sea-level due to changes in ocean mass and reliable SSL, respectively. Here, we attempt to assess the observation-based sterodynamic contribution by combining in situ-based SSL with the GRACE-derived OMR due to changes in ocean processes from 2003 January to 2017 June. This approach based on the combined use of in situ-based profiles and GRACE observations allows a direct comparison with available observations of individual processes on regional scales, which provides a complete picture of the underlying regional sea-level dynamics. The circulation-driven OMR component can be estimated by subtracting the mass changes from the ICE and LWS fingerprints from the GIA-corrected GRACE data.

It should be noted that during the GRACE period, the two strongest earthquakes of the 2004 Sumatra and 2011 Tohoku occurred in the northwestern Pacific marginal seas. The GRACE mascon data includes the two strongest earthquake signals that affect the local changes in ocean mass trends. We applied an empirical orthogonal function (EOF) analysis to remove the signals during the earthquake periods, which was recently reported by Chao and Liau (2019). Figures 3.3.4-5 present the EOF results for the GRACE data based on the three products (GSFC, CSR, JPL) during the two earthquake events. For all products, the first EOF modes indicate the strongest earthquake signals over the northwestern Pacific marginal seas, explaining more than 90% of the total variance. These signals were corrected by removing the recombined loading vector with the principal component from the GRACE mass data. The

correction for the Sumatra earthquake was only applied to SCS and for the Tohoku earthquake only for the EJS (Figure 3.3.6) because of the limited extent of the influence of the earthquake signal (Figures 3.3.4-5). After the correction, we estimate observation-based OMR component by subtracting the ICE and LWS contributions from the GRACE mascon data. Several large earthquakes occurred near the SCS during the GRACE period; for example, the Indian Ocean in April 2012 (Mw 8.6) and Sumatra in September 2007 (Mw 8.5). However, both signals were not captured by EOF analysis and had a negligible effect on sea level change in the SCS. Therefore, we corrected only the two strongest earthquake signals, the 2004 Sumatra and 2011 Tohoku, to estimate observation-based OMR. We present steric sea-level (SSL) and ocean mass redistribution (OMR) spatial trend from IAP and GSFC datasets in the manuscript due to each dataset has a different spatial resolution, like GRACE JPL mascon showing gradual change along adjacent 3° mascon and CSR representing 1/4° degree. Each pattern from all GRACE products and SSL datasets are already given in Figure 3.3.7-8.

Comparing the altimetry sea-level with the sum of the observation-based sterodynamic, contemporary-GRD, and the GIA components shows reasonable agreement in spatial SLR trends during 2003–2016 (Figure 3.3.9). As mentioned above, the contemporary-GRD changes (ICE and LWS, Figure 3.3.9a and b) can explain a large portion (59.5~74.3%) of the regional SLR trends over these marginal seas (Table 3.3.1), and an increase in Greenland mass loss since the mid-2000s notably contributes to contemporary sea-level changes (Chen et al., 2017; Dieng et al., 2017). However, the sterodynamic processes are responsible for the spatial patterns of SLR trend (Figure 3.3.9c). Recent studies have indicated that steric changes alone cannot account for regional sterodynamic sea-level changes because the ocean circulation-driven OMR can play an important role in the regional SLR over continental shelves and coastal regions (Landerer et al., 2007; Dangendorf et al., 2021; Wang et al., 2021).

To further examine the sterodynamic contributions, we decompose the sterodynamic sea-level into an in situ-based local SSL component and GRACE-derived OMR component (Figure 3.3.10). Local SSL changes dominate the sterodynamic SLR in most regions during the GRACE period of 2003-2016, except along the shallow continental shelves, including the YECS. As mentioned above, negative trends over the subtropical North Pacific may be related to changes in the large-scale wind stress curl over the Pacific subtropical (Wu et al., 2019). For the deep-water regions of the SCS and EJS, positive trends of the SSL appear as the heat penetrates deeper ocean depths, but it has little impact on the shallow shelf regions (Figure 3.3.10a). We separated the SSL into thermo-SSL and halo-SSL to identify the contribution of temperature and salinity change (Figure 3.3.11). The thermos-SSL has large impacts on the spatial pattern of the SSL rise, but the contribution of halo-SSL is small in the marginal seas. In contrast with the SSL, the sterodynamic SLR along the continental shelves mainly arises from the circulation-driven OMR process rather than the local SSL changes (Figure 3.3.10b). This result is consistent with previous studies that showed the importance of ocean-bottom pressure changes induced by mass redistribution on continental shelves and coastal areas (Ponte et al., 2002; Landerer et al., 2007; Dangendorf et al., 2021). Because the thermal expansion is relatively small on the continental shelves where the water depth decreases, a net mass is transferred onto the shallower regions from the deeper ocean (see Figure. 1 of Dangendorf et al., 2021). This was also noted by Chen et al. (2021), who focused on the dominance of mass contribution in the YECS based on the results of climate model projections during the 21st century (Coupled Model Intercomparison Project Phase 5 dataset).

The time series of regional sea-level budgets and trends for the three marginal seas are shown in Figure 3.3.12, which compares the altimetric SLR with estimates of the underlying processes. The temporal evolution of the geocentric SLR agrees well with the sum of all components, and the estimates are not distinguishable within the uncertainty except for the

SCS, representing the closure of the regional SLR budget and the consistency of different datasets (Table 3.3.1). Similar to the estimate for the period of 1993–2017, the mass loss from land ice contributes more than 50% of the trend from the sum of the processes for all marginal seas and the sterodynamic process, i.e., SSL and OMR components, explains most of the temporal evolution of the regional SLR. The variability of observation-based sterodynamic sea-level was also compared with the reanalysis-based one, and the two time-series were highly correlated each other for all regions (Figure 3.3.13). This comparison gives a reliable sterodynamic contribution to regional sea-level changes that was cross-checked, suggesting an important role of ocean dynamics on regional sea levels. The contributions of the LWS and GIA were relatively small compared to those of the other processes. In particular, the sterodynamic processes for these marginal seas are attributed to geographical differences in the underlying dynamics. Along the continental shelves including the YECS, the sterodynamic sea-level is substantially induced by the circulation-driven OMR component. The rate of the circulation-driven OMR component is 1.23±0.86 mm/yr in the YECS, which explains 31.8% of the total SLR rate, while the local SSL effect makes only a small contribution (6.2%, Table 3.3.1). On the other hand, the changes in local SSL for the SCS and EJS contribute to 29.5% (0.89±0.69 mm/yr) and 17.7% (0.68±0.29 mm/yr) of the sum of the individual components, respectively, with stronger SSL rise in the deep-water regions than the surrounding continental shelf regions. The contribution from the circulation-driven OMR is relatively smaller than that of the YECS, with a rate of 0.68±0.69 mm/yr in the EJS and nearly zero in the SCS. Although the uncertainties that may arise from systematic errors of space observations are still large, these results confirm the steric-driven change in ocean bottom pressure between the deep ocean and shallow marginal seas, which play a role in driving SLR trend along the continental shelves (Landerer et al., 2007; Chen et al., 2021; Dangendorf et al., 2021).

The sum of the contributors also explains the observed sea-level fluctuations on

interannual time scales (i.e., de-trended variations), showing high correlation coefficients (> 0.85) for all marginal seas (Table 3.3.1). However, the contributor to the explained variance of sea-level variability differs among the regions: for the SCS, local SSL explains a substantial fraction of detrended sea-level changes (80%), while the fluctuations for the YECS (95%) and EJS (83%) were dominated by the circulation-driven OMR process (Table 3.3.2). Heat advection associated with westward transport through the Luzon Strait drives the basin-mean heat content in the SCS, thereby leading to SSL variability as shown in Figure 3.3.12b (Qu et al., 2006; Cheng et al., 2010; Moon et al., 2013; Jin et al., 2021). Meanwhile, the dominant variability of the circulation-driven OMR in the YECS and EJS is likely to be the result of mass exchange between the marginal sea and the rest of the ocean (Fukumori et al., 2015). Previous studies have found a near-uniform barotropic fluctuation in the EJS, with monthly to interannual timescales (Choi et al., 2004; Kim et al., 2015). This mass fluctuation may be related to a near-stationary balance between the inflow through the Korea/Tsushima Strait and the outflow through the Tsugaru and Soya Straits (Kim et al., 2015). Although not focused on in this study, further investigations of sea-level fluctuations in the EJS in line with the mass flux through the straits are required in the future.

Table 3.3.2. Percentage of explained variance of the sum of all components for SSL and OMR over 2003-2016. All time series are detrended before computing the explained variance.

	Percentage of explained variance (%) from 2003 to 2016		
	YECS	**SCS**	**EJS**
SSL	2%	80%	14%
OMR	95%	19%	83%

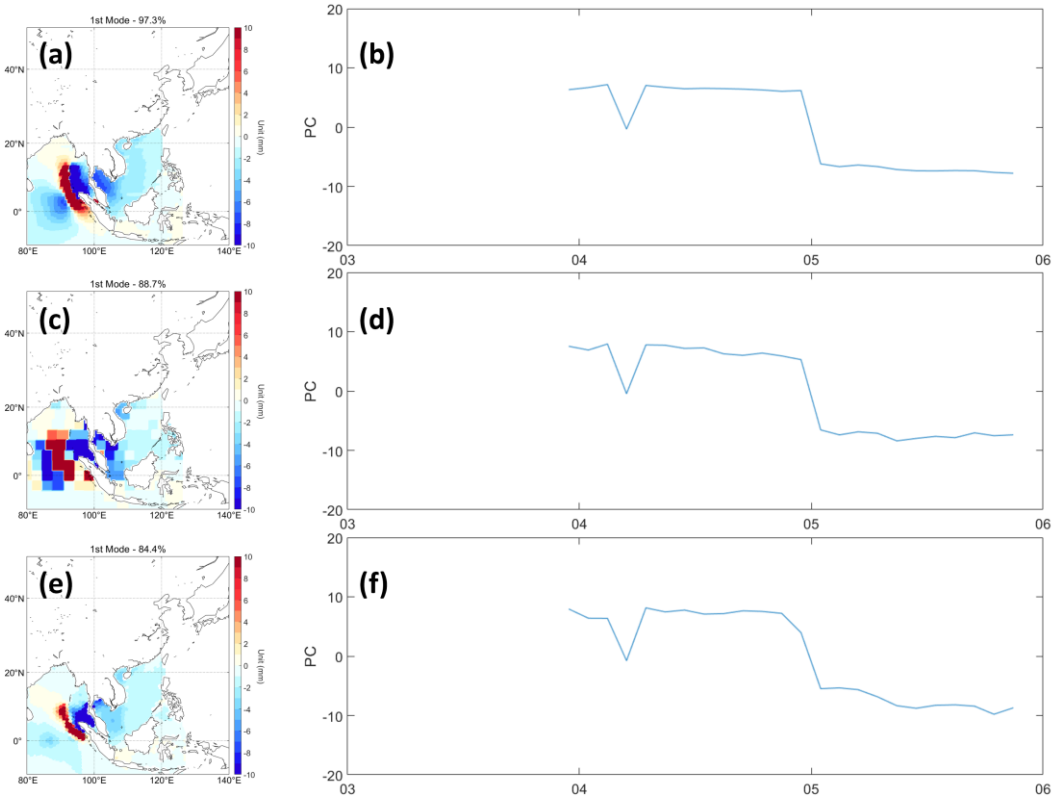

Figure 3.3.4. The EOF results for the GRACE datasets. Spatial pattern (left) and principal component time series (right panels) of the EOF first mode of the manometric sea-level representing Sumatra earthquake signal on December 2004 based on the GRACE products: (a, b) GSFC, (c, d) JPL, and (e, f) CSR. The EOF analysis is applied for the periods from 1 year before through 1 year after the earthquakes.

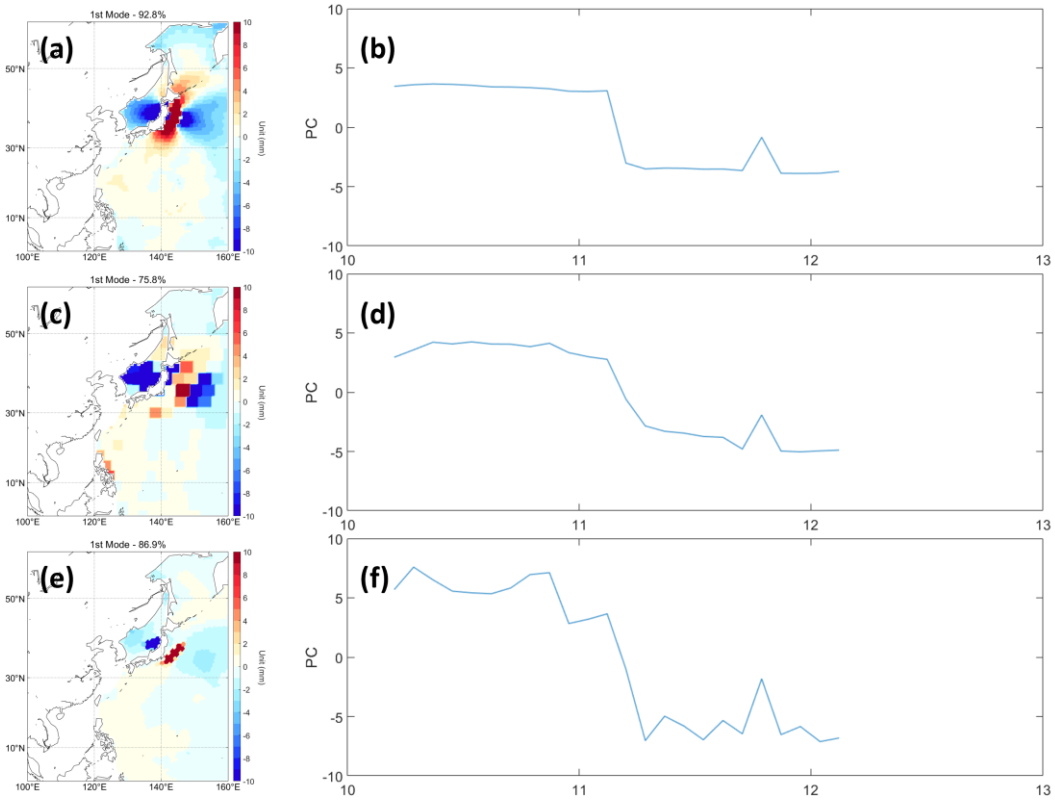

Figure 3.3.5. Same as Figure 3.3.4 but for Tohoku earthquake on March 2011.

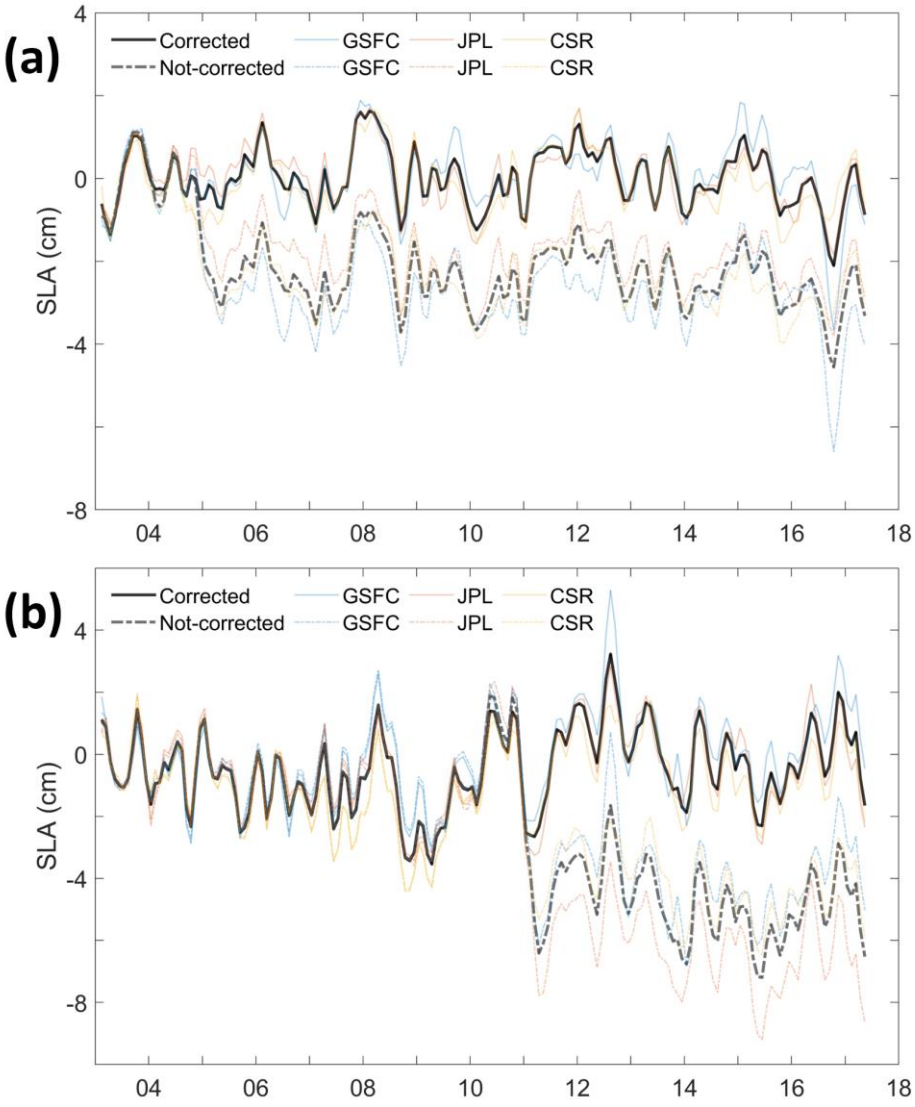

Figure 3.3.6. Comparison of GRACE-derived OMR. Time series of OMR for three different products from GSFC (blue), JPL (red), and CSR (yellow) before (dashed lines) and after (solid lines) EOF-based correction for the 2004 Sumatra-Andaman and 2011 Tohoku earthquakes in (a) SCS and (b) EJS from 2003 January to 2017 June. The ensemble mean is shown by black line.

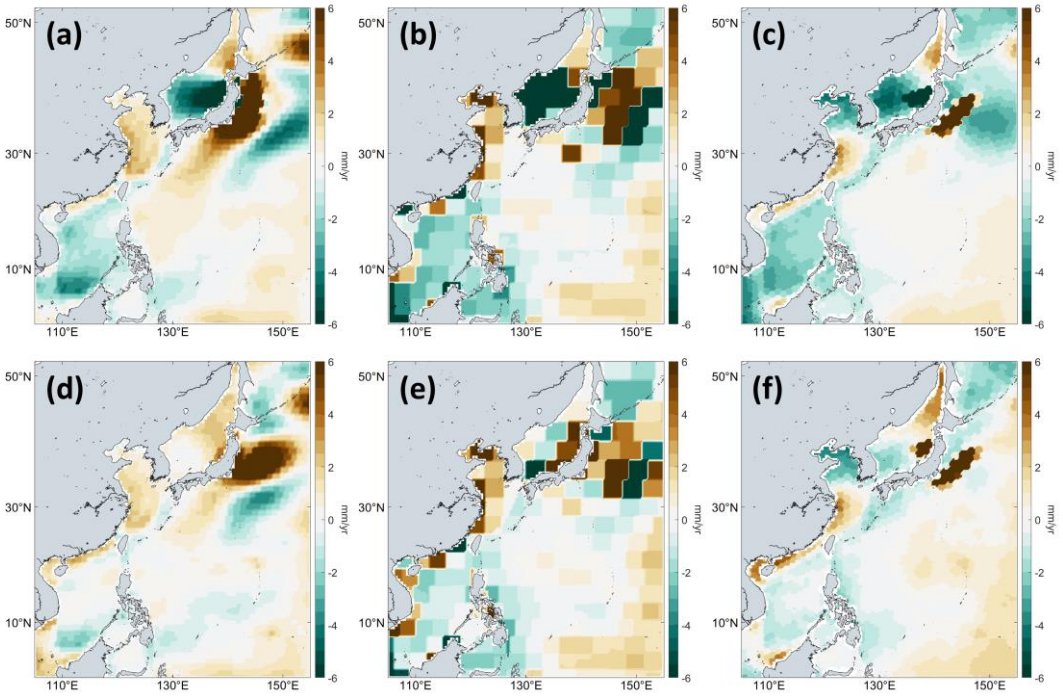

Figure 3.3.7. Sea-level rise trend from GRACE-derived OMR component. Regional trend maps of the OMR in the northwestern Pacific from three different products: (a, d) GSFC, (b, e) JPL, and (c, f) CSR before (upper) and after (lower) EOF-based correction for the 2004 Sumatra-Andaman and 2011 Tohoku earthquakes over 2003-2016.

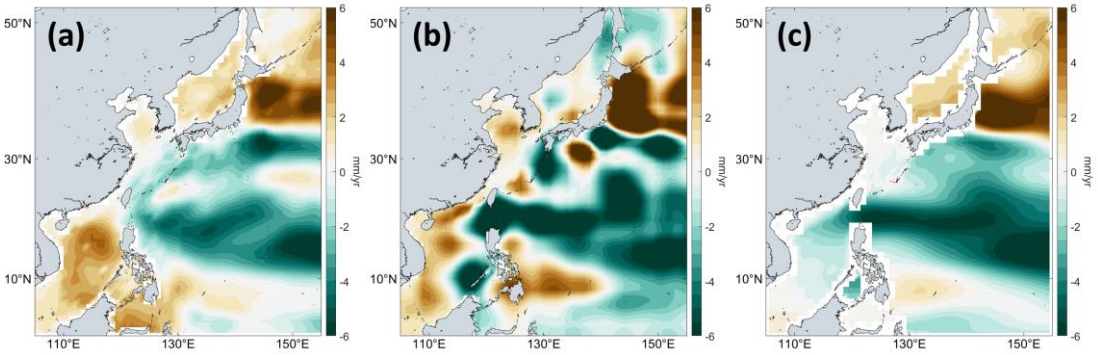

Figure 3.3.8. The in situ-based SSL trend. Regional trend maps of the local SSL in the northwestern Pacific derived from three different products over 2003-2016: (a) IAP, (b) EN4, and (c) JMA.

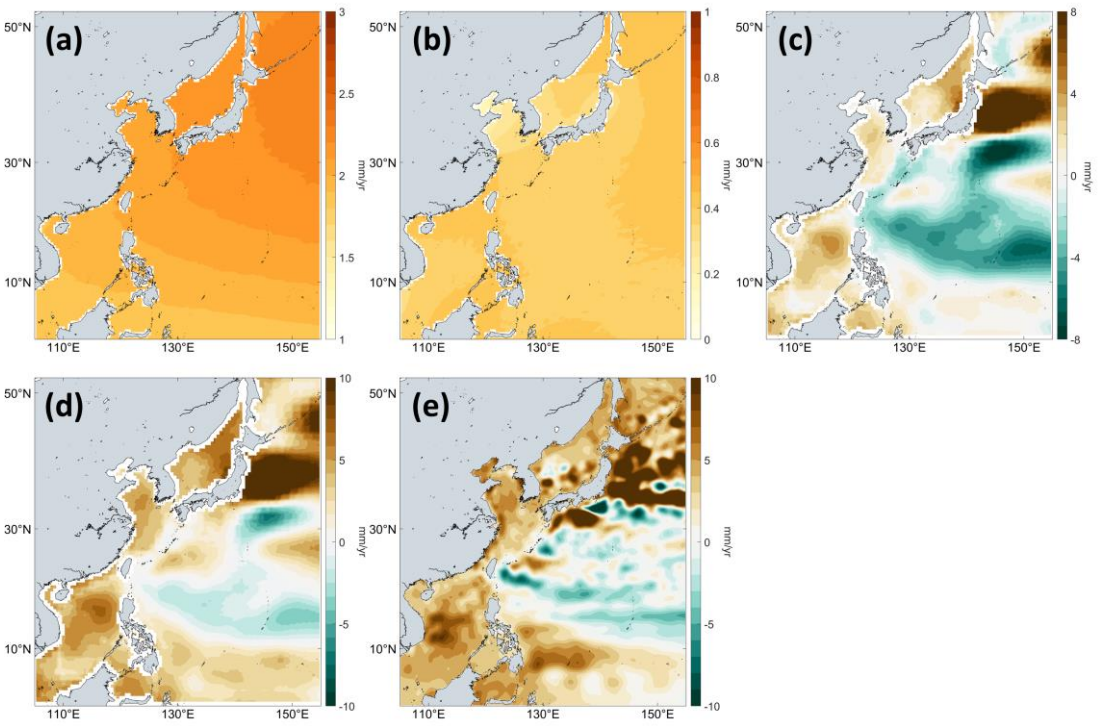

Figure 3.3.9. Sea-level rise trend from the individual contributor and satellite-altimetry. Regional maps of the estimated individual contributor and satellite-altimetry of SLR trend in the northwestern Pacific over 2003-2016: (a) ICE, (b) LWS, (c) Sterodynamic effect, (d) the sum of all components, and (e) satellite-altimetry. The sterodynamic contribution is estimated by directly combining in situ-based SSL from IAP product with the GRACE-derived OMR from GSFC product. The GIA trend in Figure 3.3.2c was used to calculate the sum of all components.

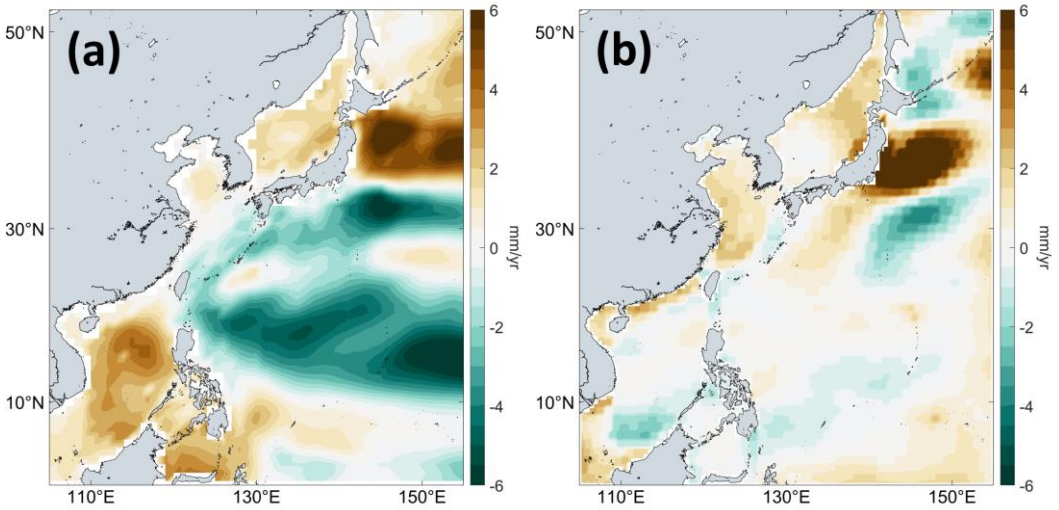

Figure 3.3.10. Observation-based SSL and OMR trend. Regional maps of SLR trend for (a) local SSL and (b) OMR components in the northwestern Pacific over 2003-2016. Data sources are based on IAP product for SSL and GSFC product for OMR, respectively. The other data sources for SSL and OMR components are also shown in Figures 3.3.7-8.

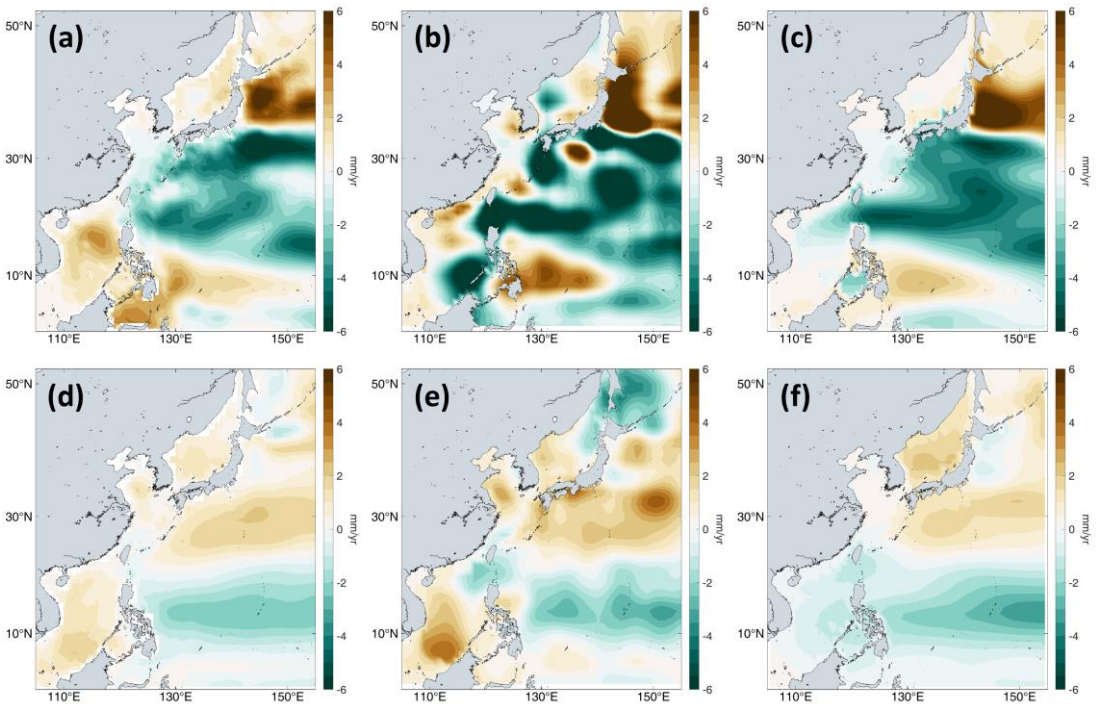

Figure 3.3.11. The in situ-based thermo-SSL and halo-SSL trend. Regional trend maps of the thermo-SSL and halo-SSL in the northwestern Pacific derived from three different products over 2003-2016: (a,d) IAP, (b,e) EN4, and (c,f) JMA.

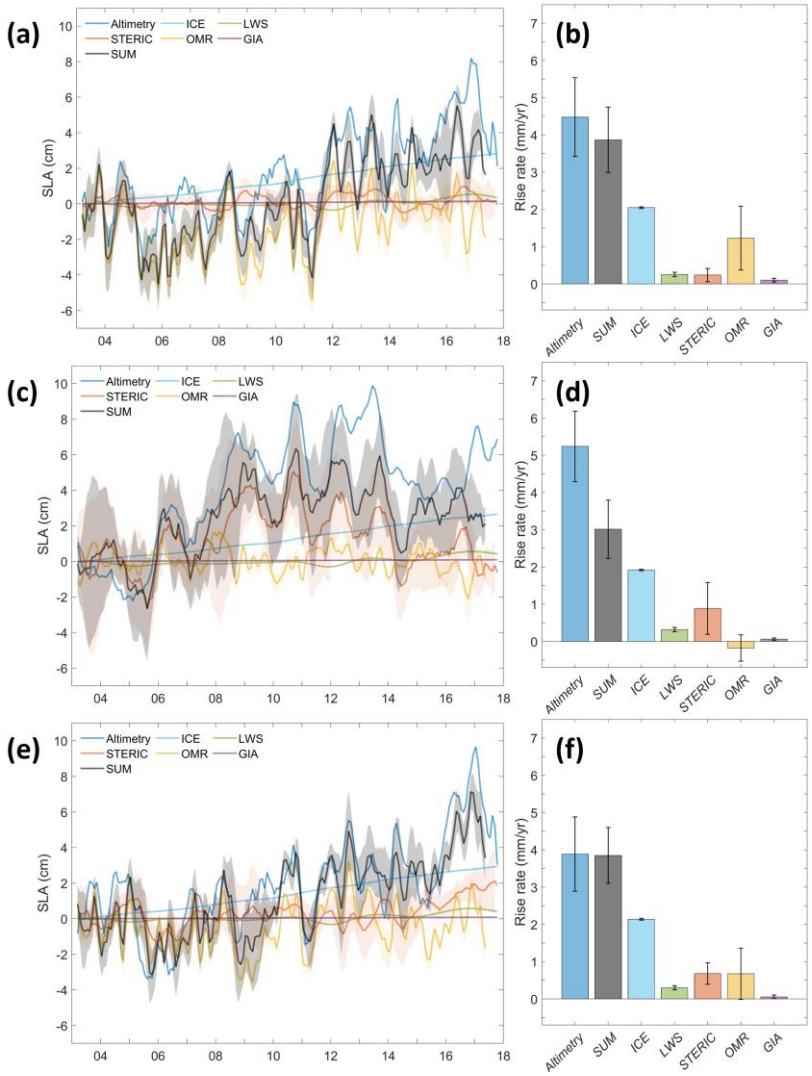

Figure 3.3.12. Mean sea-level budget time series and trends over 2003-2016. (a) Time series of mean sea-level in the YECS from altimetry (blue), ICE (light-blue), LWS (green), situ-based SSL (orange), GRACE-derived OMR (yellow), and GIA (purple). For SSL component, we used in situ-based products: IAP, EN4, and JMA and an ensemble mean of these datasets is used. For OMR component, we used the GRACE from different products: GSFC, JPL, and CSR and an ensemble mean of these products is used. Shaded areas represent one standard deviations uncertainty among each time series. (c) same as (a) but for SCS, and (f) EJS, respectively. Error bar represent 95% confidence intervals estimated slope of uncertainty.

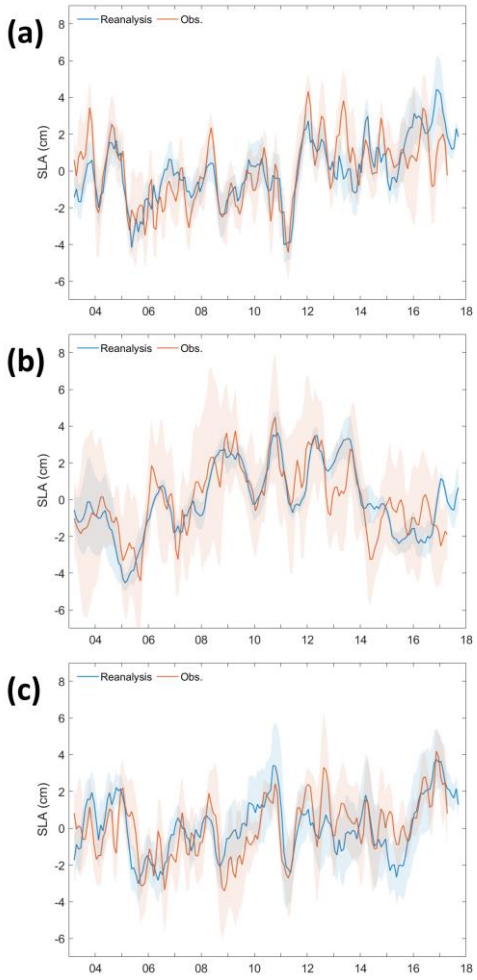

Figure 3.3.13. Comparison of sterodynamic sea-level of reanalysis and observation datasets. Regional mean sterodynamic sea-level change estimated from reanalysis (blue) and observation (red) datasets over 2003-2017. (b) same as (a) but for SCS. (c) same as (a) but for EJS. The correlation (root mean square difference) between reanalysis-based sterodynamic and observation-based sterodynamic is 0.68 (1.41), 0.77 (1.23), and 0.60 (1.90) in YECS, SCS, and EJS, respectively. For reanalysis-based sterodynamic, we averaged sterodynamic sea level from GECCO3 and ECCO v4. For observation-based sterodynamic, we sum the ensemble mean of SSL component and OMR component from different products: IAP, EN4, and JMA for SSL and GSFC, JPL, and CSR for OMR.

3.3.5. Discussion and Conclusion

Recent advances in observation have improved the understanding of the GMSL budget and underlying processes, however, the process-based assessment on regional scales is still challenging due to several physical processes with spatial and temporal variability. Because sea-level changes occurring over regional scales pose a threat to coastal communities with high population density, understanding and quantifying the underlying regional processes is of great importance. This study assessed the regional SLR budget in the northwestern Pacific marginal seas in terms of different individual processes. To provide a better understanding of the underlying processes, we examined whether the regional sea-level budget can be closed with a combination of observations and ocean reanalyses over 1993–2017, as well as with independent observations from in situ-based profiles including Argo floats and satellite gravity measurement since 2003.

By comparing the sum of the estimated reanalysis-based contributions with the altimetry SLR, it was found that the trend of the sum is comparable to the geocentric SLR trends for YECS and EJS. Trends of individual process show that the land ice and sterodynamic are the major contributors for all three marginal seas, while GIA has a small contribution. The mass loss from land ice explains a large fraction (~ 50%) of the observed SLR trends over the northwestern Pacific, which is consistent with previous estimates of the GMSL budget (Frederikse et al., 2020; Cha et al., 2021). Unlike the land ice contribution, the spatial pattern of the SLR trend and its interannual variability after detrending are dominated by sterodynamic processes (Dangendorf et al., 2021; Wang et al., 2021). To examine the detailed sterodynamic processes, the sterodynamic sea-level was further decomposed into two processes, local SSL and circulation-driven OMR components, using completely independent datasets from in situ profiles and GRACE measurements since 2003. Along continental shelves including the YECS,

the sterodynamic sea-levels are substantially induced by the circulation-driven OMR component, which accounts for approximately one third of the total SLR rate, while the steric effect makes only a small contribution. In contrast, the changes in the local SSL for the SCS and EJS differently contribute to the sum in spatial patterns, with a stronger SSL rise in the deep-water region than in the surrounding continental shelf area. These results highlight the circulation-driven change in ocean mass between the deep ocean and shallow marginal seas, which drives regional SLR trend and their interannual variability along the continental shelves (Landerer et al., 2007; Chen et al., 2021).

Our results show that the regional SLR budget in YECS and EJS can be reasonably close to independent observational datasets. However, a large gap exists in the SCS, indicating that the trend of the sum is much smaller than that in the altimetry SLR. One possible source of underestimation may be associated with local SSL estimates based on in situ and Argo measurements (Figure 3.3.8 and 3.3.14). The comparison among the three SSL estimates shows a substantial spread around the ensemble mean for the SCS, which is approximately three times larger than those for the YECS and EJS. This indicates an inconsistency in different datasets, especially in the SCS, which may arise from insufficient sampling, instrumental biases, and mapping choices (Dieng et al., 2015; Boyer et al., 2018; Camargo et al., 2020). Despite systematic errors in space measurement and in situ uncertainties, this observation-based SLR budget demonstrates the utility of independent observational platforms for a process-based assessment by achieving the regional SLR budget closure. As efforts to improve and continue to lengthen both satellite measurements and in situ observations, our understanding of relevant processes will be enhanced with respect to monitoring and projecting regional sea-level changes that improve the basis for future vulnerability.

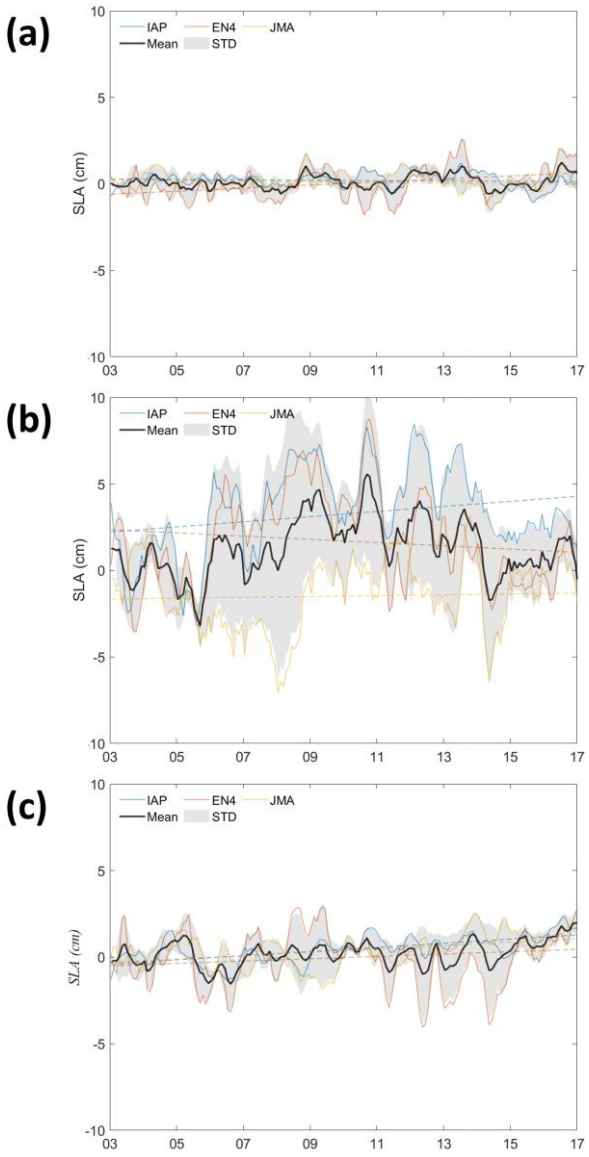

Figure 3.3.14. Comparison of the in situ-based local SSL. Regional mean SSL time series in (a) YECS, (b) SCS, and (c) EJS from three different products: IAP (blue), EN4 (red), and JMA (yellow). Ensemble mean time series is shown by black line and one standard deviation uncertainty indicated by gray shading.

Chapter 4 Conclusion

Present-day global mean sea-level change is the key indicator of climate change, including ocean and cryosphere. While global mean sea-level rise implies rising sea-level for the world's oceans, the regional response is not uniform. Mass input from melting glaciers, ice sheets, and land water change will not be distributed evenly everywhere due to Earth's Gravity, Rotation, and Deformation effects from mass exchange between land and ocean. Sterodynamic effect is comprised of density changes in the local water column (steric sea-level) and circulation-driven ocean mass redistribution and drives the spatial and temporal variations in regional sea-level rise. Especially, circulation-driven ocean mass redistribution, which has zero global mean, can play an important role in the sea-level change over shallow region than deeper region (section 3.2). Using advanced satellite altimetry and in situ measurement, the extent of global and regional sea-level rise can be understood. However, there is still a lack of understanding of how natural climate variability and physical processes contribute to sea-level rise. Also, sea-level varies on various time scales, from short-term change to seasonal-to-decadal variability or longer. The contribution to sea-level at each time scales can combine with ongoing sea-level rise, increasing sea-level rise and flood risk over the short and long term. It is essential to estimate sea-level change at different time scales for improved information regarding future sea-level rise. Therefore, this dissertation aims to understand the impact of decadal climate variability on the global and tropical Pacific sea-level change and the role of each physical process in sea-level rise on the northwestern Pacific marginal seas. The major findings of this study are as follows:

Firstly, despite continuous global warming, the global mean sea-level rise stagnated over the 2000s and increased again since 2010. Decadal climate-driven land water storage and steric sea-level change largely account for this decadal fluctuation in global mean sea-level rise. Also,

the increase in ocean heat uptake since 2011 is linked to Pacific decadal climate variability. These results can clarify the ocean's role in the global hydrological cycle, earth energy imbalance, and perspectives on continuous sea-level change. For example, Pacific decadal climate-driven signals can accelerate or decelerate ongoing global mean sea-level rise. The cross-validation of Earth's energy imbalance emphasizes the consistency of energy gaining in Earth's climate system. However, systemic altimetry errors and in situ observation uncertainties still remain large due to unsampled regions, instrumental bias, and mapping choice. Therefore, it is essential to extend satellite measurement and deep ocean (deeper than 2000m) observation for a better understanding of global sea-level rise and the Earth's energy imbalance in the future.

Secondly, a dramatic shift toward an El Nino-like state in the tropical Pacific was observed in satellite altimetry and in situ measurement. EEMD analysis demonstrates a distinct decadal mode in the tropical Pacific, corresponding to the recent shift. This decadal fluctuation also shows a clear connection with the decadal period of global ocean warming, which likely contributed to the suppression of global warming over the 2000s and the resumption of warming in the last few years. The decadal mode in the tropical Pacific is associated with the PDO-related trade wind change on the decadal timescale. Model experiment shows that upper-ocean circulation associated with the Pacific climate variability can control the sea-level trend, subsurface temperature change, and strength of the equatorial undercurrent on the decadal timescale. These results suggest that the Pacific decadal climate variability can impact on global ocean warming on low-frequency fluctuation. Also, this study has implications for decadal predictions of sea level and global ocean warming. For example, if trade winds persistently strengthen associated the decadal climate variability, a global ocean warming slowdown can occur with a La Nina-like pattern in the tropical Pacific.

Lastly, this study assessed the regional sea-level rise in the northwestern Pacific marginal seas. It examined whether the sea-level budget can be closed with a combination of observation and ocean reanalyses over 1993-2017, as well as with independent observation from in situ profiles including Argo floats and satellite gravity measurements since 2003. The results show that ice melting and sterodynamic process are the major contributors to sea-level rise, while the spatial pattern and interannual variability are dominated by sterodynamic effect. The observation-based sterodynamic estimation shows that along continental shelves, sterodynamic sea-level is substantially induced by ocean mass redistribution due to changes in ocean circulation. In contrast, the local steric process contributes more to sea-level rise in the deep-water region than in the surrounding shelf area. This result highlights the ocean mass change between the deep ocean and shallow marginal seas, which plays a role in driving regional sea-level rise and variability. Furthermore, the observation-based regional sea-level rise budget closure shows the utility of independent observation platforms for a process-based assessment. Efforts to improve observation networks, including satellite altimetry and in situ measurement, can enhance our understanding of sea-level changes and improve future vulnerabilities.

Chapter 5 Discussion

This study showed significant progress, which has been made in understanding sea-level rise and decadal variability by identifying the role of climate variability on the decadal time scale and estimating the contribution of physical processes. Nonetheless, additional investigation should be considered for the future study. For example, our results have shortcomings in understanding sea-level rise near the coast because these studies focus on global and regional scales. Since much of the world's population lives near the coast, understanding local processes is also crucial to prevent the risk of sea-level rise and flooding. A combination of observation and reanalyses may reproduce sea-level rise at the tide gauges, but the low-resolution ocean models do not well resolve the ocean dynamics on coastal sea-level change. Improvements in the knowledge of comprehensive processes and increasing model resolution will provide confidence in projecting future sea-level change at the coast. Additionally, vertical land motion, affected by anthropogenic and natural processes such as groundwater depletion, tectonic motion, and sediment compaction, is the dominant factor causing significant spatial variation at the coast (Chen et al., 2018). Estimating vertical land motion is crucial to understanding sea-level changes at the coast. However, the current shortage of GPS stations near the tide gauges can complicates accurate assessments of sea-level rise. Nevertheless, evaluating local effects and identifying the physical process is necessary to improve coastal sea-level projections.

Another significant progress in this study is that the budget of independent datasets in sea-level and Earth's energy imbalance can be reasonably consistent within uncertainties (sections 3.1 and 3.3). Despite the improvement in the independent observing system, many parts of the oceans are still undersampled. There is bias and uncertainties in not well-sampled regions, making it difficult to estimate steric sea-level and ocean heat content change (Llovel et al.,

2014; Hamlington et al., 2020). Because Argo floats originally planned to cover the upper 2000m and open ocean below 60° latitude (Riser et al., 2016), there are gaps in the deep ocean below 2000m, in marginal seas, and in the polar regions (von Schuckmann et al., 2020). Thus, extending observation to the deep ocean is essential for a better understanding of sea-level change and rigorous evaluation of energy change in Earth's climate system. Extending satellite measurement and in situ monitoring and exploring deep ocean, such as the deep Argo program and Global Ocean Ship-Based Hydrographic Investigation Program (GO-SHIP) will help to elucidate the contribution of deep ocean warming (Johnson et al., 2015).

References

Ablain, M., Legeais, J. F., Prandi, P., Marcos, M., Fenoglio-Marc, L., Dieng, H. B., … Cazenave, A. (2017). Satellite Altimetry-Based Sea Level at Global and Regional Scales. Surveys in Geophysics, 38(1), 7–31.

Andres, M., Kwon, Y. O., & Yang, J. (2011). Observations of the Kuroshio's barotropic and baroclinic responses to basin-wide wind forcing. Journal of Geophysical Research: Oceans, 116(4), 1–12.

Beckley, B. D., Callahan, P. S., Hancock, D. W., Mitchum, G. T., & Ray, R. D. (2017). On the "Cal-Mode" Correction to TOPEX Satellite Altimetry and Its Effect on the Global Mean Sea Level Time Series. Journal of Geophysical Research: Oceans, 122(11), 8371–8384.

Boening, C., Willis, J. K., Landerer, F. W., Nerem, R. S., & Fasullo, J. (2012). The 2011 la Nia: So strong, the oceans fell. Geophysical Research Letters, 39(19), 1–5.

Boyer, T.P. et al. (2018). World Ocean Database 2018. A.V. Mishonov, Technical Ed., NOAA Atlas NESDIS 87

Camargo, C. M., Riva, R. E., Hermans, T. H., & Slangen, A. B. (2020). Exploring Sources of Uncertainty in Steric Sea-Level Change Estimates. Journal of Geophysical Research : Oceans.

Camargo, C. M., Riva, R. E., Hermans, T. H., Schütt, E. M., Marcos, M., Hernandez-Carrasco, I., & Slangen, A. (2023). Regionalizing the sea-level budget with machine learning techniques. Ocean Science, 19(1), 17-41.

Caron, L., Ivins, E. R., Larour, E., Adhikari, S., Nilsson, J., & Blewitt, G. (2018). GIA Model Statistics for GRACE Hydrology, Cryosphere, and Ocean Science. Geophysical Research

Letters, 45(5), 2203–2212.

Carton, J. A., Penny, S. G., & Kalnay, E. (2019). Temperature and salinity variability in the SODA3, ECCO4r3, and ORAS5 ocean reanalyses, 1993-2015. Journal of Climate, 32(8), 2277–2293.

Cazenave, A., Dieng, H. B., Meyssignac, B., Von Schuckmann, K., Decharme, B., & Berthier, E. (2014). The rate of sea-level rise. Nature Climate Change, 4(5), 358–361.

Cha, S. C., Moon, J. H., & Song, Y. T. (2018). A Recent Shift Toward an El Niño-Like Ocean State in the Tropical Pacific and the Resumption of Ocean Warming. Geophysical Research Letters, Vol. 45, pp. 11,885-11,894.

Cha, H., Moon, J.-H., Kim, T., & Song, Y. T. (2021). Underlying drivers of decade-long fluctuation in the global mean sea-level rise. Environmental Research Letters, 16(12), 124064.

Chambers, D. P., Cazenave, A., Champollion, N., Dieng, H., Llovel, W., Forsberg, R., … Wada, Y. (2017). Evaluation of the Global Mean Sea Level Budget between 1993 and 2014. Surveys in Geophysics, 38(1), 309–327.

Chang, L., Tang, H., Yi, S., & Sun, W. (2019). The Trend and Seasonal Change of Sediment in the East China Sea Detected by GRACE. Geophysical Research Letters, 46(3), 1250–1258.

Chao, B. F., & Liau, J. R. (2019). Gravity Changes Due to Large Earthquakes Detected in GRACE Satellite Data via Empirical Orthogonal Function Analysis. Journal of Geophysical Research: Solid Earth, 124(3), 3024–3035.

Chen, C., Wang, G., Yan, Y., & Luo, F. (2021). Projected sea level rise on the continental

shelves of the China Seas and the dominance of mass contribution. Environmental Research Letters, 16(6).

Chen, J. L., Wilson, C. R., & Tapley, B. D. (2010). The 2009 exceptional Amazon flood and interannual terrestrial water storage change observed by GRACE. Water Resources Research, 46(12), 1–10.

Chen, N., Han, G., & Yang, J. (2018). Mean relative sea level rise along the coasts of the China Seas from mid-20th to 21st centuries. Continental Shelf Research, 152, 27-34.

Chen, X., & Tung, K. K. (2014). Varying planetary heat sink led to global-warming slowdown and acceleration. Science, 345(6199), 897–903.

Chen, X., Zhang, X., Church, J. A., Watson, C. S., King, M. A., Monselesan, D., … Harig, C. (2017). The increasing rate of global mean sea-level rise during 1993-2014. Nature Climate Change, 7(7), 492–495.

Cheng, L., Trenberth, K. E., Fasullo, J., Boyer, T., Abraham, J., & Zhu, J. (2017). Improved estimates of ocean heat content from 1960 to 2015. Science Advances, 3(3), 1–11.

Cheng, L., Zheng, F., & Zhu, J. (2015). Distinctive ocean interior changes during the recent warming slowdown. Scientific Reports, 5, 1–11.

Cheng, X., & Qi, Y. (2010). On steric and mass-induced contributions to the annual sea-level variations in the South China Sea. Global and Planetary Change, 72(3), 227–233.

Cheng, X., Xie, S. P., Du, Y., Wang, J., Chen, X., & Wang, J. (2016). Interannual-to-decadal variability and trends of sea level in the South China Sea. Climate Dynamics, 46(9–10), 3113–3126.

Chiang, J. C. H., & Vimont, D. J. (2004). Analogous Pacific and Atlantic Meridional Modes

of Tropical Atmosphere – Ocean Variability. Journal of Climate, 17, 4143–4158.

Choi, B. J., Haidvogel, D. B., & Cho, Y. K. (2004). Nonseasonal sea level variations in the Japan/East Sea from satellite altimeter data. Journal of Geophysical Research: Oceans, 109(12), 1–12.

Cogley, J. G. (2009). Geodetic and direct mass-balance measurements: Comparison and joint analysis. Annals of Glaciology, 50(50), 96–100.

Dee, D. P., Uppala, S. M., Simmons, A. J., Berrisford, P., Poli, P., Kobayashi, S., ... Bechtold, P. (2011). The ERA-Interim reanalysis: Configuration and performance of the data assimilation system. Quarterly Journal of the royal meteorological society, 137(656), 553-597.

Dangendorf, S., Frederikse, T., Chafik, L., Klinck, J. M., Ezer, T., & Hamlington, B. D. (2021). Data-driven reconstruction reveals large-scale ocean circulation control on coastal sea level. Nature Climate Change, 11(6), 514–520.

Dieng, H. B., Cazenave, A., Meyssignac, B., & Ablain, M. (2017). New estimate of the current rate of sea level rise from a sea level budget approach. Geophysical Research Letters, 44(8), 3744–3751.

Dieng, H. B., Palanisamy, H., Cazenave, A., Meyssignac, B., & von Schuckmann, K. (2015). The Sea Level Budget Since 2003: Inference on the Deep Ocean Heat Content. Surveys in Geophysics, 36(2), 209–229.

Dong, S., & Kelly, K. A. (2004). Heat budget in the Gulf Stream region: The importance of heat storage and advection. Journal of physical oceanography, 34(5), 1214-1231.

Durack, P. J., Gleckler, P. J., Landerer, F. W., & Taylor, K. E. (2014). Quantifying

underestimates of long-term upper-ocean warming. Nature Climate Change, 4(11), 999–1005.

Eagleson, P. S. (1978). Climate, soil, and vegetation: 1. Introduction to water balance dynamics. Water Resources Research, 14(5), 705-712.

ECCO Consortium , Fukumori, I., Wang, O., Fenty, I., Forget, G., Heimbach, P., & Ponte, R. M. (2021). Synopsis of the ECCO Central Production Global Ocean and Sea-Ice State Estimate (Version 4 Release 4)

England, M. H., Mcgregor, S., Spence, P., Meehl, G. A., Timmermann, A., Cai, W., … Santoso, A. (2014). Recent intensification of wind-driven circulation in the Pacific and the ongoing warming hiatus. Nature Climate Change, 4(3), 222–227.

Ezer, T. (2013). Sea level rise, spatially uneven and temporally unsteady: Why the U.S. East Coast, the global tide gauge record, and the global altimeter data show different trends. Geophysical Research Letters, 40(20), 5439–5444.

Fairall, C. W., Bradley, E. F., Rogers, D. P., Edson, J. B., & Young, G. S. (1996). Bulk parameterization of air-sea fluxes for tropical ocean-global atmosphere coupled-ocean atmosphere response experiment. Journal of Geophysical Research: Oceans, 101(C2), 3747-3764.

Fasullo, J. T., Boening, C., Landerer, F. W., & Nerem, R. S. (2013). Australia's unique influence on global sea level in 2010-2011. Geophysical Research Letters, 40(16), 4368–4373.

Feng, W., Zhong, M., & Xu, H. Z. (2012). Sea level variations in the South China Sea inferred from satellite gravity, altimetry, and oceanographic data. Science China Earth Sciences, 55(10), 1696–1701.

Forget, G., Campin, J. M., Heimbach, P., Hill, C. N., Ponte, R. M., & Wunsch, C. (2015). ECCO version 4: An integrated framework for non-linear inverse modeling and global ocean state estimation. Geoscientific Model Development, 8(10), 3071–3104.

Franzke, C. (2010). Long-range dependence and climate noise characteristics of Antarctic temperature data. Journal of Climate, 23(22), 6074-6081.

Franzke, C. (2012). Nonlinear trends, long-range dependence, and climate noise properties of surface temperature. Journal of Climate, 25(12), 4172-4183.

Frederikse, T., Landerer, F., & Caron, L. (2019). The imprints of contemporary mass redistribution on local sea level and vertical land motion observations. Solid Earth, 10(6), 1971–1987.

Frederikse, T., Landerer, F., Caron, L., Adhikari, S., Parkes, D., Humphrey, V. W., … Wu, Y. H. (2020). The causes of sea-level rise since 1900. Nature, 584(7821), 393–397.

Fu, L. L. (2016). On the decadal trend of global mean sea level and its implication on ocean heat content change. Frontiers in Marine Science, 3(MAR), 1–6.

Fukumori, I., Wang, O., Fenty, I., Forget, G., Heimbach, P., & Ponte, R. M. (2017). ECCO version 4 release 3.

Fukumori, I., Wang, O., Llovel, W., Fenty, I., & Forget, G. (2015). A near-uniform fluctuation of ocean bottom pressure and sea level across the deep ocean basins of the Arctic Ocean and the Nordic Seas. Progress in Oceanography, 134, 152–172.

Gardner, A. S., Moholdt, G., Cogley, J. G., Wouters, B., Arendt, A. A., Wahr, J., … Paul, F. (2013). A reconciled estimate of glacier contributions to sea level rise: 2003 to 2009. Science, 340(6134), 852–857.

GISTEMP Team, 2018: GISS Surface Temperature Analysis (GISTEMP). NASA Goddard Institute for Space Studies. [Available at https://data.giss.nasa.gov/gistemp/. Dataset accessed 2018-06-23.]

Good, S. A., Martin, M. J., & Rayner, N. A. (2013). EN4: Quality controlled ocean temperature and salinity profiles and monthly objective analyses with uncertainty estimates. Journal of Geophysical Research: Oceans, 118(12), 6704–6716.

Gray, L. J., Scaife, A. A., Mitchell, D. M., Osprey, S., Ineson, S., Hardiman, S., … Kodera, K. (2013). A lagged response to the 11 year solar cycle in observed winter Atlantic/European weather patterns. Journal of Geophysical Research Atmospheres, 118(24), 13,405-13,420.

Gregory, J. M., Griffies, S. M., Hughes, C. W., Lowe, J. A., Church, J. A., Fukimori, I., … van de Wal, R. S. W. (2019). Concepts and Terminology for Sea Level: Mean, Variability and Change, Both Local and Global. In Surveys in Geophysics (Vol. 40).

Groh, A., Horwath, M., Horvath, A., Meister, R., Sørensen, L. S., Barletta, V. R., … Shepherd, A. (2019). Evaluating GRACE mass change time series for the antarctic and Greenland ice sheet-methods and results. Geosciences (Switzerland), 9(10).

Guo, J., Hu, Z., Wang, J., Chang, X., & Li, G. (2015). Sea level changes of China seas and neighboring ocean based on satellite altimetry missions from 1993 to 2012. Journal of Coastal Research, (August 2002), 17–21.

Haidvogel, D. B., Arango, H. G., Hedstrom, K., Beckmann, A., Malanotte-Rizzoli, P., & Shchepetkin, A. F. (2000). Model evaluation experiments in the North Atlantic Basin: simulations in nonlinear terrain-following coordinates. Dynamics of atmospheres and oceans, 32(3-4), 239-281.

Haidvogel, D. B., Arango, H., Budgell, W. P., Cornuelle, B. D., Curchitser, E., Di Lorenzo,

E., ... Levin, J. (2008). Ocean forecasting in terrain-following coordinates: Formulation and skill assessment of the Regional Ocean Modeling System. Journal of Computational Physics, 227(7), 3595-3624.

Hamlington, B. D., Cheon, S. H., Thompson, P. R., Merrifield, M. A., Nerem, R. S., Leben, R. R., & Kim, K. Y. (2016). An ongoing shift in Pacific Ocean sea level. Journal of Geophysical Research: Oceans, 121(7), 5084-5097.

Hamlington, B. D., Cheon, S. H., Piecuch, C. G., Karnauskas, K. B., Thompson, P. R., Kim, K. Y., … Frederikse, T. (2019). The Dominant Global Modes of Recent Internal Sea Level Variability. In Journal of Geophysical Research: Oceans (Vol. 124).

Hamlington, B. D., Reager, J. T., Lo, M. H., Karnauskas, K. B., & Leben, R. R. (2017). Separating decadal global water cycle variability from sea level rise. Scientific Reports, 7(1), 1–7.

Hamlington, B. D., Gardner, A. S., Ivins, E., Lenaerts, J. T., Reager, J. T., Trossman, D. S., ... & Willis, M. J. (2020). Understanding of contemporary regional sea-level change and the implications for the future. Reviews of Geophysics, 58(3), e2019RG000672.

Hamlington, B. D., Piecuch, C. G., Reager, J. T., Chandanpurkar, H., Frederikse, T., Nerem, R. S., … Cheon, S.-H. (2020). Origin of interannual variability in global mean sea level. Proceedings of the National Academy of Sciences, 201922190.

Hansen, J., Ruedy, R., Sato, M., & Lo, K. (2010). Global surface temperature change. Reviews of Geophysics, 48(4).

Harvey, T. C., Hamlington, B. D., Frederikse, T., Nerem, R. S., Piecuch, C. G., Hammond, W. C., … Boening, C. (2021). Ocean mass, sterodynamic effects, and vertical land motion largely explain US coast relative sea level rise. Communications Earth & Environment,

2(1).

Hathaway, D. H. (2015). The solar cycle. Living Reviews in Solar Physics, 12(1).

Haigh, J. D. (1996). The impact of solar variability on climate. Science, 272(5264), 981-984.

Haigh, J. D., Blackburn, M., & Day, R. (2005). The response of tropospheric circulation to perturbations in lower-stratospheric temperature. Journal of Climate, 18(17), 3672-3685.

Hood, L., Schimanke, S., Spangehl, T., Bal, S., & Cubasch, U. (2013). The surface climate response to 11-yr solar forcing during northern winter: Observational analyses and comparisons with GCM simulations. Journal of climate, 26(19), 7489-7506.

Hosoda, S., Ohira, T., & Nakamura, T. (2008). A monthly mean dataset of global oceanic temperature and salinity derived from Argo float observations. JAMSTEC Report of Research and Development, 8, 47-59.

Hu, S., & Fedorov, A. V. (2016). Exceptionally strong easterly wind burst stalling El Niño of 2014. Proceedings of the National Academy of Sciences, 113(8), 2005-2010.

Hu, S., & Fedorov, A. V. (2017a). The extreme El Niño of 2015–2016: The role of westerly and easterly wind bursts, and preconditioning by the failed 2014 event. Climate Dynamics, 1-19.

Hu, S., & Fedorov, A. V. (2017b). The extreme El Niño of 2015–2016 and the end of global warming hiatus. Geophysical Research Letters, 44(8), 3816-3824.

Hu, X., Sejas, S. A., Cai, M., Taylor, P. C., Deng, Y., & Yang, S. (2019). Decadal evolution of the surface energy budget during the fast warming and global warming hiatus periods in the ERA-interim. Climate Dynamics, 52(3–4), 2005–2016.

Huang, B., Banzon, V. F., Freeman, E., Lawrimore, J., Liu, W., Peterson, T. C., ... Zhang, H.

M. (2015). Extended reconstructed sea surface temperature version 4 (ERSST. v4). Part I: upgrades and intercomparisons. Journal of climate, 28(3), 911-930.

Huang, B., Thorne, P. W., Smith, T. M., Liu, W., Lawrimore, J., Banzon, V. F., ... Menne, M. (2016). Further exploring and quantifying uncertainties for extended reconstructed sea surface temperature (ERSST) version 4 (v4). Journal of Climate, 29(9), 3119-3142.

Huang, N. E., Shen, Z., Long, S. R., Wu, M. C., Shih, H. H., Zheng, Q., … Liu, H. H. (1998). The empirical mode decomposition and the Hilbert spectrum for nonlinear and non-stationary time series analysis. Proceedings of the Royal Society A: Mathematical, Physical and Engineering Sciences, 454(1971), 903–995.

Huang, N. E., & Wu, Z. (2008). A review on Hilbert-Huang transform: Method and its applications to geophysical studies. Reviews of geophysics, 46(2).

Humphrey, V., Gudmundsson, L., & Seneviratne, S. I. (2016). Assessing global water storage variability from GRACE: Trends, seasonal cycle, subseasonal anomalies and extremes. Surveys in geophysics, 37, 357-395.

IMBIE Team. (2020). Mass balance of the Greenland Ice Sheet from 1992 to 2018. Nature, 579(7798), 233–239.

IPCC. (2013). Climate change 2013: The physical science basis. Contribution of working group I to the fifth assessment report of the intergovernmental panel on climate change. Cambridge University Press.

Ishii, M., Fukuda, Y., Hirahara, S., Yasui, S., Suzuki, T., & Sato, K. (2017). Accuracy of Global Upper Ocean Heat Content Estimation Expected from Present Observational Data Sets. Sola, 13(0), 163–167.

Ishii, M., & Kimoto, M. (2009). Reevaluation of historical ocean heat content variations with time-varying XBT and MBT depth bias corrections. Journal of Oceanography, 65(3), 287–299.

Ji, F., Wu, Z., Huang, J., & Chassignet, E. P. (2014). Evolution of land surface air temperature trend. Nature Climate Change, 4(6), 462–466.

Jin, Y., Zhang, X., Church, J. A., & Bao, X. (2021). Projected sea level changes in the marginal seas near China based on dynamical downscaling. Journal of Climate, 34(17), 7037–7055.

Jo, S., Moon, J.-H., Kim, T., Song, Y. T., & Cha, H. (2022). Interannual Modulation of Kuroshio in the East China Sea Over the Past Three Decades. Frontiers in Marine Science, 9(June), 1–11.

Johnson, G. C., & Birnbaum, A. N. (2017). As El Niño builds, Pacific Warm Pool expands, ocean gains more heat. Geophysical Research Letters, 44(1), 438–445.

Johnson, G. C., Lyman, J. M., & Loeb, N. G. (2016). Improving estimates of Earth's energy imbalance. Nature Climate Change, 6(7), 639–640.

Johnson, G. C., Lyman, J. M., & Purkey, S. G. (2015). Informing deep argo array design using argo and full-depth hydrographic section data. Journal of Atmospheric and Oceanic Technology, 32(11), 2187–2198.

Kalnay, E., Kanamitsu, M., Kistler, R., Collins, W., Deaven, D., Gandin, L., ... Zhu, Y. (1996). The NCEP/NCAR 40-year reanalysis project. Bulletin of the American meteorological Society, 77(3), 437-472.

Kidwell, A., Jo, Y. H., & Yan, X. H. (2014). A closer look at the central Pacific El Niño and warm pool migration events from 1982 to 2011. Journal of Geophysical Research: Oceans,

119(1), 165-172.

Kim, S.-B., & Fukumori, I. (2008). A near uniform basin-wide sea level fluctuation over the Japan East : A semienclosed sea with multiple straits. Journal of Geophysical Research, 113.

Kodera, K., & Kuroda, Y. (2002). Dynamical response to the solar cycle. Journal of Geophysical Research Atmospheres, 107(24), ACL 5-1-ACL 5-12.

Kosaka, Y., & Xie, S. P. (2013). Recent global-warming hiatus tied to equatorial Pacific surface cooling. Nature, 501(7467), 403-407.

Köhl, A. (2020). Evaluating the GECCO3 1948–2018 ocean synthesis – a configuration for initializing the MPI-ESM climate model. Quarterly Journal of the Royal Meteorological Society, 146(730), 2250–2273.

Landerer, F. W., Jungclaus, J. H., & Marotzke, J. (2007). Ocean bottom pressure changes lead to a decreasing length-of-day in a warming climate. Geophysical Research Letters, 34(6), 1–5.

Large, W. G., McWilliams, J. C., & Doney, S. C. (1994). Oceanic vertical mixing: A review and a model with a nonlocal boundary layer parameterization. Reviews of Geophysics, 32(4), 363-403.

Leclercq, P. W., Oerlemans, J., & Cogley, J. G. (2011). Estimating the Glacier Contribution to Sea-Level Rise for the Period 1800-2005. Surveys in Geophysics, 32(4–5), 519–535.

Lee, H. S., Yamashita, T., & Mishima, T. (2012). Multi-decadal variations of ENSO, the Pacific Decadal Oscillation and tropical cyclones in the western North Pacific. Progress in oceanography, 105, 67-80.

Lee, S. K., Park, W., Baringer, M. O., Gordon, A. L., Huber, B., & Liu, Y. (2015). Pacific origin of the abrupt increase in Indian Ocean heat content during the warming hiatus. Nature Geoscience, 8(6), 445-449.

Lee, T., & McPhaden, M. J. (2010). Increasing intensity of El Niño in the central-equatorial Pacific. Geophysical Research Letters, 37(14), 1–5.

Lenssen, N. J. L., Schmidt, G. A., Hansen, J. E., Menne, M. J., Persin, A., Ruedy, R., & Zyss, D. (2019). Improvements in the GISTEMP Uncertainty Model. Journal of Geophysical Research: Atmospheres, 124(12), 6307–6326.

Leuliette, E. W., & Willis, J. K. (2011). Balancing the sea level budget. Oceanography, 24(2), 122–129.

Levine, A. F., & McPhaden, M. J. (2016). How the July 2014 easterly wind burst gave the 2015–2016 El Niño a head start. Geophysical research letters, 43(12), 6503-6510.

Levitus, S., Antonov, J. I., Boyer, T. P., Locarnini, R. A., Garcia, H. E., & Mishonov, A. V. (2009). Global ocean heat content 1955–2008 in light of recently revealed instrumentation problems. Geophysical Research Letters, 36(7).

Levitus, S., Antonov, J. I., Boyer, T. P., Baranova, O. K., Garcia, H. E., Locarnini, R. A., … Zweng, M. M. (2012). World ocean heat content and thermosteric sea level change (0-2000m), 1955-2010. Geophysical Research Letters, 39(10), 1–5.

Lin, Y. (2021). The Footprint of the 11-Year Solar Cycle in Northeastern Pacific SSTs and Its Influence on the Central Pacific El Niño Geophysical Research Letters. Geophysical Research Letters, 1–10.

Liu, W., Huang, B., Thorne, P. W., Banzon, V. F., Zhang, H. M., Freeman, E., ... Woodruff, S.

D. (2015). Extended reconstructed sea surface temperature version 4 (ERSST. v4): Part II. Parametric and structural uncertainty estimations. Journal of Climate, 28(3), 931-951.

Liu, Y. C., Hwang, C., Han, J., Kao, R., Wu, C. R., Shih, H. C., & Tangdamrongsub, N. (2016). Sediment-Mass accumulation rate and variability in the East China Sea detected by GRACE. Remote Sensing, 8(9), 1–19.

Llovel, W., Becker, M., Cazenave, A., Jevrejeva, S., Alkama, R., Decharme, B., … Beckley, B. (2011). Terrestrial waters and sea level variations on interannual time scale. Global and Planetary Change, 75(1–2), 76–82.

Llovel, W., Willis, J. K., Landerer, F. W., & Fukumori, I. (2014). Deep-ocean contribution to sea level and energy budget not detectable over the past decade. Nature Climate Change, 4(11), 1031-1035.

Llovel, William, & Terray, L. (2016). Observed southern upper-ocean warming over 2005-2014 and associated mechanisms. Environmental Research Letters, 11(12).

Loeb, N. G., Johnson, G. C., Thorsen, T. J., Lyman, J. M., Rose, F. G., & Kato, S. (2021). Satellite and Ocean Data Reveal Marked Increase in Earth's Heating Rate. Geophysical Research Letters, 48(13), 1–8.

Long, X., Widlansky, M. J., Schloesser, F., Thompson, P. R., Annamalai, H., Merrifield, M. A., & Yoon, H. (2020). Higher sea levels at Hawaii caused by strong El Niño and weak trade winds. Journal of Climate, 33(8), 3037-3059.

Loomis, B. D., Luthcke, S. B., & Sabaka, T. J. (2019). Regularization and error characterization of GRACE mascons. Journal of Geodesy, 93(9), 1381–1398.

Lyman, J. M., Good, S. A., Gouretski, V. V., Ishii, M., Johnson, G. C., Palmer, M. D., … Willis,

J. K. (2010). Robust warming of the global upper ocean. Nature, 465(7296), 334–337.

Maher, N., Gupta, A. S., & England, M. H. (2014). Drivers of decadal hiatus periods in the 20th and 21st centuries. Geophysical Research Letters, 41(16), 5978-5986.

Maher, N., England, M. H., Gupta, A. Sen, & Spence, P. (2018). Correction to: Role of Pacific trade winds in driving ocean temperatures during the recent slowdown and projections under a wind trend reversal. Climate Dynamics, 0(0), 1.

Mantua, N. J., Hare, S. R., Zhang, Y., Wallace, J. M., & Francis, R. C. (1997). A Pacific interdecadal climate oscillation with impacts on salmon production. Bulletin of the american Meteorological Society, 78(6), 1069-1080.

Marzeion, B., Cogley, J. G., Richter, K., & Parkes, D. (2014). Attribution of Past Glacier Mass Loss to Anthropogenic and Natural Climate Forcing. Science, 345(6199), 919–921.

Marzeion, B., Leclercq, P. W., Cogley, J. G., & Jarosch, A. H. (2015). Brief Communication: Global reconstructions of glacier mass change during the 20th century are consistent. Cryosphere, 9(6), 2399–2404.

Matthes, K., Kuroda, Y., Kodera, K., & Langematz, U. (2006). Transfer of the solar signal from the stratosphere to the troposphere: Northern winter. Journal of Geophysical Research: Atmospheres, 111(D6).

McPhaden, M. J. (2015). Playing hide and seek with El Niño. Nature Climate Change, 5(9), 791-795.

Meehl, G. A., Arblaster, J. M., Matthes, K., Sassi, F., & Van Loon, H. (2009). Amplifying the pacific climate system response to a small 11-year solar cycle forcing. Science, 325(5944), 1114–1118.

Meehl, G. A., & Arblaster, J. M. (2011). Decadal variability of Asian–Australian monsoon–ENSO–TBO relationships. Journal of Climate, 24(18), 4925-4940.

Meehl, G. A., Hu, A., Arblaster, J. M., Fasullo, J., & Trenberth, K. E. (2013). Externally forced and internally generated decadal climate variability associated with the Interdecadal Pacific Oscillation. Journal of Climate, 26(18), 7298-7310.

Meehl, G. A., Hu, A., & Teng, H. (2016). Initialized decadal prediction for transition to positive phase of the Interdecadal Pacific Oscillation. Nature communications, 7, 11718.

Merrifield, M. A., Thompson, P. R., & Lander, M. (2012). Multidecadal sea level anomalies and trends in the western tropical Pacific. Geophysical Research Letters, 39(13).

Meyssignac, B., Boyer, T., Zhao, Z., Hakuba, M. Z., Landerer, F. W., Stammer, D., … Zilberman, N. (2019). Measuring global ocean heat content to estimate the earth energy imbalance. Frontiers in Marine Science, 6(JUL), 1–31.

Misios, S., Mitchell, D. M., Gray, L. J., Tourpali, K., Matthes, K., Hood, L., … Krivolutsky, A. (2016). Solar signals in CMIP-5 simulations: Effects of atmosphere-ocean coupling. Quarterly Journal of the Royal Meteorological Society, 142(695), 928–941.

Moon, J. H., Song, Y. T., Bromirski, P. D., & Miller, A. J. (2013). Multidecadal regional sea level shifts in the Pacific over 1958–2008. Journal of Geophysical Research: Oceans, 118(12), 7024-7035.

Moon, J.-H., & Tony Song, Y. (2013). Sea level and heat content changes in the western North Pacific. Journal of Geophysical Research: Oceans, 118(4), 2014–2022. https://doi.org/10.1002/jgrc.20096

Moreira, L., Cazenave, A., & Palanisamy, H. (2021). Influence of interannual variability in

estimating the rate and acceleration of present-day global mean sea level. Global and Planetary Change, 199(February), 103450.

Moum, J. N., Perlin, A., Nash, J. D., & McPhaden, M. J. (2013). Seasonal sea surface cooling in the equatorial Pacific cold tongue controlled by ocean mixing. Nature, 500(7460), 64-67.

Mudelsee, M. (2019). Trend analysis of climate time series: A review of methods. Earth-Science Reviews, 190(December 2018), 310–322.

NASA News (2017), NASA, NOAA data show 2016 warmest year on record globally. [Available at https://www.nasa.gov/press-release/nasa-noaa-data-show-2016-warmest-year-on-record-globally. Accessed 2017–01-31.]

Nerem, R. S., Beckley, B. D., Fasullo, J. T., Hamlington, B. D., Masters, D., & Mitchum, G. T. (2018). Climate-change–driven accelerated sea-level rise detected in the altimeter era. Proceedings of the National Academy of Sciences, 115(9), 2022–2025.

Newman, M., Alexander, M. A., Ault, T. R., Cobb, K. M., Deser, C., Di Lorenzo, E., … Smith, C. A. (2016). The Pacific decadal oscillation, revisited. Journal of Climate, 29(12), 4399–4427.

Nieves, V., Willis, J. K., & Patzert, W. C. (2015). Recent hiatus caused by decadal shift in Indo-Pacific heating. Science, 349(6247), 532-535.

Oppenheimer, M. et al. (2019). Sea level rise and implications for low-Lying islands, coasts and communities. In IPCC Special Report on the Ocean and Cryosphere in a Changing Climate (eds Pörtner, H.-O. et al). (Cambridge University Press).

Paek, H., Yu, J. Y., & Qian, C. (2017). Why were the 2015/2016 and 1997/1998 extreme El

Niños different? Geophysical Research Letters, 44(4), 1848–1856.

Peltier, W. R. (2004). Global glacial isostasy and the surface of the ice-age earth: The ICE-5G (VM2) model and GRACE. Annual Review of Earth and Planetary Sciences, 32, 111–149.

Peltier, W. Richard, Argus, D. F., & Drummond, R. (2018). Comment on "An Assessment of the ICE-6G_C (VM5a) Glacial Isostatic Adjustment Model" by Purcell et al. Journal of Geophysical Research: Solid Earth, 123(2), 2019–2028.

Piecuch, C. G., & Ponte, R. M. (2011). Mechanisms of interannual steric sea level variability. Geophysical Research Letters, 38(15), 1–6.

Piecuch, C. G., & Quinn, K. J. (2016). El Niño, La Niña, and the global sea level budget. Ocean Science, 12(6), 1165–1177.

Ponte, R., Rajamony, J., & Gregory, J. (2002). Ocean angular momentum signals in a climate model and implications for Earth rotation. Climate Dynamics, 19(2), 181–182.

Power, S., Casey, T., Folland, C., Colman, A., & Mehta, V. (1999). Inter-decadal modulation of the impact of ENSO on Australia. Climate Dynamics, 15(5), 319-324.

Purkey, S. G., & Johnson, G. C. (2010). Warming of global abyssal and deep Southern Ocean waters between the 1990s and 2000s: Contributions to global heat and sea level rise budgets. Journal of Climate, 23(23), 6336–6351.

Qu, T., Du, Y., & Sasaki, H. (2006). South China Sea throughflow: A heat and freshwater conveyor. Geophysical Research Letters, 33(23), 8–11.

Reager, J. T., Famiglietti, J. S., Lo, M.-H., Eicker, A., Wiese, D. N., & Gardner, A. S. (2016). A decade of sea level rise slowed by climate-driven hydrology. Science, 351(6274), 699–

703.

Reichle, R. H., Koster, R. D., De Lannoy, G. J. M., Forman, B. A., Liu, Q., Mahanama, S. P. P., & Toure, A. (2011). Assessment and enhancement of MERRA land surface hydrology estimates. Journal of Climate, 24(24), 6322–6338.

Reichle, R. H., Draper, C. S., Liu, Q., Girotto, M., Mahanama, S. P. P., Koster, R. D., & De Lannoy, G. J. M. (2017). Assessment of MERRA-2 land surface hydrology estimates. Journal of Climate, 30(8), 2937–2960.

Rietbroek, R., Brunnabend, S. E., Kusche, J., Schröter, J., & Dahle, C. (2016). Revisiting the contemporary sea-level budget on global and regional scales. Proceedings of the National Academy of Sciences of the United States of America, 113(6), 1504–1509.

Riser, S. C., Freeland, H. J., Roemmich, D., Wijffels, S., Troisi, A., Belbéoch, M., ... & Jayne, S. R. (2016). Fifteen years of ocean observations with the global Argo array. Nature Climate Change, 6(2), 145-153.

Roemmich, D., Church, J., Gilson, J., Monselesan, D., Sutton, P., & Wijffels, S. (2015). Unabated planetary warming and its ocean structure since 2006. Nature Climate Change, 5(3), 240–245.

Royston, S., Vishwakarma, B. D., Westaway, R., Rougier, J., Sha, Z., & Bamber, J. (2020). Can We Resolve the Basin-Scale Sea Level Trend Budget From GRACE Ocean Mass? Journal of Geophysical Research: Oceans, 125(1).

Save, H., Bettadpur, S., & Tapley, B. D. (2016). High-resolution CSR GRACE RL05 mascons. Journal of Geophysical Research: Solid Earth.

Scanlon, B. R., Zhang, Z., Save, H., Sun, A. Y., Schmied, H. M., Van Beek, L. P. H., …

Bierkens, M. F. P. (2018). Global models underestimate large decadal declining and rising water storage trends relative to GRACE satellite data. Proceedings of the National Academy of Sciences of the United States of America, 115(6), E1080–E1089.

Scaife, A. A., Ineson, S., Knight, J. R., Gray, L., Kodera, K., & Smith, D. M. (2013). A mechanism for lagged North Atlantic climate response to solar variability. Geophysical Research Letters, 40(2), 434-439.

Shchepetkin, A. F., & McWilliams, J. C. (2005). The regional oceanic modeling system (ROMS): a split-explicit, free-surface, topography-following-coordinate oceanic model. Ocean modelling, 9(4), 347-404.

Shepherd, A., Ivins, E. R., A, G., Barletta, V. R., Bentley, M. J., Bettadpur, S., … Zwally, H. J. (2012). A Reconciled Estimate of Ice-Sheet Mass Balance. Science, 338(November), 1183–1190.

Song, Y., & Haidvogel, D. (1994). A semi-implicit ocean circulation model using a generalized topography-following coordinate system. Journal of Computational Physics, 115(1), 228-244.

Tamisiea, M., & Mitrovica, J. (2011). The Moving Boundaries of Sea Level Change: Understanding the Origins of Geographic Variability. Oceanography, 24(2), 24–39.

Tapley, B. D., Watkins, M. M., Flechtner, F., Reigber, C., Bettadpur, S., Rodell, M., … Velicogna, I. (2019). Contributions of GRACE to understanding climate change. Nature Climate Change, 9(5), 358–369.

Timmermann, A., McGregor, S., & Jin, F. F. (2010). Wind effects on past and future regional sea level trends in the southern Indo-Pacific. Journal of Climate, 23(16), 4429-4437.

Trenberth, K. E., & Fasullo, J. T. (2010). Tracking Earth's energy. Science, 328(5976), 316-317.

Trenberth, K. E., Fasullo, J. T., & Balmaseda, M. A. (2014). Earth's energy imbalance. Journal of Climate, 27(9), 3129–3144.

van Loon, H., Meehl, G. A., & Arblaster, J. M. (2004). A decadal solar effect in the tropics in July–August. Journal of Atmospheric and Solar-Terrestrial Physics, 66(18), 1767-1778.

Vivier, F., Kelly, K. A., & Thompson, L. A. (2002). Heat budget in the Kuroshio Extension region: 1993–99. Journal of physical oceanography, 32(12), 3436-3454.

von Schuckmann, K., & Le Traon, P.-Y. (2011). How well can we derive Global Ocean Indicators from Argo data? Ocean Science Discussions, 8(3), 999–1024. https://doi.org/10.5194/osd-8-999-2011

von Schuckmann, K., Cheng, L., Palmer, M. D., Hansen, J., Tassone, C., Aich, V., … Wijffels, S. E. (2020). Heat stored in the Earth system: Where does the energy go? Earth System Science Data, 12(3), 2013–2041.

Wada, Y., Van Beek, L. P. H., Sperna Weiland, F. C., Chao, B. F., Wu, Y. H., & Bierkens, M. F. P. (2012). Past and future contribution of global groundwater depletion to sea-level rise. Geophysical Research Letters, 39(9), 1–6.

Wang, J., Church, J. A., Zhang, X., Gregory, J. M., Zanna, L., & Chen, X. (2021). Evaluation of the Local Sea-Level Budget at Tide Gauges Since 1958. Geophysical Research Letters, 48(20), 1–12.

Watson, C. S., White, N. J., Church, J. A., King, M. A., Burgette, R. J., & Legresy, B. (2015). Unabated global mean sea-level rise over the satellite altimeter era. Nature Climate

Change, 5(6), 565–568.

WCRP Global Sea Level Budget Group. (2018). Global sea-level budget 1993 – present. Earth System Science, 10, 1551–1590.

Wentz, F. J., Scott, J., Hoffman, R., Leidner, M., Atlas, R., & Ardizzone, J. (2015). Remote Sensing Systems Cross-Calibrated Multi-Platform (CCMP) 6-hourly ocean vector wind analysis product on 0.25 deg grid, Version 2.0. Remote Sensing Systems, Santa Rosa, CA. Available online at www.remss.com/measurements/ccmp. [Accessed 23 06 2018].

White, W. B., Lean, J., Cayan, D. R., & Dettinger, M. D. (1997). Response of global upper ocean temperature to changing solar irradiance. Journal of Geophysical Research: Oceans, 102(C2), 3255-3266.

Wiese, D. N., Landerer, F. W., & Watkins, M. M. (2016). Quantifying and reducing leakage errors in the JPL RL05M GRACE mascon solution. Water Resources Research, 5(3), 2–2.

Wouters, B., Gardner, A. S., & Moholdt, G. (2019). Global glacier mass loss during the GRACE satellite mission (2002-2016). Frontiers in Earth Science, 7(May), 1–11.

Wu, C. R., Wang, Y. L., & Chao, S. Y. (2019). Disassociation of the Kuroshio Current with the Pacific Decadal Oscillation since 1999. Remote Sensing, 11(3).

Wu, Z., & Huang, N. E. (2004). A study of the characteristics of white noise using the empirical mode decomposition method. In Proceedings of the Royal Society of London A: Mathematical, Physical and Engineering Sciences, 460 (2046), 1597-1611.

Wu, Z., & Huang, N. E. (2009). Ensemble empirical mode decomposition: a noise-assisted data analysis method. Advances in adaptive data analysis, 1(01), 1-41.

Xie, S. P., Kosaka, Y., & Okumura, Y. M. (2016). Distinct energy budgets for anthropogenic and natural changes during global warming hiatus. Nature Geoscience, 9(1), 29–33.

Xue, Y., & Kumar, A. (2017). Evolution of the 2015/16 El Niño and historical perspective since 1979. Science China Earth Sciences, 60(9), 1572-1588.

Yang, Y., Feng, W., Zhong, M., Mu, D., & Yao, Y. (2022). Basin-Scale Sea Level Budget from Satellite Altimetry, Satellite Gravimetry, and Argo Data over 2005 to 2019. Remote Sensing, 14(18), 1–12.

Yi, S., Sun, W., Heki, K., & Qian, A. (2015). An increase in the rate of global mean sea level rise since 2010. Geophysical Research Letters, 42(10), 3998–4006.

Yu, J. Y., & Kim, S. T. (2011). Relationships between extratropical sea level pressure variations and the central Pacific and eastern Pacific types of ENSO. Journal of Climate, 24(3), 708–720.

Yu, K., Liu, H., Chen, Y., Dong, C., Dong, J., Yan, Y., & Wang, D. (2019). Impacts of the mid-latitude westerlies anomaly on the decadal sea level variability east of China. Climate Dynamics, 53(9–10), 5985–5998.

Zemp, M., Huss, M., Thibert, E., Eckert, N., McNabb, R., Huber, J., … Cogley, J. G. (2019). Global glacier mass changes and their contributions to sea-level rise from 1961 to 2016. Nature, 568(7752), 382–386.

Zhang, X., & Church, J. A. (2012). Sea level trends, interannual and decadal variability in the Pacific Ocean. Geophysical Research Letters, 39(21), 1–8.

Zhang, Y., He, B. I. N., Guo, L., & Liu, D. (2019). Differences in response of terrestrial water storage components to precipitation over 168 global river basins. Journal of

Hydrometeorology, 20(9), 1981–1999.